PAUL SCHERRER INSTITUT

PSI

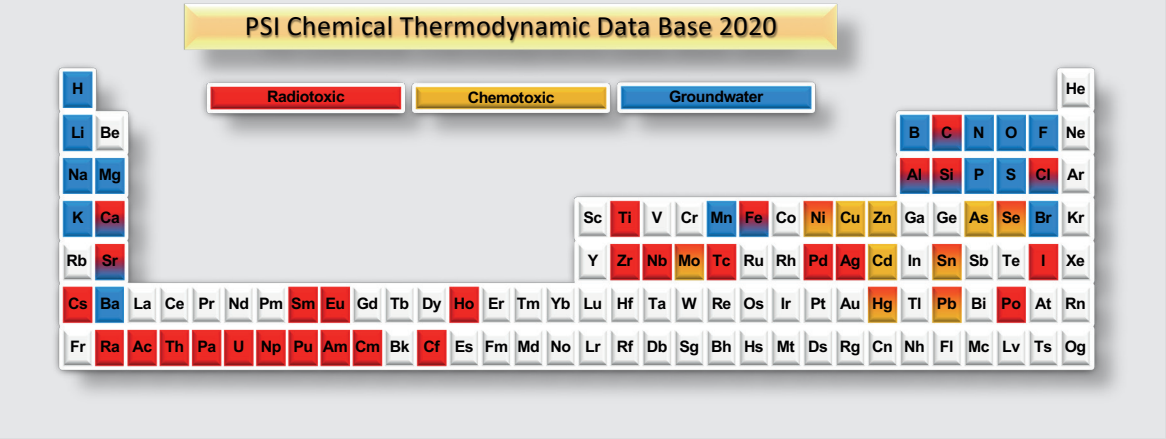

Progress Report 2020

Laboratory for Waste Management :: Nuclear Energy and Safety Department

Social eventic and research meetings in times of pandemic.

Cover
Updated thermodynamic database PSI-TDB 2020 (see chapter 6).

PAUL SCHERRER INSTITUT

PSI

Progress Report 2020

Laboratory for Waste Management
Nuclear Energy and Safety Department

See also our web-page
http://www.psi.ch/les/

Preface

The mission of the Laboratory for Waste Management (LES) is to carry out a comprehensive research and development (R&D) programme in support of Swiss radioactive waste disposal options. In particular, the aim is to be one of the world-leading laboratories in the fields of geochemistry of disposal systems and transport mechanisms of radionuclides, including geochemical retardation and immobilisation.

The laboratory serves an important national role by supporting the Swiss Federal Government and Nagra in their tasks to safely dispose of radioactive wastes from medical, industrial and research applications as well as from nuclear power plants. The research activities cover fundamental aspects of repository geochemistry, chemistry and physics of radionuclides at geological interfaces, and radionuclide transport and retardation in geological and technical barriers. The work performed is a balanced combination of experimental activities conducted in dedicated laboratories for handling radioactive isotopes, field experiments and computer simulations. The work is directed towards repository implementation and Nagra uses the results in their comprehensive performance assessments studies. The finalisation of the site selection process and the implementation of a repository in the next decades will require strong expertise in model-based assessments of the repository *in situ* conditions for specific repository designs. The long-term strategy of LES is thus to develop experimental and modelling expertise necessary for fully coupled description of relevant processes in a repository in order to assist safety driven implementation of disposal options in Switzerland.

Together with two other laboratories in the department of Nuclear Energy and Safety, LES maintains best practices and standards in the laboratory management and data processing according to the ISO9001:2015 certified Integrated Quality Management System. In 2020, LES has successfully passed the monitoring audit conducted by the Swiss Safety Center (www.safetycenter.ch). The certification covers the research and scientific services for agencies in the area of nuclear waste disposal and environmental sciences.

The present report summarises the research activities and results achieved in 2020. It gives a detailed overview of research projects, personnel management, national and international collaborations, and individual contributions achieved by scientists in the four research groups at PSI and the Chair of Mineralogy at the University of Bern.

We gratefully acknowledge the support of our work by PSI, Nagra, and numerous research programmes within national and European funding agencies (e.g. SNSF, ERC).

Table of Contents

1 OVERVIEW

Churakov S.V.

1.1 Introduction

The overall progress of the Laboratory for Waste Management (LES) from January 1st, 2020 to December 31th, 2020 is summarised in the first part of the report. The report is organised thematically according to the eight overarching research topics. These topics are multidisciplinary in nature and include contributions from different research groups at LES and the Mineralogy Group at the Institute of Geological Sciences at the University of Bern.

1.2 General

The site selection process for geological disposal of radioactive waste in Switzerland has entered its final stage. On November 22nd, 2018, the Swiss Federal Government has approved the further investigation of the "Jura Ost", "Nördlich Lägern" and "Zürich Nordost" areas for the final selection of a disposal site for a radioactive waste repository in Switzerland. All proposed siting regions are located within the Opalinus Clay formation. In 2019, Nagra has started the deep drilling campaign with the aim to characterise the local site-specific geological and hydrological conditions. First diffusion and sorption measurements on drill cores samples obtained at potential siting regions have started at LES in January 2020. The diffusion and sorption measurements on the drill cores were the most prominent activities 2020. Dedicated laboratory infrastructure and sampling methodology was prepared and tested back in 2019. Complete data sets for the Bülach1-1 and Trüllikon1-1 drillings were available by the end of 2020. The measurements will continue on samples from Bözberg1-1 and other locations in 2021. These geodata will provide a solid scientific basis for the performance assessment calculations and contribute to the chain of arguments in the site selection process.

It the current stage of the site selection process and the preparation of a general licence application, the priorities of the waste disposal implementation are focused on the synthesis of the technical documentation and the development of defendable chains of arguments for the discrimination between currently investigated disposal sites. In this context, LES' national role is to maintain the expertise in the field of waste disposal geochemistry, independent of the short-term priorities of the sectoral plan. Accordingly, LES continues research on the main pillars of repository safety, namely further development of models, providing mechanistic description of the sorption and transport behaviour of radionuclides, and reactive transport processes in the repository near-field. Present and future research activities focus on the behaviour of modern spent fuel under repository conditions, the chemical evolution of the repository near-field, sorption competition phenomena, the behaviour of redox-sensitive radionuclides, the role of mineral surface-induced redox reactions, and the transfer of sorption models and data from dispersed to compacted systems. LES further strengthens and builds up its experimental and modelling expertise in reactive transport simulations. These capabilities are particularly important for understanding the long-term evolution of *in situ* repository conditions and the interaction between repository barriers causing an alteration of their retention and transport properties. Special attention is paid to understanding the role of heterogeneities in the waste forms, which can lead locally to very specific chemical conditions.

Rapid advances in performance of parallel computers and improvements in accuracy of the so-called data driven surrogate models based on artificial intelligence and deep neural networks (AI/dNN) opens up opportunities for the development of robust coupled reactive transport codes and their practical application in performance assessment studies. LES is taking a leading role in the development of AI/dNN digital twins for laboratory experiments and field-scale mock ups. These beyond state-of-the-art models aim to assist the implementation of experimental studies in the lab and to facilitate the optimisation of the waste disposal design based on fully coupled THMC modelling.

Nearly 40 years of research on repository geochemistry resulted in large amounts of experimental, geo-chemical, and thermodynamic data. These data are particularly important for thermodynamic modelling, radionuclides retention and reactive transport simulations. Since many years, LES is supporting a long-term development of datasets for safety analysis, including sorption, diffusion and thermodynamics. A next update of the LES thermodynamic database in an electronic form was released in 2020 (www.psi.ch/en/les/database). The updated data set is fully integrated in the GEMS thermodynamic modelling software (gems.web.psi.ch).

In 2019, the Joint European Research Proposal COFUND-EJP NFRP-2018-6: *"European Joint Research Programme in the management and disposal of radioactive waste Eurad"* has been approved by the

European Commission. This project is a joint venture of 52 mandated research institutions, waste management organisations and technical safety organisations focusing on the most urgent research issues of nuclear waste disposal in Europe. Within the Eurad framework, LES participates in six individual work packages (WP):

FUTURE: Fundamental understanding of radionuclide retention (WP Lead and Task lead)

DONUT: Modelling of process couplings and numerical tools applied to performance assessment (Task co-Lead)

ACED: Assessment of chemical evolution of ILW and HLW disposal cells (Task Lead)

GAS: Mechanistic understanding of gas transport in clay materials (Contributor)

CORI: Cement organics radionuclide interactions (Contributor)

UMAN: Uncertainty management multi-actor network (Contributor)

Beginning of 2020 a second call for follow up projects within the Eurad consortium has been launched. LES has actively participated in the development of the project proposals in this second wave call. The submitted project proposals are under review.

Within EURATOM NFRP-2019-2020-10 RIA call LES participates to the project "Pre-disposal management of radioactive waste, PREDIS". This 4 years EU project was approved in spring 2020 and started in September 1st, 2020. The consortium includes 47 partners from 18 Member States. The research focus of the project is aligned with priorities formulated within the Roadmap Theme 2 of the Eurad strategic research agenda (https://www.ejp-eurad.eu/) and with those identified by the project's industrial End Users Group. LES participates in the work package focused on performance of cementitious waste packages and takes a leading role in the development of a model based digital twin for the estimation of waste packages evolution in the extended intermediate storage.

In 2020 LES continued its participation in the collaborative project *"Thermodynamik und Speziation von Aktiniden bei höheren Temperaturen"* (ThermAc) funded by the German Ministry of Education and Finances (BMBF) contributing to further extension of the database for high temperature properties of actinides.

The compound-specific analysis of ^{14}C compounds released by the corrosion of irradiated steel is ongoing. The results collected in 2019 and 2020 provide a first clear trend, explaining the release mechanism of the C14- bearing compounds in the aqueous and gaseous phase.

The reactive transport codes developed at LES are versatile and applicable to broad cross-disciplinary issues. The recently established collaboration with GlaxoSmithKline Vaccines (GSK), a science-led pharmaceutical company focused on the research, development and manufacturing of innovative pharmaceutical products, was continued.

Scientific exchange is an essential component of research and development programmes. Particularly important is the cross dissemination of knowledge in neighbouring fields. LES actively maintains collaborations with national and international research institutes in the field of waste management and environmental research. The main multi- and bi-lateral co-operations with external institutions and universities are summarised in Table 1.1.

Participation in international research projects and independent acquisition of funding for PhD and postdoc projects is an essential driving force for developing state-of-the-art research capabilities, knowledge transfer and education of young generation scientists. BSc/MSc/PhD projects and postdoc fellowships approved or started in 2020 are listed below along with ongoing ones:

T. Arnold (BSc student): *"Experimentelle Untersuchungen von Auflösungs- und Wachstums-prozessen auf Mineraloberflächen"* (UniBe 2019-2020)

R. Haller (BSc/MSc student): *"Geochemical modelling of reactive transport processes with deep neural networks"* (UniBe 2018-2021)

N. Krätiger (BSc/MSc student): *"Comparative study of C-S-H and ASR-products in cement by GCMC modelling"* (UniBe 2019-2022)

R. Mercutio (BSc student): *"Strukturveränderungen des Stellerit und Levyn durch Bleiaufnahme"* (UniBe 2019-2020)

D. Roos (MSc student): *"Structural changes and thermal stability of Pb^{2+}-modified zeolites"* (UniBe 2019/2021)

L. Hax Damiani (PhD student): *"Modelling transport across reactive interfaces with the Nernst-Planck approach"*. Start date: January 2016 (Funding: EU).

A. Glauser (PhD student/UBern): *"Development of quality of bottom ash from municipal solid waste incineration in Switzerland."* Start date: July 2017 (Funding: Various industrial partners).

P. Krejci (PhD student): *"Multispecies cation transport in compacted clays"*. Start date: December 2016 (Funding: Swiss National Science Foundation, SNSF).

P. Luraschi (PhD student): *"Evolution of transport properties, mineralogy and porosity of cement-clay interfaces"*. Start date: April 2017 (Funding: Nagra, PSI).

M. Mahrous (PhD student): *"Resolving dissolution-precipitation processes in porous media: Pore-scale lattice Boltzmann modelling combined with synchrotron-based X-ray characterisation"*. Start date: March 2018 (Funding: SNSF).

J. Owusu (PhD student): *"Pore-scale simulations of gas molecules in saturated and partially saturated clays"*. Start date: Nov 2019 (Funding: HORIZON 2020, Eurad).

Y. Qian (PhD student): *"Adsorption of redox sensitive radionuclides on Fe-bearing clay minerals"*. Start date: Nov 2019 (Funding: HORIZON 2020, Eurad).

R. Schliemann (PhD student): *"Dissolution, growth and ion uptake at phyllosilicate surfaces: Coupling atomistic interactions at the mineral water interface with Kinetic Monte Carlo model"*. Start date: July 2016 (Funding: SNSF).

M. Wolffers (PhD student/UBern): *"Genesis and characterisation of fly ash in Swiss waste incineration plants"* Start date: March 2019 (Funding: Industry).

Dr. Y. Chen (postdoc): *"Diffusive transport of gaseous species at saturated and partially saturated conditions"*. Start date: September 2019 (Funding: EU Horizon 2020 Marie Skłodowska-Curie grant, PSI-FELLOW-II-3i).

Dr. P. Cruz Hernandez (postdoc): *"Sorption mechanisms of Zn and U on Opalinus Clay"*. Start date: August 2019 (EU Horizon 2020 Marie Skłodowska-Curie grant, PSI-FELLOW-II-3i).

Dr. T.L. Guillemot (postdoc) *"Development of C-14 AMS based analytical methods for the identification and quantification of dissolved and volatile organic compounds"* Start date: January 2019 (Funding Nagra).

Dr. F. Marafatto (postdoc): *"Cryo-microspectroscopy at the microXAS beamline for the investigation of redox- and radiation-sensitive samples"*. Start date: June 2017 (Funding: PSI, EAWAG).

Dr. D. Miron (postdoc): *"Effect of aluminum on C-S-H structure, stability and solubility"*. Start date: December 2017 (Funding: SNSF).

Dr. G. Geng (PSI-FELLOW-II-3i postdoc): *"Alkali-silica reaction in concrete"*. Start date: July 2017 (Funding: SNSF, EU Horizon 2020 Marie Skłodowska-Curie grant, PSI-FELLOW-II-3i).

Dr. R. Patel (postdoc): *"Resolving carbonation mechanisms of cement-based materials through multi-scale microstructural simulations"*. Start date: August 2017. Completed: July 2019 (Funding: EU Horizon 2020 Marie Skłodowska-Curie grant, PSI-FELLOW-II-3i);
"Boiling crisis in nuclear reactor". Start date: August 2019 (Funding: Swissnuclear).

Tab. 1.1: National and international co-operations.

Co-operations
National
Nagra* (Major financial contribution, Various technical working groups) Swissnuclear* (Reactor safety, material aging)
Multinational
NEA Thermodynamic Database Project EURATOM HORIZON2020 (Eurad) EURATOM HORIZON2020 (PREDIS) EURATOM HORIZON2020 (DISCO) Mont Terri Projects* (diffusion retardation, clay-cement interaction)
Universities
University of Bern*, Switzerland (mineralogy, petrography, water chemistry, C-14 AMS) EPFL, Switzerland (cement systems) Université de Bourgogne, Dijon, France (molecular modelling) ETH Zurich*, Switzerland (GEMS) Hiroshima University, Japan (clay-cement interaction) University of Luxembourg* (porous media) Sino-French Institute of Nuclear Engineering and Technology, Sun Yatsen University (diffusion) Uppsala University, Sweden (atomistic simulations)
Research Centres
CEA*, France (chemistry of near-and far-field) Eawag, Switzerland (Gas MS analytics) EMPA*, Switzerland (cement, ceramics) IFR, HZDR*, Germany (XAS, TRLFS, atomistic modelling, reactive transport) INE, KIT*, Germany (near- and far-field; TRLFS) FZJ, Germany (sorption/diffusion of Ra, reactive transport, thermodynamics of solid solutions) SCK/CEN, Belgium (clay and cement systems) UFZ*, Germany (reactive transport, clay systems)
Industrial Partners
GlaxoSmithKline NanoCem

**formal co-operation agreements*

Several LES PhD students have defended their PhD thesis in 2020:

A. Mancini: *"Thermodynamic and spectroscopic investigations of ferric and ferrous iron in cementitious systems"*. PhD Defence 18 March 2020, ETH Zurich (Funding: SNSF).

S. Wick: *"Thallium Sorption onto Illite and Birnessite and its Relevance in Soils"*. PhD Defence 28 January 2020, ETH Zurich (Funding: SNSF).

LES has an aging research team. The personnel planning and knowledge transfer is one of the main concerns of the LES management. A broad consensus has been established that experimental research expertise at LES has to cover the main pillars of repository safety such as diffusion, sorption and the modelling of reactive transport phenomena. To keep long-term leadership in the field of geochemical modelling a new tenure track position was announced in the beginning of 2020. After a careful evaluation of highly qualified applications, the position was offered to Dr. G. D. Miron, who has been strongly involved in the development of thermodynamic databases and successful data management.

Another tenure track position is opened in the field of reactive transport experiments in December 2020. The candidate selection is ongoing and the position is expected to be filled in spring-summer 2021. The successful candidate is expected to strengthen the synergies between the laboratory and field experiments and take a leading role in representing LES in the Mont Terri Research Consortium.

Dr. Bart Baeyens, former head of the “Clay Sorption Mechanism Group” and a highly respected expert in sorption model development, retired in December 2020. Dr. Bart Baeyens leaves behind 34 years of experience in the field of radionuclides retention. This knowledge and expertise was transferred to Dr. Maria Marques who has taken the lead of the group in July 2020. The expertise of Bart Baeyens is essential for the successful accomplishment of the experimental work on the sorption on samples from the drill cores. Accordingly, Dr. Bart Baeyens will continue to support LES as a consultant in 2021.

The organisational chart of LES comprises four research groups located at PSI (Fig. 1.1). A fifth research group is located at the Institute of Geological Sciences (IfG) at the University of Bern. The mineralogy group at IfG is complementing the expertise in the field of mineral dissolution kinetics, structural studies of high porous materials and X-ray diffraction-based structure refinement, and the geochemistry of conventional waste disposal. In particular, the mineralogy group hosts the Competence Centre for Secondary Raw Materials conducting applied research in the field of environmental geochemistry and secondary raw materials recycling.

The LES annual report 2020 is organised in seven thematic research projects addressing specific aspects of repository geochemistry and radionuclide transport:

Chapter 2: Geochemical evolution of repository systems

Chapter 3: Development of mechanistic sorption models and experimental validation

Chapter 4: Radionuclides transport and retention in compacted systems at full and partial saturation

Chapter 5: Radioactive waste characterisation

Chapter 6: Thermodynamic models and databases

Chapter 7: Fundamental aspects of mineral reactivity and structural transformations

Chapter 8: Geochemical aspects of conventional waste materials and their disposal

The following section provides an overview of activities related to the Sectoral Plan for Deep Geological Disposal, repository near- and far-field, reactivity of barrier systems and code benchmarking activities.

1.3 Sectoral plan for deep geological disposal

The potential radiological impact of a repository is one of the main safety relevant criteria employed in the site selection process. Sorption and diffusion data are the basis for dose calculations. The sorption databases for *in situ* repository conditions are derived using a thermodynamic approach. The updated PSI chemical thermodynamic database TDB-2020, is released in electronic form as a part of the GEMS geochemical solver together with a detailed documentation of the recommended thermodynamic parameters. The TDB revision has been finalised in 2020 with a review of selected organic ligands, alkali (Li, Na, K) and alkaline earth (Mg, Ca, Sr, Ba) phosphate compounds and complexes, Fe species and selected data from the latest NEA review of U, Np, Pu, Am and Tc data. This database will be the reference for all subsequent thermodynamic calculations within the “Sachplan Geologische Tiefenlager, Etappe 3” (see section 6.2).

The systematic evaluation of isocoulombic reactions for estimating the temperature dependence of lanthanide and actinide complexes has continued. To identify the optimal reactions that produce the best estimates, the isocoulombic method has been tested against available experimental data on the temperature dependence of aqueous complexation and solubility reactions of lanthanides and actinides. To facilitate the evaluation, a dedicated database and a complementary

tool for the automated generation of alternative isocoulombic reactions and identified criteria for choosing the optimal ones were implemented as a part of the ThermoHub software package (thermohub.org/thermomatch/isoc/). The development of the isocoulombic reaction approach was part of the ThermAc project (2015-2020), supported by the German Federal Ministry of Education and Research (see section 6.3).

An update of the cement sorption database for the use in safety assessments is planned for 2022. Missing gaps in the database are completed by experimental studies. In 2020, sorption kinetic studies with ^{45}Ca and ^{32}Si on C-S-H phases, portlandite and degraded hardened cement paste were completed. In addition, ^{45}Ca, ^{35}S and $^{14}CO_3^{2-}$ sorption studies on monocarbonate, hemicarbonate and ettringite were launched. Finalisation of these studies is planned in early 2021 (see section 6.4).

Calcium silicate hydrates (C-S-H) determine the most relevant properties and the durability of hydrated cement pastes and concretes. C-S-H have a complex structure and a wide variation of chemical compositions. In a collaborative SNSF project "CASH-2", a new, flexible and extendable CASH+ sublattice solid solution model, consistent with the C-S-H defect-tobermorite structure, and describing the stability, solubility, density, water content and mean silicate chain length (MCL) of C-S-H phases has been developed. The CASH+ model considers simultaneous substitutions of chemical moieties in BT (bridging tetrahedral silicate chain) and IC (interlayer cation exchange) sublattices, *i.e.* sets of structurally equivalent sites. The solid solution model includes 20 end members describing the chemistry of the Ca-Si-K-Na-Al-Fe-Si-H_2O system (see section 6.5).

1.4 Repository near-field

1.4.1 Repository chemistry

Dissolution of spent fuel and vitrified nuclear waste defines the radionuclides release after breaching of the disposal casks containing high-level radioactive waste. Because of its high importance, this source term has been intensively studied for decades. In the framework of the Horizon 2020 EU project DisCo (Modern spent fuel Dissolution and chemistry in failed Container conditions) LES is developing thermodynamic models of UO_2 fuels under in-pile conditions. The objective is to assess whether or not dopants such as chromia (Cr_2O_3) could lead to higher oxygen potentials in UO_2 fuel. The role of doping and impurities on the *in situ* conditions was analysed by means of a refined thermodynamic model (see section 5.3).

Phosphorous species and salts of phosphorous acid play an important role in the thermodynamic control of the solubility of actinides and fission product. Recently, a large number of aqueous and solid phosphor bearing species were included in the updated version of the PSI chemical thermodynamic database. The importance of phosphate species for the *in situ* conditions in the HLW repository near-field and the solubility of spent fuel and cladding was re-evaluated using the extended database.

It could be shown that a proper consideration of phosphate species in the calculations results in a reduction of Ca and phosphate concentrations by nearly two orders of magnitude. This change in the aqueous chemistry is, however, not sufficient to hinder the precipitation of $PuPO_3$(cr), which remains the solubility-limiting phase for Pu. The equilibrium Pu concentration raises by more than two orders of magnitude compared to previous estimations conducted with an incomplete thermodynamic database, but still remains below the picomolal level. Phosphorus is a minor element in steel, and the amount released after corrosion of the canister seems to be insufficient to induce precipitation of apatite and $PuPO_3$(cr) (see section 2.2.2).

The anoxic corrosion of activated steel in the near-field of a low- and intermediate long lived radioactive waste (L/ILW) repository leads to the release of ^{14}C-containing low molecular weight (LMW) carbon compounds. The high mobility of ^{14}C-carrying gaseous and dissolved compounds is attributed to their weak interaction with mineral surfaces in the far-field. The chemical form of the ^{14}C-carrying species dictates the routes of ^{14}C migration in the engineered barrier system of a deep geological repository and the surrounding host rock, and therefore determines the long-term contribution of ^{14}C to dose release from a repository for radioactive waste. To support future safety assessments, a laboratory-scale experiment is being carrying out with the aim of identifying and quantifying the ^{14}C-bearing carbon compounds released during corrosion of irradiated steel in anoxic and highly alkaline conditions. The latter conditions simulate the long-term chemical environment in a cement-based L/ILW repository. Since May 2016, a long-term corrosion experiment with irradiated steel is running and allows a regular sampling of both the liquid and gas phases in the reactor. In parallel LES has completed the development of the sampling and measurement protocol for compound specific analysis in the gaseous and liquid phase. The measurements are performed with an on-site liquid and gas chromatography separation system and off-site characterisation of ^{14}C content in each species by accelerated mass spectrometry. This coupled measurement system allows to achieve the detection limit of 10^{-14} M. Such a

compound-specific radiocarbon analysis (CSRA) was developed in co-operation with the Department of Chemistry & Biochemistry at the University of Bern, Switzerland).

A systematic CSRA was applied to the solutions and gas phases sampled in 2019 and 2020. ^{14}C-carrying carboxylic acids (formic acid, acetic acid, malonic acid, oxalic acid and lactic acid) were found to be the main carbon compounds contributing ~ 50 % to the TO^{14}C. Thanks to CSRA developed for the gas phase in the last two years, ^{14}C-bearing hydrocarbons (HCs) produced in the anoxic corrosion experiment with irradiated steel, have been identified for the first time. Only two HCs were quantified in the gas phase of the reactor, $^{14}CH_4$ and $^{14}C_2H_6$. $^{14}CH_4$ was the most abundant one, corresponding to the total ^{14}C content in the gas phase within the uncertainty range, whereas the $^{14}C_2H_6$ concentration was found to be close to the detection limit of the analytical method. The measured release of $^{14}CH_4$ by homogenous corrosion of irradiated steel seems to proceed at a rate of ~ 1 nm/a. This rate is in agreement with corrosion rates reported for stainless steel in anoxic, strongly alkaline conditions (see section 5.2.1-5.2.4).

1.4.2 Clay systems

Solid/liquid distribution coefficients (K_d values) are applied to estimate the retention of radionuclides in the engineered barriers and host rocks in the safety analysis of deep geological radioactive waste repositories. In order to derive adsorption values for argillaceous rocks under a wide range of porewater and mineralogical compositions, the so-called bottom-up approach is applied. This approach assumes that the uptake of radionuclides in complex mineral/porewater systems can be quantitatively predicted from the knowledge and understanding of the mechanistic adsorption processes on single minerals, and the models developed to describe them. In the reporting year, this approach has been applied to estimate the uptake of Cs^{I}, Ni^{II}, Eu^{III}, Th^{IV} and U^{VI} by Opalinus Clay samples from the Bülach1-1 drill core and compared with experimental K_d values. For all elements, except for Th the results of blind predictions are within the error bars of the experimental data points. The measured K_d values for Th show high scatter and are systematically higher than the results of blind predictions. The reason for the discrepancy is the very low Th concentration close to detection limit making accurate measurements challenging (see section 3.1).

The current sorption model used in the safety assessment assumes reversibility of sorption. Relevant open questions are related to adsorption reversibility and to the mechanisms that control the retention of radionuclides in the long-term. Among other activities, LES conducts wet chemical and spectroscopic investigations on the reversibility of Ni and Zn on 2:1 clay minerals. First results from adsorption/ desorption experiments of Zn on illite (illite du Puy, IdP) have become available in 2020 (see section 3.4.1).

Clay minerals such as illite, smectite, illite/smectite mixed layers and kaolinite are main components of consolidated argillaceous host rocks. Success of the bottom-up approach depends on the correct assignment of the solid phases responsible for radionuclides uptake in host rocks. Within an EU-funded COFUND project, micro-spectroscopic techniques are applied to verify whether adsorption is taking place on the clay fraction or on other minor phases. The precise nature of the retention mechanism (*i.e.*, adsorption, neo-formation, co-precipitation) in both dispersed (extracted fraction) and compacted systems (thin sections) will be investigated with bulk-XAS. In 2020, several samples of montmorillonite (SWy), Illite (IdP) with different metal loadings were prepared for further investigations. Thin sections of Opalinus Clay samples were placed in contact with U containing solutions in different redox states, and also with Th^{IV}. The micro-XRF/XAS measurements and evaluations of spectra are ongoing (see section 3.6).

The surface complexation of metals on clay minerals is closely related to the reactivity and dissolution/ precipitation processes at the edge sites of the clay platelets. The surface complexation can also serve as a precursor for the neo-formation of phyllosilicates. Within the SNSF PhD project of René Schliemann, ab initio molecular dynamics simulations were applied to directly evaluate the dissolution mechanism and the activation energy of Al and Si leaching from idealized (110) and (010) edge surfaces of pyrophyllite. The simulations provide a mechanistic insight into atomic scale details of leaching of tetrahedral and octahedral units at phyllosilicate surface and explains the molecular scale reasons of the pH-dependent dissolution kinetics of smectite minerals (see section 7.5).

The composition of clay rock porewater is mainly controlled by the solubilities of mineral phases and exchange or complexation processes taking place at the mineral surfaces. Because of the inherent difficulties related to the extraction of porewater from clay rocks in its pristine equilibrium composition, the composition of synthetic clay porewaters is defined based on thermodynamic calculations. The result of such modelling cannot, however, be readily verified. New experiments were therefore carried out, in which the consistency between solution composition and the cation occupancy of Opalinus Clay was assessed in order to test the applicability of the underlying thermodynamic datasets. In these experiments,

Opalinus Clay rock samples were re-saturated with two synthetic porewaters exhibiting different concentrations of alkali and earth-alkaline elements. The concentrations of the most important constituents of the solution phases were monitored periodically by ion chromatography during the two re-saturation steps. Measured evolution of the solution concentrations was used to estimate model parameter for predicting pore water composition by thermodynamic modelling (see section 3.2).

Significant quantities of gas are expected to be generated in a repository, either by corrosion of metallic materials or due to degradation of organic waste compounds. Molecular diffusion is an important gas dissipation mechanism helping to reduce potential pressure build up in the repository near-field. Diffusion studies of gas molecules in fully and partially saturated compacted clay systems is ongoing in the framework of a Marie Skłodowska-Curie COFUND fellowship partially co-funded by the EU. A new diffusion cell was developed and coupled to the portable Mini-Ruedi mass spectrometric (MS) system developed in the group of Prof. Rolf. Kipfer at Eawag. First results for the diffusion of helium (He) in fully saturated compacted Volclay could be obtained. The molecular mechanism of the gas transport at saturated and partially saturated conditions is further investigated by molecular dynamics simulations within the European project Eurad WP GAS. First simulations have been set up to evaluate the mobility of gaseous species as function of clay compaction (see section 4.5).

1.4.3 Cement systems

The LMW organic compounds such as ^{14}C-carrying formate and ^{14}C-carrying acetate detected in the corrosion experiments are thermodynamically unstable and their oxidation to $^{14}CO_2$ or reduction to $^{14}CH_4$ would result in the undesired release of ^{14}C from the repository via the gas phase. Experimental studies of LMW decomposition confirmed that formate decomposition is very slow at ambient temperature while it is accelerated with increasing temperatures and in the presence of $Ca(OH)_2(s)$ and Fe-powder. The outcomes of these experiments were compared with the results from thermodynamic carbon speciation calculations performed with the Gibbs Energy Minimization code (GEM-Selektor). In all cases, it is predicted that, at thermodynamic equilibrium, the large portion of formate is decomposed and only a very small fraction of the initial formate concentration is present. The major decomposition product is carbonate, thus confirming the observations from the experiments. (see section 5.2.5).

1.4.4 Interface processes

Cement and clay materials are characterized by different porewater chemistry. Chemical interaction between these materials results in dissolution-precipitation reactions of minerals that may alter the transport properties at their interface. The evolution of materials at the interface is of relevance for the long-term safety assessment of underground radioactive waste repositories. Chemical and mineralogical changes at the OPA-ESTRED and OPA-OPC interfaces after 2 years of interaction were analysed by SEM/EDX imaging. OPA-OPC interfaces are characterised by portlandite dissolution close to the contact plane with clay (due to pH decrease). This leads to Ca^{2+} diffusion into the Opalinus Clay creating a region of ~1.5 mm enriched in calcium. At the OPA-ESDRED interface, a magnesium enrichment is observed within the first mm of the clay. Based on complementary modelling it could be confirmed that Ca and Mg are transported from the cement to the OPA compartment and precipitate as C-S-H and M-S-H (Magnesium silica hydrates), respectively. The comparison of these two systems illustrates that the course of mineralogical alteration depends on the starting compositions of the cement and clay (see section 2.2.1).

Alkali-silica reaction (ASR) is one of the most important concrete durability issues worldwide. The sorption properties of ASR are barely known experimentally. A comparative study of C-S-H and ASR sorption properties was conducted using reactive Grand Canonical Monte Carlo simulations. The simulations show that differences in the protonation state of the surface sites, evolution of surface charge and pH dependent ion adsorption are largely determined by the distinct surface site densities in both phases. The density of the titratable ≡SiOH surface sites on C-S-H is nearly two times larger than that of ASR product. Since ion adsorption is primary driven by electrostatic interaction of ions with the charged surface sites, C-S-H have higher sorption capacities than the ASR products. Further, the modelling suggests that the ζ-potential of the ASR product remains weakly negative at the most relevant conditions (see section 7.6).

1.5 Repository far-field

Application of electrical double layer models for the transport of ions near the planar surfaces of charged clay minerals (“EDL diffusion”) has shown to provide a robust description of diffusion as function of ionic strength and pH conditions. This concept also takes into account competition effects between different metal cations in the solution and EDL. The fraction of mobile surface species is therefore, directly affected by

the presence of competing species in the bulk aqueous phase. Such effects may be of particular importance in the process of compiling diffusion databases for repository conditions. The majority of available diffusion experiments performed on pure clay minerals were obtained using simple electrolytes such as NaCl or $NaClO_4$. To upscale the diffusion coefficients of surface complexing ions to repository conditions, it is imperative to understand the effects of sorption competition between cations with higher valence, present in electrolyte. Diffusion experiments with different test radionuclides are therefore conducted using compacted illite under variable concentrations of Ca^{2+} in a given NaCl electrolyte. Blind predictions of the effective diffusion coefficients (D_e) and the respective sorption distribution ratios (R_d) for such experiments are validated against preliminary experimental data (see section 4.2).

Further development of the modelling setup for a modified in-/out-diffusion method, which allows to measure diffusion parameters using small samples of compacted clay minerals has been accomplished and tested within the Eurad project FUTURE based on the data from existing experiments. This technique shall be applied in a later phase of the work on size-fractionated vermiculite. Those experiments will be carried out in close collaboration with partners from the University of Poitiers, who kindly provided this material to PSI (see section 4.3).

1.6 Model development, code benchmarking, advanced analytical tools, thermodynamic databases

In order to have a better estimate of the uncertainty in sorption model parameters, the GEMSFITS code was extended to perform Monte Carlo based parameter estimations. The developed version of the code can refine the equilibrium constants for surface complexation and ion exchange to obtain best agreement between measured and calculated values for all used datasets. For evaluating the parameter uncertainty intervals of adjusted parameters, GEMSFITS uses the Monte Carlo sampling method. Future work is planned to refine the surface complexation constants of other elements, to provide 95% confidence interval parameter uncertainties, and to make them consistent with the updated version of the PSI/Nagra database (see section 3.3).

Reactive transport simulations are the main tool applied for the long-term performance assessment of repository *in situ* conditions and the geochemical evolution of the repository near-field. The coupled THMC simulations of large special domains performed for a long-time scale are particularly challenging due to memory requirements and high computational costs. The performance analysis indicates that in traditional THMC-coupled codes, more than 70% of computational resources are assigned to the calculations of geochemical equilibria. Therefore, any performance improvement of the geochemical modelling modules may have a big impact on the performance of the coupled codes. In this context, machine learning and Artificial Neural Networks (ANN) can be efficiently used to build data driven surrogate models for geochemical modelling. Recently we have applied ANN to simulate reactive transport processes in a microfluidic experiment and benchmarked the results against the conventional Law of Mass Action (LMA) method and the open-source software GEMS. The implemented ANN approach provides a 165× speedup with respect to a highly optimised LMA code without any loss in accuracy. Such a two order of magnitude improvement in the computational performance opens up opportunities for the development of reliable digital twin models for reactive transport phenomena in laboratory and field experiments (see section 2.3.1).

The development of advanced Lattice Boltzmann based models for the simulation of electrochemically coupled transport of ions in surface charged porous media under saturated and partially saturated conditions has been continued within the Eurad WP4-DONUT. The exchange visit of Dr. Yuankai Yang from FZ-Julich (IEK-6) to PSI was supported by the Eurad mobility scheme. During this exchange visit, a generic coupled numerical framework for 3D simulation of ion transport in unsaturated porous media was established. (see section 2.3.2).

Chemical thermodynamic modelling is widely applied to elucidate the impact of various factors such as klinker composition, hydration, leaching, or temperature on the speciation and the properties of hydrated cementitious systems. Available general-purpose geochemical codes such as GEM-Selektor (gems.web.psi.ch) have versatile but complex user interfaces, which require advanced knowledge of chemical thermodynamics, and demand a considerable training effort. Hence, there is a clear need for a dedicated tool for cement modelling, which can be used by students or non-chemists working on cements with minimal requirement of previous experience. To meet this need, CemGEMS (https://cemgems.app) – an open access easy-to-use web-application has been developed to assist cement chemists, students and researchers in easily performing and visualizing of thermodynamic models of hydration of cementitious materials. CemGEMS can be viewed as a “proof-of-concept” for further development of web-based tools dedicated for specific applications of chemical thermodynamic modelling by the GEM method (see section 2.4).

Thermodynamic properties of materials can be predicted from first principle quantum mechanical calculations. Such calculations are very demanding. Moreover, the accurate calculations must include an harmonic effects, which depend on the full interaction potential between atoms in the system. Recently, the Decoupled Anharmonic Mode Approximation (DAMA) which is based on a full-potential representation of inter-atomic interactions along the eigenmodes was extended to the reciprocal space in order to enable a more efficient calculation of the phonon dispersion and the phonon density of states (DOS) in solids. The new implementation of q-DAMA allows not only the examination of high temperature phases of crystals, which often show multiple energy minima at the Potential Energy Surface (PES), but also to take into account higher order corrections in the thermo-dynamic properties. The successful bench-marking of q-DAMA against experimental data and other simulation techniques encourages its application to materials with strong anharmonic behaviour, including those with soft modes (see section 7.4).

Within the Swissnuclear funded collaborative project "*Multi-scale numerical prediction of boiling crisis*", the development of multiscale computation fluid dynamics is continued in collaboration with the Laboratory for Scientific Computing and Modelling at PSI (LSM-PSI). A hybrid thermal LB model was further developed to account for the conjugate heat transfer near rough solid sun faces. This model will allow a direct simulation of the nucleate pool boiling and to provide key relationships between nucleation site density and different hydrodynamic parameters, which would serve as input for PSI-Boil (see section 2.5.1).

1.7 Disposal of conventional waste and fundamental aspects of mineralogy

PSI/LES and the Institute for Geological Science at the University of Bern (UBERN/IfG) have long-standing collaboration in the field of environmental mineralogy and applied geochemical engineering. The research of the Mineralogy Group at the University of Bern covers fundamental and applied aspects of mineral dissolution and precipitation, chemical factors of crystal structure stability and temperature driven phase transitions in minerals. The dedicated laboratories operated by the group are equipped with powder and single crystal diffractometers for structural studies of minerals, and with an atomic force microscope for *in situ* characterisation of mineral surfaces. The experimental studies are widely supported by modelling activities.

The Competence Centre for Secondary Raw Materials (CCSRM, Project Leader Dr. U. Eggenberger) is embedded in the Mineralogy group and conducts applied research in the field of environmental geochemistry and secondary raw materials. The core competences of the CCSRM cover the topics of circular economy and disposal quality of conventional non-radioactive waste materials. Geochemical aspects and challenges related to the *in situ* conditions in conventional and radioactive waste disposal rely on common scientific background and modelling tools. Shared expert knowledge provides the fruitful basis for collaboration and mutual synergies between LES/PSI and CCSRM/UniBern. Recently, CCSRM has established a project collaboration with the Wyss Academy for Nature (www.wyssacademy.unibe.ch) on the topic of circular economy.

Approximately 6 million tons of solid municipal waste are incinerated annually in Switzerland. Nearly half of the incinerated residuals is disposed in landfill sites. Potentially, these deposits might be enriched in heavy metals and/or other hazardous chemicals. In accordance with the new regulatory requirements, the acid filter and fly ash washing technology (FLUWA) is applied for metal recovery, before disposal. The FLUWA operation conditions and the efficiency of metal recovery depend on the composition of the input ashes. The FLUWA process optimisation and its application to different incineration residues is investigated in several PhD projects supported by industrial and federal agencies (see section 8.2-8.5).

Heavy-metal-exchanged zeolites are attractive materials that find applications in several research fields, from environmental remediation to catalysis. The SNSF-AMBIZIONE project, led by Dr. G. Cametti, investigates the structural changes taking place in natural zeolites as a function of heavy metal uptake by combining experimental methods (X-ray diffraction, X-ray absorption spectroscopy) and theoretical computations (MD simulations). These complementary approaches are highly successful in structural characterisation of complex systems, where the charge compensating cations are usually affected by strong positional disorder (see section 7.3).

Several hazardous metals are known to form insoluble carbonate minerals. Their solubility products are up to five orders of magnitude lower than abundant materials like magnesite, calcite, aragonite and dolomite. These highly abundant Ca and Mg carbonate minerals can be used for remediation of contaminated waters and binding of hazardous metal as insoluble carbonates. In a number of complementary MSc and BSc projects the kinetics and molecular mechanisms of Pb^{2+} interaction with various carbonate polymorphs was investigated. The aim of these studies was to understand the effects of annealing, ionic strength, pH and temperature on the kinetics of Pb^{2+}-carbonate precipitation (see section 7.2).

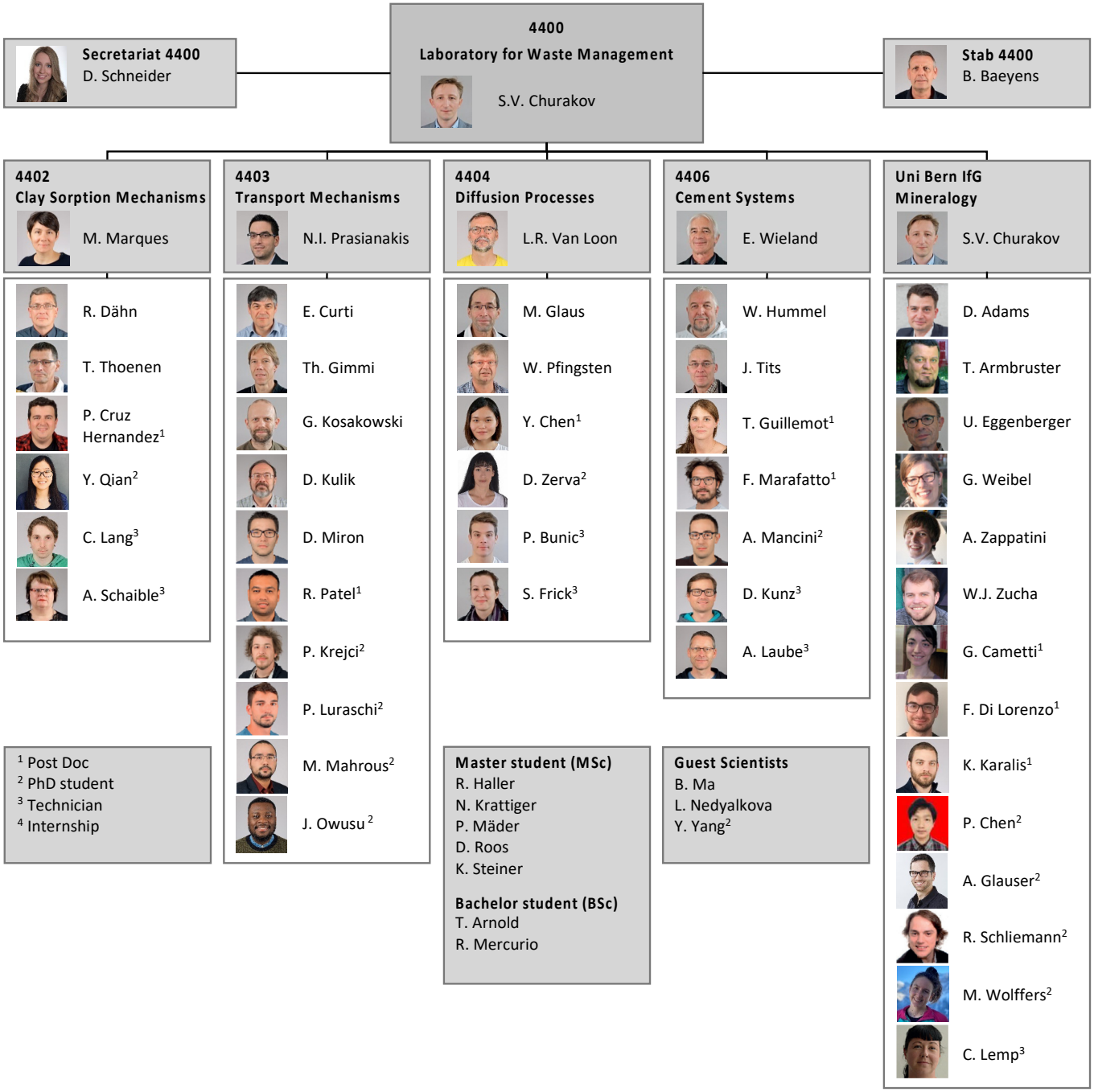

Fig. 1.1: Organisational chart of LES.

2 GEOCHEMICAL EVOLUTION OF REPOSITORY SYSTEMS

Prasianakis N.I., Churakov S.V., Curti E., Gimmi T., Pfingsten W., Kulik D., Miron D., Patel R.(postdoc), Luraschi P.(PhD student), Mahrous M. (PhD student), Haller R. (MSc student)

2.1 Introduction

This project aims at developing cross scale THMC-numerical models and simulation tools for describing the long-term evolution of the multi-barrier repository system and geotechnical engineering. This expertise is essential for the safety assessment and cross comparison of various repository designs as a part of the site selection process in the Sectoral Plan for Deep Geological Disposal (SGT) Stage 3, and the following general license application. Geotechnical engineering is a steadily growing research field aiming at optimization of the subsurface reservoirs properties, for geothermal energy production and for resource exploration.

The project is focusing on three main topics: 1) Experimental characterization and numerical modelling of the evolution of the technical barriers and their respective interfaces e.g. cement evolution and cement-clay interaction; 2) Fundamental understanding of reactive transport mechanisms including sorption through multiscale modelling and upscaling techniques; 3) The benchmarking and application of state-of-the-art coupled codes as well as the development and coupling of thermodynamic modelling and database tools. Overarching thematic contributions and modelling support is provided in the area of contaminants retention and transport in host rock, heterogeneities, uncertainties and diffusion in disperse/compacted systems.

In the area of repository design and the temporal evolution of the repository *in situ* conditions, the study of the evolution of cement-clay interfaces, are continuing. Within the Nagra supported PhD project: "*Evolution of transport properties, mineralogy, and porosity of cement-clay interfaces*" (P. Luraschi), the interaction between various cement types and Opalinus Clay (OPA) was investigated using several analytical methods. After a 2-year period of interaction, the cement-clay samples were investigated using several analytical methods. Focus was given to the evolution OPA-OPC cement interaction and OPA-ESDRED (lower pH) mortar. The different compositions of the two cements resulted in different microstructure evolution and precipitants at the clay side.

Recently, a review of thermodynamic data for phosphorous species has been conducted. The effect of phosphate on pore water chemistry inside a breached canister in contact with spent fuel has been evaluated using updated thermodynamic database. It was confirmed that despite apatite precipitation, Pu(III) phosphate remains to be the solubility Pu phase inside the canister and maintains very low Pu concentrations.

Within the SNSF PhD project "*Resolving dissolution-precipitation processes in porous media: Pore-scale Lattice Boltzmann modelling combined with synchrotron based X-Ray characterization*" (M. Mahrous), and the EU project Eurad WP4-DONUT funding from the European Union's Horizon 2020 research and innovation programme under grant agreement no. 847593, the pore-level reactive transport modelling capabilities have been enhanced using machine learning techniques and more specific artificial neural networks (ANN). Chemical calculations were accelerated by four orders of magnitude during high performance computing simulations with no loss in accuracy. The efficiency and accuracy were demonstrated after implementing the ANN technique in the digital twin of a microfluidic lab-on-a-chip experiment conducted at FZ-Jülich. The overall calculations were significantly accelerated.

Within the EU project Eurad WP4-DONUT Mobility scheme and in the realms of collaboration between PSI and FZ-Julich (IEK-6), Dr. Yuankai Yang visited PSI to investigate the ion diffusion in unsaturated nanoscale porous media via multiscale simulations. A multi-model framework was established and the influence of water films on ion transport within nanoclays has been assessed.

GEM Software (GEMS, lead scientist D. Kulik) development has been continued and a leap towards web-based dedicated tools has been completed. To cover the needs of a dedicated tool, easy to learn and to use for students or non-chemists working on cements, and with little to no maintenance efforts, the CemGEMS (https://cemgems.app) web application was developed within a project funded by NANOCEM. CemGEMS web application can potentially model cement leaching, degradation and salt attacks, it can be used with benefits in (radioactive) waste management studies in addition to applications in cement research and industrial engineering.

Several diversification projects are currently on-going, based on the advanced modelling capabilities that exist at LES. In the realms of a collaborative project with the Laboratory for scientific computing and modelling at

PSI (LSM-PSI) and under the umbrella of Swissnuclear funding agency through the project "*Numerical prediction of boiling crisis considering surface characteristics*" (R. Patel), the fundamental understanding of boiling processes from atomistic to reactor scale is pursued. Also, an industrial research project with the pharmaceutical company "*GlaxoSmithKline*" has been continued in 2020.

2.2 *In situ* conditions in repository near-field

2.2.1 Interactions at cement-clay

Cement and clay materials are characterized by different porewater chemistry. Chemical interaction between these materials results in dissolution-precipitation reactions of minerals that may alter the transport properties at their interface. The evolution of these interface properties is of relevance for the long-term safety assessment of the underground radioactive waste repositories.

Depending on the interface type (*i.e.* the materials that are in contact) competing dissolution precipitation reactions lead to a change in the diffusive transport pathway across the interface. Experimental and modelling studies of the alteration processes at different interface types improve the model based description of reactive transport processes and ensure the optimal repository design. As a further development of the cement-clay interaction project, several interface samples of different material composition were prepared and let interact under nitrogen atmosphere.

After a 2-year period of interaction, the cement-clay samples were investigated using several analytical methods. Fig. 2.1 shows the SEM/EDX comparison of the mineralogical evolution of Opalinus Clay after 2-year contact with high porosity OPC cement paste or with ESDRED (low alkali, lower pH) mortar. The two cements have a different chemical composition, which results in a different alteration on the clay. OPC paste mineralogy is dominated by Portlandite [$(CaOH)_2$] and C-S-H (Afm and Aft are present in minor amount), with pH of ~13. ESDRED mortar does not contain Portlandite but substantial amounts of quartz grains and has a pH of ~11.

Backscatter images (BSD maps) give a general overview on the two different interfaces types showing compositional and structural differences. On the clay side, fossils and some cracks are visible (mostly parallel to the bedding plane). The high porosity OPC paste is often fractured (due to the drying technique) and shows some darker regions, where resin entered the pore space. Sand grains (quartz and feldspars) are well recognizable on the ESDRED side. SEM/EDX maps allow obtaining chemical information regarding the two samples. OPA-OPC interfaces are characterised by portlandite dissolution close to the contact with clay (due to pH decrease). This fact leads to Ca^{2+} diffusion into the Opalinus Clay creating a region of ~1.5 mm enriched in calcium (orange dashed line). When OPA gets in contact with ESDRED cement, a magnesium enrichment is observable within the first mm of the clay (yellow dashed line). According to experiments

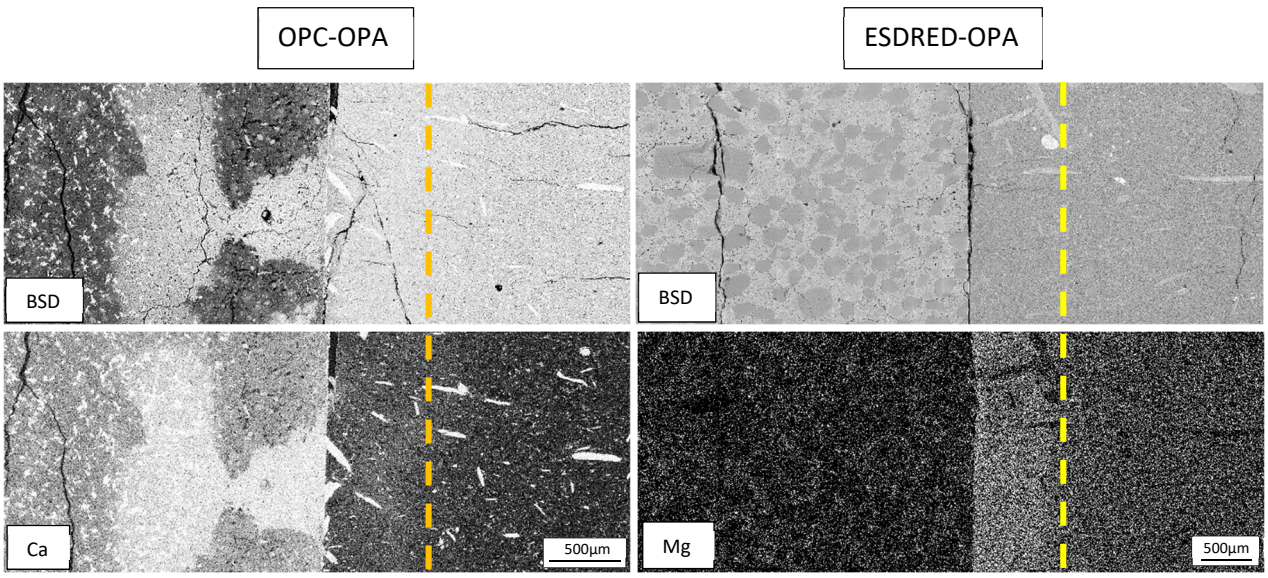

Fig. 2.1: SEM/EDX maps of OPC-OPA and ESDRED-OPA interfaces. Upper two images are taken with the backscatter detector (BSD) allowing recognizing some chemical and structural features. The two lower images show EDX maps of Calcium (left) and Magnesium (right). Ca maps shows Portlandite dissolution in the OPC paste and calcium enrichment on the OPA side. Mg EDX maps indicate a Mg enriched zone close to the contact with ESDRED. Mg maps of the OPC-OPA interface and Ca maps for the ESDRED-OPA interface do not show significant changes.

performed by other research groups, Ca in solution diffuses and precipitate as C-S-H inside the Opalinus Clay, whereas Mg forms M-S-H (Magnesium silica hydrates). The comparison of these two systems illustrates the different mineralogical alteration depending on the starting composition (of the cement but also of the clay).

2.2.2 Effect of phosphate on pore water chemistry inside a breached canister in contact with spent fuel

Earlier versions of the thermodynamic database for radionuclide solubility calculations contained only few phosphorous species and salts of phosphorous acid, namely the phosphoric acid dissociation constants and complexation/solubility data of a few actinides (U, Th, Np, Pu, Cm) and fission products (Ni, Zr). The use of limited database may lead to biased results in equilibrium calculations involving phosphorous due to missing major-element species, e.g. Mg and Ca complexes and solids. Recently, a thorough review of thermodynamic data for phosphorous was carried out at LES (Hummel and Curti 2020). Based on the review, a large number of aqueous and solid phosphor baring species have been selected and included into the updated version of PSI chemical thermodynamic database to be released by the end of 2020.

The effect of introducing the newly selected phosphate data is shown by updating a previously published pore water calculation described in Section 9-5.2 / Table 9-3 of Bradbury et al. 2014 (labeled *Eq3a*). The purpose of the calculation was to predict the aqueous and mineral speciation at equilibrium in the complex environment inside the canister of the planned Swiss HLW repository, taking into account the effects of the corrosion of spent fuel, Zircaloy cladding and steel canister. The only source of phosphorous in the simulation is the steel canister, assumed to contain 450 ppm of phosphor in elemental form. A scenario was selected in which the canister breaches spontaneously and pore water intrudes instantaneously from saturated bentonite, filling completely the open interspaces at the canister/waste package interface. The pore water composition was taken from Kosakowski and Berner (2011) and represents an average composition computed for the assumed canister breaching time, 10'000 years after repository closure. The intruded pore water was then equilibrated with 1 mole % of the canister material (partially corroded to magnetite) and with small amounts of spent fuel and Zircaloy (scaled to the respective corrosion rates).

In the original calculation, an extremely low Pu concentration limit of 10^{-15} M was calculated, arising from Pu(III)PO_4 precipitation combined with a high dissolved phosphate concentration. The high phosphate concentration was a consequence of the absence in the database of major solids, that could limit phosphate aqueous concentrations in the system of interest, e.g. $Ca_5(PO_4)_3OH$(cr) (hydroxi-apatite).

In order to test the impact of the newly selected P species and solids, the *Eq3a* calculation was updated (*Eq3a_new*) after introducing and activating manually the new P data (Table 2.1) into the current database version (12/07) as implemented in GEM-Selektor (v. 3.7.0). For consistency, the original calculation was repeated (*Eq3a_old*) using the same input recipe and the same GEM-Selektor version, but with the newly selected phosphorous species switched off. The resulting equilibrium concentrations and the list of stable solids is shown in Table 2.2. As anticipated, hydroxy-apatite precipitates when the new phosphate data are included, reducing both Ca and phosphate concentrations by about two orders of magnitude. The reduction in dissolved phosphate is nevertheless not sufficient to prevent precipitation of $PuPO_3$(cr), which remains the solubility-limiting phase for Pu. The Pu concentration raises by more than two orders of magnitude but remains below the picomolal level. Therefore, the conclusion drawn in Bradbury et al. (2014), that the solubility of Pu inside the canister should be constrained to very low concentrations by Pu(III) phosphate precipitation is confirmed in the

Tab. 2.1: Phosphate complexation and solubility constants implemented in GEM-Selektor v. 3.7.0 for the recalculation of Eq3a equilibrium. Sparingly soluble solids and complexes (irrelevant for this system) are not shown.

Reaction	**$\log_{10}K^o$** (298.15 K)
$Na^+ + PO_4^{3-} \rightleftharpoons NaPO_4^{2-}$	1.56 ± 0.17
$Na^+ + HPO_4^{2-} \rightleftharpoons NaHPO_4^-$	1.03 ± 0.07
$Na^+ + H_2PO_4^- \rightleftharpoons NaH_2PO_4$(aq)	0.30 ± 0.17
$K^+ + PO_4^{3-} \rightleftharpoons KPO_4^{2-}$	1.46 ± 0.16
$K^+ + HPO_4^{2-} \rightleftharpoons KHPO_4^-$	0.88 ± 0.07
$K^+ + H_2PO_4^- \rightleftharpoons KH_2PO_4$(aq)	0.29 ± 0.16
$Mg^{2+} + PO_4^{3-} \rightleftharpoons MgPO_4^-$	4.9 ± 0.50
$Mg^{2+} + HPO_4^{2-} \rightleftharpoons MgHPO_4$(aq)	2.73 ± 0.06
$Mg^{2+} + H_2PO_4^- \rightleftharpoons MgH_2PO_4^+$	1.11 ± 0.20
$Ca^{2+} + PO_4^{3-} \rightleftharpoons CaPO_4^-$	6.46 ± 0.11
$Ca^{2+} + HPO_4^{2-} \rightleftharpoons CaHPO_4$(aq)	2.58 ± 0.05
$Ca^{2+} + H_2PO_4^- \rightleftharpoons CaH_2PO_4^+$	0.99 ± 0.09
$Sr^{2+} + H_2PO_4^- \rightleftharpoons SrH_2PO_4^+$	5.62 ± 0.20
$Sr^{2+} + HPO_4^{2-} \rightleftharpoons SrHPO_4$(aq)	2.35 ± 0.12
$Sr^{2+} + H_2PO_4^- \rightleftharpoons SrH_2PO_4^+$	0.69 ± 0.20
$Ca_5(PO_4)_3OH$(cr) $\rightleftharpoons 5\ Ca^{2+} + 3\ PO_4^{3-} + OH^-$	-58.29 ± 0.15
$Ca_5(PO_4)_3Cl$(cr) $\rightleftharpoons 5\ Ca^{2+} + 3\ PO_4^{3-} + Cl^-$	-46 ± 5.00

Tab. 2.2: Comparison of pore water calculation for in-canister conditions, including (Eq3a_new) and excluding (Eq3a_old) the new selected phosphate data. Only major components and significantly divergent results are shown.

	Eq3a_new	***Eq3a_old***
pH	7.39	7.53
Eh(Volt)	-0.436	-0.445
I(mol/kgw)	0.258	0.275
Total element molalities		
Al	8.92E-09	1.60E-08
Ba	1.09E-07	1.13E-07
C	1.18E-05	1.55E-05
Ca	2.64E-04	9.93E-03
Cl	1.75E-01	1.75E-01
Fe	8.39E-03	4.35E-03
K	1.33E-03	1.33E-03
Mg	5.61E-03	5.61E-03
Na	2.09E-01	2.09E-01
Ni	8.91E-04	6.04E-04
P	4.93E-05	5.85E-03
Pu	4.36E-13	1.45E-15
Ra	1.92E-10	1.98E-10
S	3.28E-02	3.28E-02
Se	1.82E-08	2.53E-08
Si	1.81E-04	1.82E-04
Sn	1.33E-08	1.46E-08
Sr	6.20E-05	6.20E-05
Saturated (+), supersaturated (++) and undersaturated (---) solids		
kaolinite, $Al_2Si_2O_5(OH)_4$	+	---
Ra-baryte, $(Ba,Ra)SO_4$	+	+
OH-apatite, $Ca_5(PO_4)_3OH$	+	++
Pu(III) phosphate, $PuPO_3$	+	+
magnetite, Fe_3O_4	+	+
siderite, $FeCO_3$	+	+
tugarinovite, MoO_2	+	+
theophrastite, $Ni(OH)_2$	+	+
NpO_2(am)	+	+
ferroselite, $FeSe_2$	+	+
quartz, SiO_2	+	+
cassiterite, SnO_2	+	+
$TcO_2(H_2O)_{1.6}$	+	+
UO_2(am,hyd)	+	+
baddeleyite, ZrO_2	+	+

updated *Eq3a_new* calculation, in spite of apatite precipitation. Although phosphorus is a minor element in steel, the amount released through aqueous corrosion of the canister seems to be sufficient to induce precipitation of apatite and $PuPO_3$(cr). Indirect experimental evidence for the precipitation of sparingly soluble actinide(III) phosphates in a similar system is provided by Curti et al. (2006) who detected REE(III)-phosphate nanoparticles in the corrosion products of nominally phosphor-free borosilicate glass leached during 12 years in stainless steel containers.

2.3 Fundamental understanding of reactive transport and sorption mechanisms

2.3.1 Acceleration of Geochemical Speciation Calculations for Reactive Transport Simulations

Reactive transport simulations play a key role in process understanding and modelling of the geochemical evolution of waste repositories. These simulations include diffusive / advective mass transport, solute transport, and homogeneous and heterogeneous chemical reactions calculations. The main computational cost is the homogeneous reactions in the aqueous phase (Geochemical Speciation Calculations), which consumes 70%-99% of the total simulation time. In 2020, the geochemical speciation calculations of a $SrCl_2$-Na_2SO_4 system were accelerated using the Look-up table method and with machine learning (Artificial Neural Networks (ANN)). Results were compared against the conventional Law of Mass Action (LMA) method and the open-source software GEMS. Figures 2.2 and 2.3 show a comparison of the geochemical acceleration methods compared to the conventional LMA method in terms of accuracy. It is shown that, without any loss in accuracy, the ANN and Look-up table methods can be several orders faster than LMA. The ANN approach shows

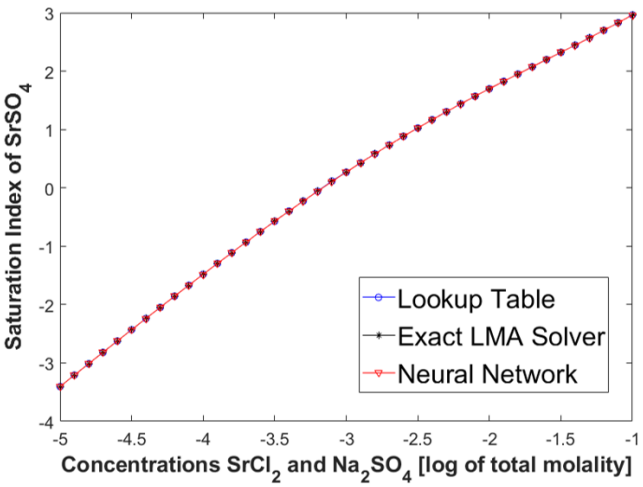

Fig. 2.2: Comparison of accuracy of the used acceleration methods (Look-up table and artificial neural networks) against the conventional Law of Mass Action method in calculating the saturation index of celestine ($SrSO_4$) mineral for different concentrations of $SrCl_2$ and Na_2SO_4. Lookup table was populated with data from the exact LMA solver. The ANN was trained on the look-up table data.

clear advantages, in terms of memory, throughput when the dimensionality of the chemical system increases. However, the training of high dimensional neural networks remains challenging. The acceleration methods were further implemented in a full reactive transport simulation of celestine ($SrSO_4$) precipitation and for several thousands of timesteps to assess the performance in realistic simulation setups. A multiscale multiphysics numerical simulation describing the mass transport, nucleation, mineral precipitation and dissolution within confined spaces has been setup and tested against experimental data, in collaboration with the nuclear waste management and reactor safety laboratory at Forschungszentrum Jülich (FZ-Jülich), Germany. The experimental data stemmed from a microfluidic lab-on-chip experiment conducted at the experimental facilities of the FZ-Jülich. More specific, during runtime the NN managed to have a sustained throughput of 13 Million calculations of Saturation Index per second, while the GEMS output was ~1000 calculations per second on the same CPU core, giving a speed up of 4 orders of magnitude: ~10'000x (Prasianakis et al. 2020). It is noted that the typical Lattice Boltzmann mass transport solvers achieve calculation speed of 1-5 Million lattice updates per second for mixtures composed of 4 components. A direct coupling with any external geochemical solver will significantly reduce the simulation speed. However, coupling with an ANN, the cost of geochemical calculations reduces to lower levels than the cost of the transport. A proof of concept for simple systems shows already a great potential. Another typical network that has been produced is relevant to calcite-dolomite systems and is shown in Figure 2.3. Results were presented in the international workshop on "How to integrate geochemistry at affordable costs into reactive transport for large-scale systems?" in Dresden, Germany, and published in (Prasianakis 2020). Combination of machine learning techniques with reactive transport simulations will eventually lead to more accurate and reliable field-scale simulations, in reasonable computational times. Moreover, it paves the way to development of more realistic digital twins.

2.3.2 Model developments in Eurad WP-DONUT

Within the EU project Eurad WP4-DONUT Mobility scheme and in the realms of collaboration between PSI and FZ-Julich (IEK-6), Dr. Yuankai Yang visited PSI to investigate the ion diffusion in unsaturated nanoscale porous media via multiscale simulations. During this exchange visit, a generic coupled numerical framework for simulation of ion transport in unsaturated porous media was established as shown in Figure 2.4. As a first step a liquid-gas distribution within 3D microstructures for a given saturation state was simulated using pseudo potential lattice Boltzmann method (Li et al. 2016). Multiphase modelling was performed using Yantra (lead developer: Dr. R. Patel). This simulation served as an input to Poisson-Nernst-Planck based lattice Boltzmann method to simulate species diffusion in the liquid phase. The latter is implemented for GPU architecture by Dr. Y. Yang. From the simulations, the relationships of effective diffusivities with respect to the water content in clays can be assessed. Several preliminary simulations showed that the water film on the clay surface controls the solute diffusion at low water contents even at the micrometer scale, a mechanism, which may be attributed to the surface roughness of the particles. Figure 2.5 shows an example simulation with and without consideration of water films at low saturation. Figure 2.5 also shows that the consideration of water films drastically influences species diffusion.

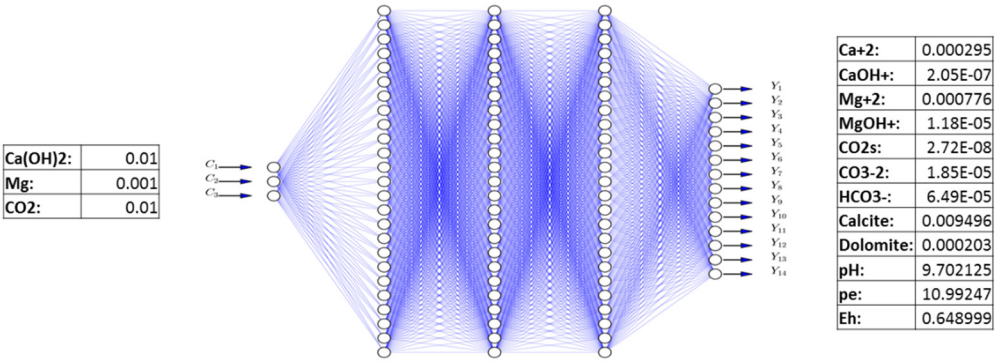

Fig. 2.3: A typical artificial neural network (ANN) for calculating geochemical speciation during high performance computing calculations. A calcite dolomite system is considered with three master species as input and 14 species / precipitates and properties as output.

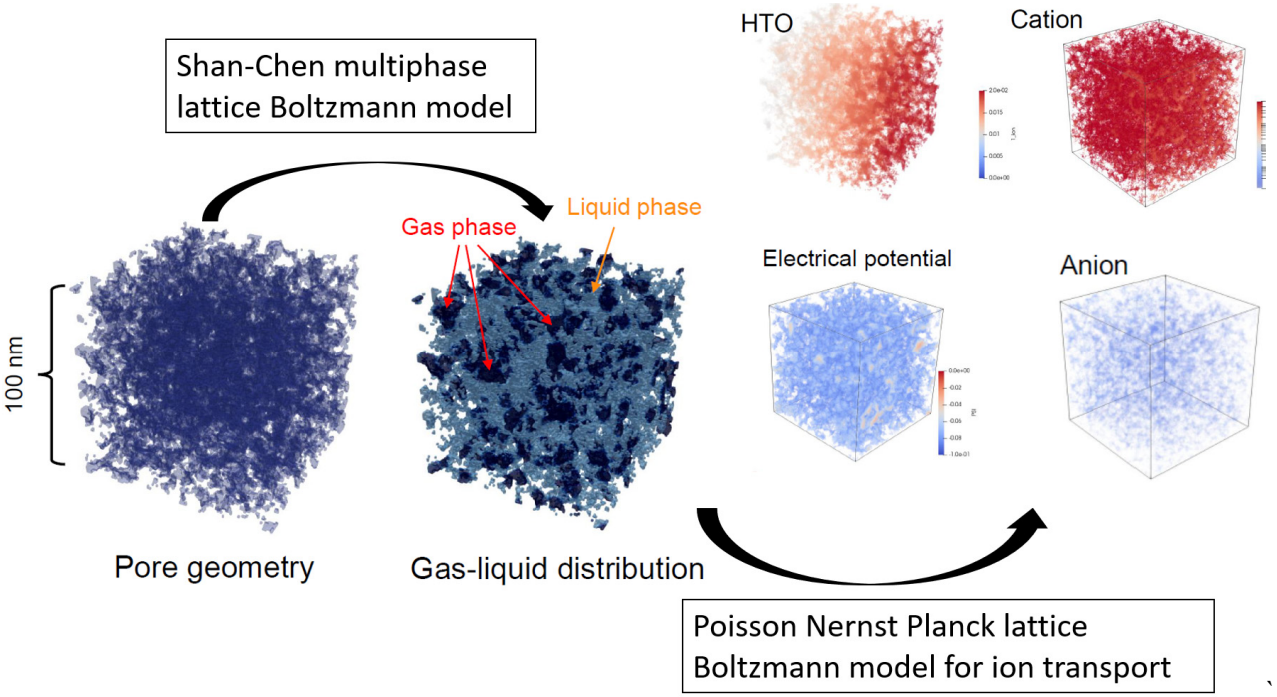

Fig. 2.4: A generic multi-scale / multi-physics framework for ion transport in unsaturated porous media.

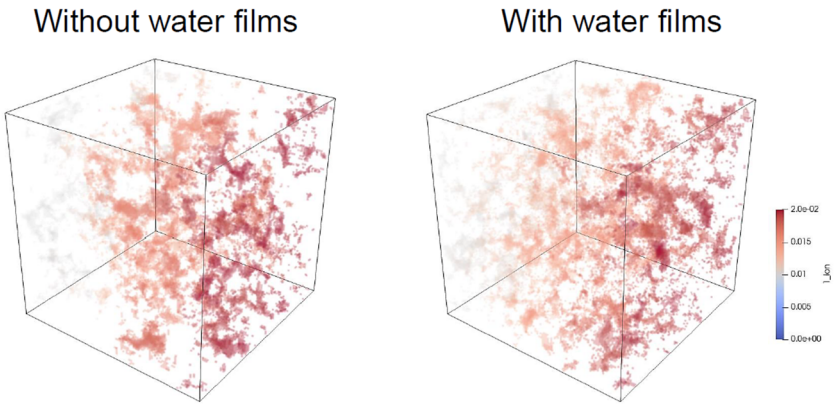

Fig. 2.5: Example distribution of diffusive species at steady state without consideration of water films and with consideration of water films.

2.4 Thermodynamic modelling of cement hydration: NANOCEM CemGEMS project

Chemical thermodynamic modelling has been successfully used to elucidate the impact of factors such as cement composition, hydration, leaching, or temperature on the speciation and the properties of hydrated cementitious systems (Lothenbach & Zajac 2019). Complex geochemical speciation software is needed for determine the relative stability of hydrated phases and aqueous species using the standard thermodynamic data bases. Available general-purpose geochemical codes such as GEM-Selektor (http://gems.web.psi.ch) all have versatile but complex user interfaces that require an installation and upgrades on desktop PC, and demand a considerable learning curve and training time. Hence the need for a dedicated tool for students or non-chemists working on cements, which is easy to use, and requers minimal maintenance efforts. To meet this need, CemGEMS (https://cemgems.app) – an open access easy-to-use web application has been developed to assist cement chemists, students and researchers in easily performing and visualizing thermodynamic models of hydration of cementitious materials.

In its back-end (server), the CemGEMS web app runs the GEMS3K code (Kulik et al. 2013; Wagner et al. 2012) with a pre-configured exported chemical system (18 chemical elements) file, covering temperatures from 0 to 99 °C and pressures from 1 to 101 bar, and based on the standard thermodynamic data from Cemdata'18 (https://www.empa.ch/cemdata) and PSI/Nagra chemical thermodynamic databases.

In the front-end (client) running in any modern web browser, CemGEMS exposes a selection of ready to use template input recipes for 10 different types of cements. Each editable and customizable recipe is composed either of amounts and compositions of cement clinker minerals or with a bulk chemical composition of cement based on XRF analyses. The recipes can be combined with any or some of template processes (hydration, blending, leaching, carbonation, salt attack, etc.). The simulation results can be presented in several types of plots (with a simple switching between them), or tabulated and exported into .csv files for use in electronic spreadsheets or other programs.

Fig. 2.6 shows the welcome page of CemGEMS that also bullet-points its main functionalities. At any time, the user can open the online Tutorial and Information page (https://cemgems.org) explaining the web app functionality, which also contains a gallery of screen images of various tables, bar charts and plots that can be produced with CemGEMS.

In May 2020, an extension of CemGEMS Nanocem internal project has been approved, which aimed to better meet the needs of users and to foster their collaboration. This includes: (i) Calculations of heat effects on cement hydration in isothermal and adiabatic cornerstone cases (already in testing); this is possible using the enthalpies and heat capacities of all clinker and hydrated phases available in Cemdata'18 database. (ii) Another process type for simulating cement hydration vs time (developed in collaboration with Frank Winnefeld, Empa), using the so-called 4PL (four-parameter logistic) equations for clinker phases and SCMs, with parameters regressed from time-dependent XRD phase characterization data.

CemGEMS web app can be used to model cement leaching, degradation and salt attacks, the processes relevant for the industrial engineering, (radioactive) waste management studies, and cement research. Particularly useful for practical applications are template recipes and process definitions, available (as JSON documents) for selection in any user session. Each of provided "hydration-ready" template recipes can save the user many hours of work because it already contains a lot of chemical and mineralogical data, collected and recommended by world-renowned experts in cement chemistry and thermodynamics. Other user oriented functionalities include:

- Easy adjustment of temperature, pressure, water/binder mass ratio, reaction extent, mineralogical and/or chemical composition, and other inputs using expandable tree-like tables and built-in editor of JSON documents.
- Computation of partial-equilibrium hydrated phase assemblage and porewater speciation set by reaction extents.
- Comparison of initial/final volumes, masses, densities, etc. for equilibrated and residual parts separately or as totals.
- Possibility to follow the impact of regular change of some inputs onto composition and properties of hydrated cement in process simulations, plots and tables of results.
- Storage and retrieval of recipes, processes and plots in local and/or remote user profile, synchronized between different devices.

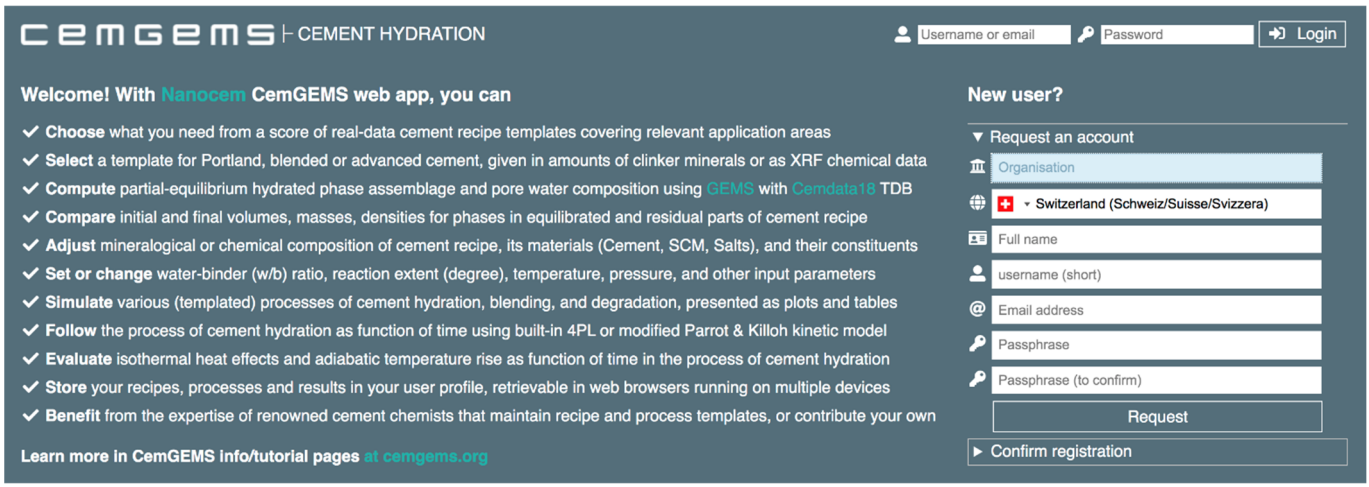

Fig. 2.6: Welcome page of CemGEMS web app (https://cemgems.app), with a list of main functionalities and a user registration form (as of November 2020). Appearance on desktop, Chrome web browser.

- Front-end operating in any modern web browser on a range of devices (from a mobile pad/tab to a desktop PC) without a need for installation or update; entering or exploring data in recipes also possible offline.
- Simple, intuitive user interface consisting of Input, Output and Process Plot views, with tree-like tables optimal for defining the cement initial composition and hydration, and for exploring the detailed results.

CemGEMS can be viewed as a "proof-of-concept" for further development of web-based tools dedicated for specific applications of chemical thermodynamic modelling by GEM method. In this context, CemGEMS tree-like table widgets, hierarchical recipes consisting of materials consisting of constituents consisting of formulae, and simple intuitive workflows identified from users' feedback, are of particular importance. Current work is focused on using web based client-server paradigm for moving GEM calculations from the server side into the client web browser, and using WebRTC for a decentralized peer-to-peer users communication in order to avoid keeping the user data (recipes, processes) in a central server database.

Funded by the Nanocem consortium (https://nanocem.org) since summer 2018, the CemGEMS web app is being developed in Switzerland at LES PSI (GEMSW code, templates, info/tutorial site) and at Congineer GmbH (DevOps, front-end and back-end), in collaboration with scientists from Empa (Barbara Lothenbach, Frank Winnefeld), EPFL (Fabien Georget), Lafarge-Holcim (Bruno Huet) and Heidelberg-Cement Technology Center (Maciej Zajac).

2.5 Diversification projects (Interdisciplinary Application of Methods and Models)

2.5.1 Numerical prediction of boiling crisis considering surface characteristics

In the realms of a collaborative project with the Laboratory for Scientific Computing and Modelling at PSI (LSM-PSI) and under the umbrella of the Swissnuclear funding agency through the project "*Numerical prediction of boiling crisis considering surface characteristics*", the fundamental understanding of boiling processes from atomistic to reactor scale is pursued. The goal of the proposed project is to predict the boiling crisis, *i.e.* Critical Heat Flux (CHF), based on purely numerical simulation, in which surface condition/roughness is fully taken into account. LES is conducting the model development and simulations at the micrometer and the atomistic scale, aiming at providing bottom-up parametrization to the macroscopic boiling code, developed at PSI, PSI Boil (https://www.psi.ch/en/lsm/psi-boil).

Within the ongoing Swissnuclear project the hybrid thermal LB model was further developed to account for conjugate heat transfer near rough solid. This model would allow direct simulation of the nucleate pool boiling and to provide key relationships regarding nucleation site density and different hydrodynamic parameters, which would serve as input for PSI-Boil. As a first step a thermal lattice Boltzmann model for conjugate heat transfer was developed. A case of conjugate natural convection with thermal conduction in a thick vertical wall was chosen for the validation. The simulation setup with relevant input parameters and boundary conditions is shown in Figure 2.7. The steady state plots of streamlines and isotherms for dimensionless temperature is shown in Figure 2.8. The Nusselt number computed at the surface of thick wall is compared to simulation reported by Pan et al. (2018) using second order finite difference scheme. The difference between LB model and the reference simulations was found to be 2.05% for a 270×225 computational LB domain.

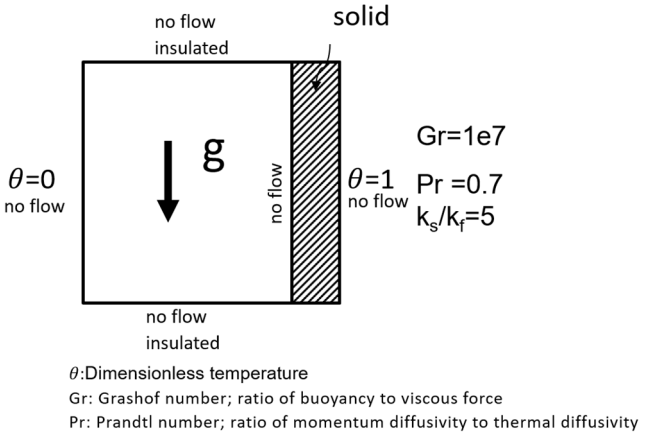

Fig. 2.7: Simulation setup for conjugate natural convection with thermal conduction in a thick vertical wall.

Initial coupling between developed LB model for heat transport and Shan-Chen multiphase model has been achieved. To demonstrate the coupling a qualitative benchmark for droplet evaporation was implemented. This benchmark is commonly referred to as D^2 test as the square of droplet diameter varies linearly with time. Figure 2.9 shows initial conditions and simulation results for different initial size of droplet. Figure 2.9 demonstrates that the model is able to successfully reproduce D^2 test and also the effect of different initial droplet size on rate of evaporation.

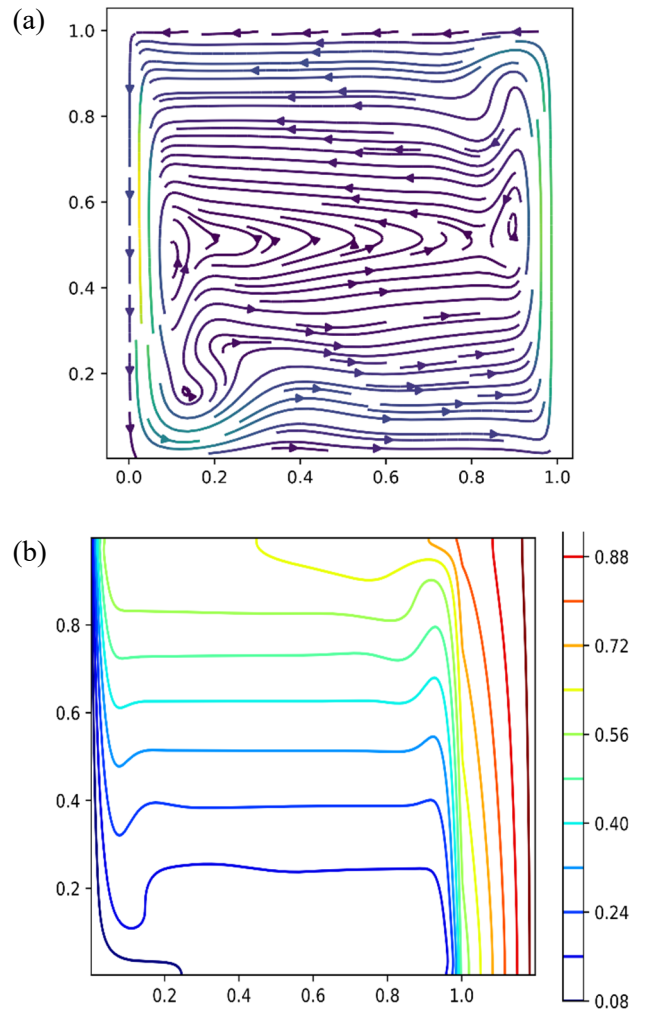

Fig. 2.8: conjugate natural convection with thermal conduction in a thick vertical wall (a) streamlines at steady state and (b) isotherms for normalized temperature.

2.5.2 Research project with GlaxoSmithKline Vaccines

In 2020, an industrial project with the pharmaceutical company GlaxoSmithKline Vaccines, Belgium (GSK) has been continued (PI: N. Prasianakis). GSK is a science-led global healthcare company focused in the research, development and manufacturing of innovative pharmaceutical medicines, vaccines and consumer healthcare products. Advancements in specific areas within the aforementioned domains can be based on advanced theoretical and numerical modelling. For this project, the state-of-the-art multiscale models and methods developed at LES are fully utilized.

2.6 References

Bradbury M.H., Berner U., Curti E., Hummel W., Kosakowski G., Thoenen T. (2014)
The Long Term Geochemical Evolution of the Nearfield of the HLW Repository. Nagra Technical Report NTB 12-01.

Curti E., Crovisier J.-L., Karpoff A.-M., Morvan G. (2006)
Long-term corrosion of two nuclear waste reference glasses (MW and SON68): a kinetic and mineral alteration study. Appl. Geochem., 21, 1152–1168.

Hummel W., Curti E. (2020)
The PSI Chemical Thermodynamic Database 2020: Data Selection for Phosphorus and Application to HLW near-field pore water modelling. Technical Note TM-44-20-06, Paul Scherrer Institut.

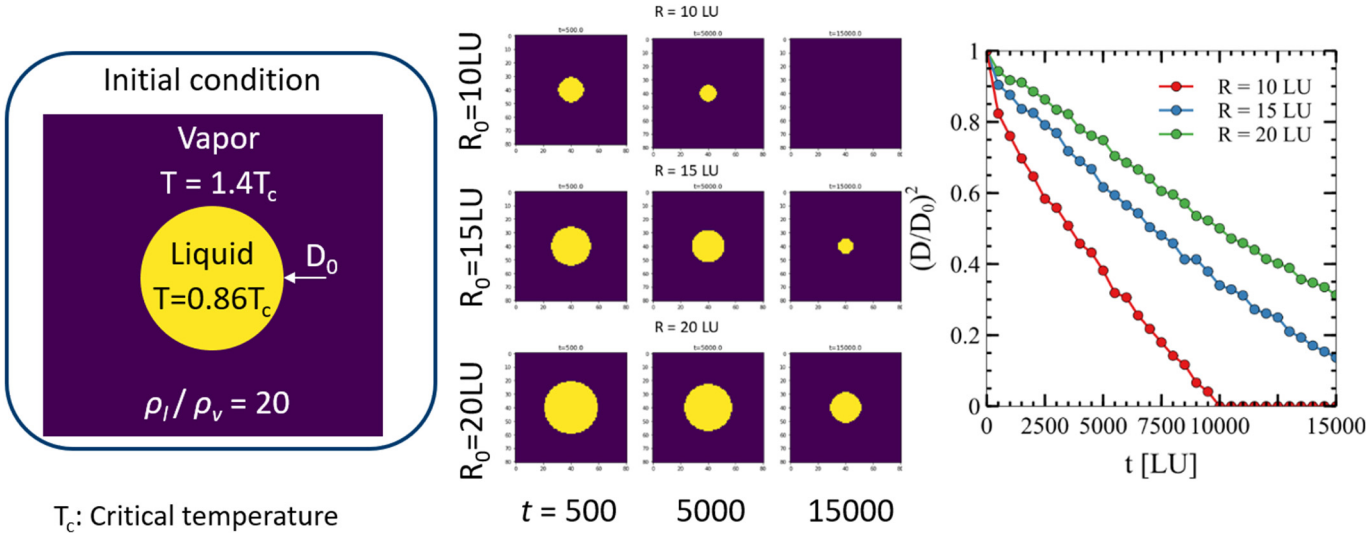

Fig. 2.9: D^2 test for droplet evaporation under isothermal conditions. Density ratio between vapour and solid phase is 20. Liquid and gas phase are in yellow and dark violet colours, respectively.

Kosakowski G., Berner U. (2011)
Influence of a concrete liner on the evolution of the near field of a HLW repository. Technical Note AN-44-10-09-Rev1, Paul Scherrer Institut.

Li Q., Luo K.H., Kang Q.J., He Y.L., Chen Q., Liu Q. (2016)
Lattice Boltzmann methods for multiphase flow and phase-change heat transfer. Progress in Energy and Combustion Science, 52, 62-105.

Pan Xiaomin, Lee Changhoon, Choi Jung-Il. (2018)
Efficient monolithic projection method for time-dependent conjugate heat transfer problems. Journal of Computational Physics 369: 191-208.

3 DEVELOPMENT OF MECHANISTIC SORPTION MODELS AND EXPERIMENTAL VALIDATION

Baeyens B., Dähn R., Glaus M.A., Kulik D., Marques Fernandes M., Miron D., Van Loon L.R., Churakov S.V., Schaible A., Lang C., Cruz P. (postdoc), Qian Y. (PhD student)

3.1 Introduction

Sorption is one of the most important repository relevant processes contributing to the retention of radionuclide transport in a repository near-field. The aim of this project is to improve the mechanistic understanding of the uptake processes of (radio-) contaminants onto 2:1 clay minerals, argillaceous rocks and soils. This knowledge is used for the development of sorption databases (SDB) for the future performance assessments, *i.e.* the bottom-up approach will be applied to calculate K_d values in argillaceous rock systems for a range of geochemical *in situ* conditions. The main topics addressed in 2020 are briefly summarised below.

In the framework of the deep drilling programme carried out by Nagra sorption investigations on bore core samples have been carried out. The bottom-up approach was tested on sorption isotherms measurements for Cs^{I}, Ni^{II}, Eu^{III}, Th^{IV} and U^{VI} on an Opalinus Clay (OPA) sample from the Bülach-1 borehole.

In collaboration with the diffusion group on the transferability of dispersed to compacted systems saturation and extractions experiments were carried out on rock sample from the Lausen borehole, to assess the consistency between equilibrium solution composition and the cation occupancy of argillaceous rocks. The aim is to test the applicability of the thermodynamic calculation approach used to derive the composition of porewaters.

GEMSFITS was applied to a large number of Ni adsorption data (edges and isotherms) on purified and homo-ionic Na-IdP (illite du Puy) to perform an uncertainty analysis of the derived surface complexation constants and selectivity coefficients of the 2SPNE SC/CE sorption model.

In the framework of the EU project FUTURE (Eurad) activities have been started during this year. In the sub-task "*Reversibility of sorption*" wet chemistry studies of Zn reversibility on illite were carried out and the first results are presented. The foreseen spectroscopic studies could not be carried out due to the Covid-19 restrictions in 2020. In task "*Redox reactivity of radionuclides on mineral surfaces*" a PhD student has carried out the purification and chemical reduction (citrate-bicarbonate–dithionite) of different Fe^{III} containing clay minerals, in order to obtain clay minerals with different Fe^{II}/Fe^{III} ratios.

The further aim is to study on these $Fe^{II/III}$ bearing clay minerals the influence of coupled adsorption and surface induced electron transfer reactions on the retention of redox-sensitive nuclides.

The sorption studies (wet chemical and spectroscopy) of Zn on illite and argillaceous rocks have been finalized and a paper is in preparation.

The results of the study on the competitive sorption behaviour on a large number of bi-ionic and multi-ionic radionuclides on illite and montmorillonite were evaluated and published in a report (NTB-19-05).

The SNSF-PhD project of Silvan Wick entitled "*Sorption of thallium to illite and birnessite and its impact on the solubility of thallium in soils*" in collaboration with Eawag (Molecular Environmental Geochemistry Group) was completed and the paper on thallium speciation in soils has been published. The PhD defence took place on 28 January 2020.

The study on the iron adsorption on clays based on *ab initio* simulations and X-ray absorption spectroscopy, conducted within SNSF-PhD project of Annamária Kéri has been finalised and published.

A project (PhD and postdoc) entitled "*Molecular scale understanding of competitive cation adsorption on swelling clay minerals*" was granted by SNSF in spring and is expected to start in the course of 2021.

3.2 Sorption studies on an Opalinus Clay sample from the Bülach-1 borehole

Sorption experiments in a synthetic pore water (SPW) were carried out on sample BUL1-1-995.09-DI, a clay-rich sub-unit, which was taken at a depth of -995 m, which is at the lower boundary of the Opalinus Clay formation (-892 m to ~ -996 m) in this region (Nördlich Lägern). The rock sample was crushed inside a glove box at a particle size ≤ 1 mm and conditioned with the SPW. The pore water composition and rock mineralogy of the sample is given in Tables 3.1 and 3.2.

Sorption isotherms for the nuclides Cs^{I}, Ni^{II}, Eu^{III}, Th^{IV} and U^{VI} have been carried out from trace concentrations up to concentrations where the stable element concentrations are still above the calculated solubility limit.

Tab. 3.1: Composition of synthetic pore water for the Bülach-1 drill cores (Mäder, pers. comm.).

pH	7.6
I.S. (M)	0.4
pCO_2 (bar)	$10^{-3.4}$
	Concentration (M)
Na	0.325
K	0.0019
Mg	0.0176
Ca	0.0383
Sr	0.0003
Cl	0.402
SO_4	0.0275
TIC	0.00041

Tab. 3.2: Mineralogical composition of BUL1-1-995.09-DI rock sample (Mazurek, pers. comm.).

Mineral	**Weight %**
Illite end-member	29
Smectite end-member	3.4
Kaolinite end-member	23
Chlorite end-member	7
Quartz	16
K-Feldspar	5
Plagioclase	3
Calcite	9
Siderite	2

The experimental results are shown in Fig. 3.1. The isotherm data have been tested using the bottom-up approach by considering for Cs the illite end-member and for the remaining nuclides the illite + smectite end-member weight % as given in Table 3.2. The model parameters given in Bradbury and Baeyens (2017) have been used for the blind predictions. In the calculations the full aqueous speciation was included in the model and only the cation exchange and/or surface complexation reactions (*i.e.* only the free and hydrolysed metal complexes form surface complexes) as defined in the 2SPNE SC/CE model were used.

The general impression of the blind modelling predictions can be regarded as good as indicated by the solid black lines in Fig. 3.1. The contributions of the dominant surface species on the different sites are also shown in the figures where appropriate. In the case of Cs (Fig. 3.1a) a slight over estimation of sorption is seen on the type II sites (2TS). Lowering the capacity of T2S by a factor of 2 results in a very good fit as shown by the dotted line in Fig. 3.1a.

The predictions for Ni^{II}, Eu^{III} and U^{VI} are within the error bars of the experimental data points. The aqueous speciation for Ni and Eu do not play a significant role since only ~30 to 50 % of the Ni/Eu is complexed with inorganic ligands reducing the sorption by ~30 to 50 %. On the other hand, for U^{VI} the aqueous complexation with inorganic ligands (*e.g.* CO_3^{2-}) or the formation of aqueous ternary complexes such as Ca-U-CO_3 play an important role in reducing the sorption by three orders of magnitude. In view of these large reduction factors the blind predictions for U^{VI} can be regarded as very satisfactory.

The data of Th are very scattered and are higher compared to the measurements obtained on pure illite (Bradbury and Baeyens 2009). The reason for these high and scattered R_d values is due that the radio-assay measurements of ^{228}Th in the supernatants are close to the background activities.

From these measurements and modelling it can be safely concluded that the so-called bottom-up approach produce highly reliable results and can be adopted for the development of SDB for safety assessment purposes.

3.3 Cation occupancy of rock samples from the Lausen drill borehole

The composition of clay rock pore water is mainly controlled by the solubilities of the mineral phases and exchange or complexation processes taking place at the mineral surfaces. Because of the inherent difficulties related to the extraction of pore water from clay rocks in its pristine equilibrium composition, the composition of synthetic clay pore waters is defined based on thermodynamic calculations. The result of such modelling cannot, however, be readily verified. Experiments were therefore carried out, in which the consistency between solution composition and the cation occupancies of the major alkaline and earth-alkaline cations of Opalinus Clay was assessed in order to test the applicability of the underlying thermodynamic datasets. Cylindrical clay rock samples with thicknesses of ~1 cm from the Lausen drilling borehole site were re-saturated with two SPW exhibiting different concentrations of alkali and earth-alkaline elements. The re-saturation was carried out in two steps, the first step comprising rather small solution reservoir volumes in order to be able to observe measurable concentration changes in the solutions during re-saturation. In the second step, larger solution volumes were applied in order to provide a large mass capacity in the solution compared to the capacity of the cation exchange sites. Table 3.3 shows the composition of the two different SPWs applied in the experiments and the expected cation composition at the planar clay surfaces (N_B denoting fractional cation occupancies).

The concentrations of the most important constituents of the solution phases were monitored periodically by ion chromatography during the two re-saturation steps.

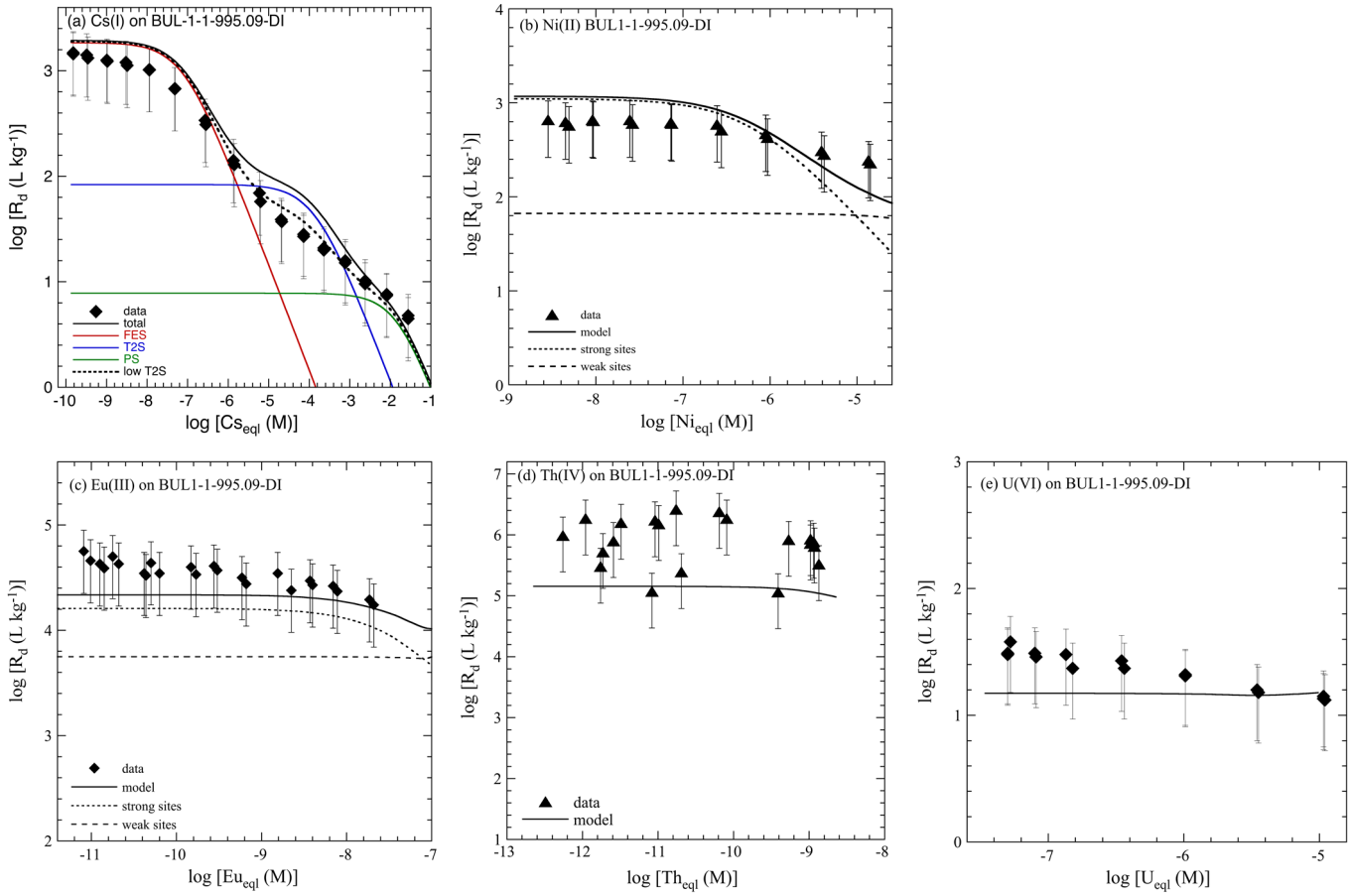

Fig. 3.1: Sorption isotherms of (a) Cs^{I}, (b) Ni^{II}, (c) Eu^{III}, (d) Th^{IV} and (e) U^{VI} on Opalinus Clay from the Bülach1 borehole. Experimental and blind predictions.

Tab. 3.3: Composition of the synthetic pore waters used for re-saturation of the clay rock samples and expected cation occupancies of the planar surface sites.

Solution characteristics	**SPW-A**	**SPW-B**
log P_{CO2} (bar)	-3.50	-3.50
pH	8.16	8.2
I.S. (M)	0.094	0.02
Na (M)	8.00×10^{-2}	1.00×10^{-2}
K (M)	2.00×10^{-3}	1.00×10^{-3}
Mg (M)	1.53×10^{-3}	8.74×10^{-4}
Ca (M)	2.03×10^{-3}	1.16×10^{-3}
Sr (M)	5.00×10^{-5}	5.00×10^{-5}
Cl (M)	8.00×10^{-2}	1.00×10^{-2}
SO_4 (M)	4.00×10^{-3}	2.00×10^{-3}
$C_{inorg.}$ (M)	9.51×10^{-4}	9.00×10^{-4}
F (M)	2.55×10^{-4}	2.43×10^{-4}
Si (M)	1.85×10^{-4}	1.85×10^{-4}
Surface characteristics		
Na: meq/kg (N_B)	31.0 (0.53)	6.8 (0.12)
K: meq/kg (N_B)	3.9 (0.07)	3.4 (0.06)
Mg: meq/kg (N_B)	8.7 (0.15)	17.8 (0.31)
Ca: meq/kg (N_B)	14.1 (0.24)	28.8 (0.50)
Sr: meq/kg (N_B)	0.3 (0.01)	1.3 (0.02)
SUM: meq/kg (N_B)	**58 (1.0)**	**58 (1.0)**

As it is not *a priori* clear to what extent a homogeneous distribution of the cations in the clay samples can be achieved during re-saturation, the solution composition in the internal pore space and the cation distribution at the clay surfaces were tentatively assessed by coupled transport modelling using the EDL sorption/diffusion model. Such simulations are inherently based on a number of model assumptions that cannot be verified unambiguously. The evolution of the species concentrations in the external solution reservoirs were used to define these model assumptions as good as possible. Fig. 3.2 (left hand side) shows a simulation of the first re-saturation phase with SPW-A. This phase is dominated by out-flux of Mg^{2+}, Ca^{2+} and SO_4^{2-} from the clay to the solution. The seeming discrepancy between experimental and model data for Sr^{2+} is explained by the large analytical uncertainty because Sr^{2+} concentrations were close to the detection limit. Note that the thermodynamic model does not take into account any (possible) dissolution or precipitation reactions. Independent of the intrinsic model assumptions it can be concluded that the clay surface was occupied to a significant extent, with alkaline earth cations in the initial state; sulphate is most probably related to oxidation of sulphide containing minerals in view of the previous storage of the samples under oxic

conditions. The model calculations also revealed that a perfect equilibrium state regarding cation distribution in the clay samples was not fully achieved during the first saturation step (cf. Fig. 3.2, right hand side). A similar data analysis after the second saturation step (not shown) indicates that the resulting fractional occupancy was significantly closer to the target values, but yet exhibiting some discrepancies.

After the two re-saturation steps, the rock samples were crushed and the cations were extracted using $CsNO_3$. Table 3.4 shows the measured cation occupancies after correction for the dissolution of soluble salts (*e.g.* NaCl) and minerals (*e.g.* calcite). The correction methodology is described in detail by Hadi et al. (2017). The measured and calculated pore water compositions are in acceptable agreement in the view of the fact that (i) the final values are strongly affected by intrinsic uncertainties related to the correction terms, and that the samples were not in perfect equilibrium with the solution phases even after the two re-saturation steps. The latter observation is of particular interest since it is broadly assumed that a re-saturation phase of 1 month is generally sufficient to obtain a homogeneous equilibrium pore water distribution in clay samples with typical thickness of ~1 cm.

3.4 Application of GEMSFITS on the sorption model of Ni on illite

A summary of experimental sorption data of Ni on illite (Na-IdP) is presented in Fig. 3.3. Thirteen independent "in house" experimental data sets are available and comprises sorption edges in 0.01 M, 0.1 M and 0.5 M $NaClO_4$ and isotherms in 0.1 M $NaClO_4$ at pH 6.1, 7.0-7.2 and 7.8. The blue lines in the sub figures are the fits by eye to the experimental data with the hydrolysis constants given in Table 3.5 and surface complexation and cation exchange constants on the strong, weak and planar sites of illite given in Table 3.6. Note that in Fig. 3.3a the Ni sorption data below pH 6 are lower that the fit calculations. This is due to competitive cation exchange reactions of H^+, Ca^{2+} and Al^{3+} with Na^+ for

Tab. 3.4: Comparison of measured and predicted cation occupancies of the Lausen clay rock samples after the two re-saturation steps.

Cation	Fractional cation occupancies (NB)			
	SPW-A		SPW-B	
	measured	predicted	measured	predicted
Na	0.43	0.53	0.11	0.12
K	0.11	0.07	0.14	0.06
Mg	0.25	0.15	0.35	0.31
Ca	0.19	0.24	0.38	0.50
Sr	0.02	0.01	0.02	0.02

Tab. 3.5: Hydrolysis reactions and constants for Ni taken from Baes and Mesmer (1976).

Hydrolysis reaction	**log ^{OH}K**
$Ni^{2+} + H_2O \Leftrightarrow NiOH^+ + H^+$	-9.86 ± 0.03
$Ni^{2+} + 2H_2O \Leftrightarrow Ni(OH)_2^0 + 2H^+$	-19.0 ± 1
$Ni^{2+} + 3H_2O \Leftrightarrow Ni(OH)_3^- + 3H^+$	-30 ± 0.5

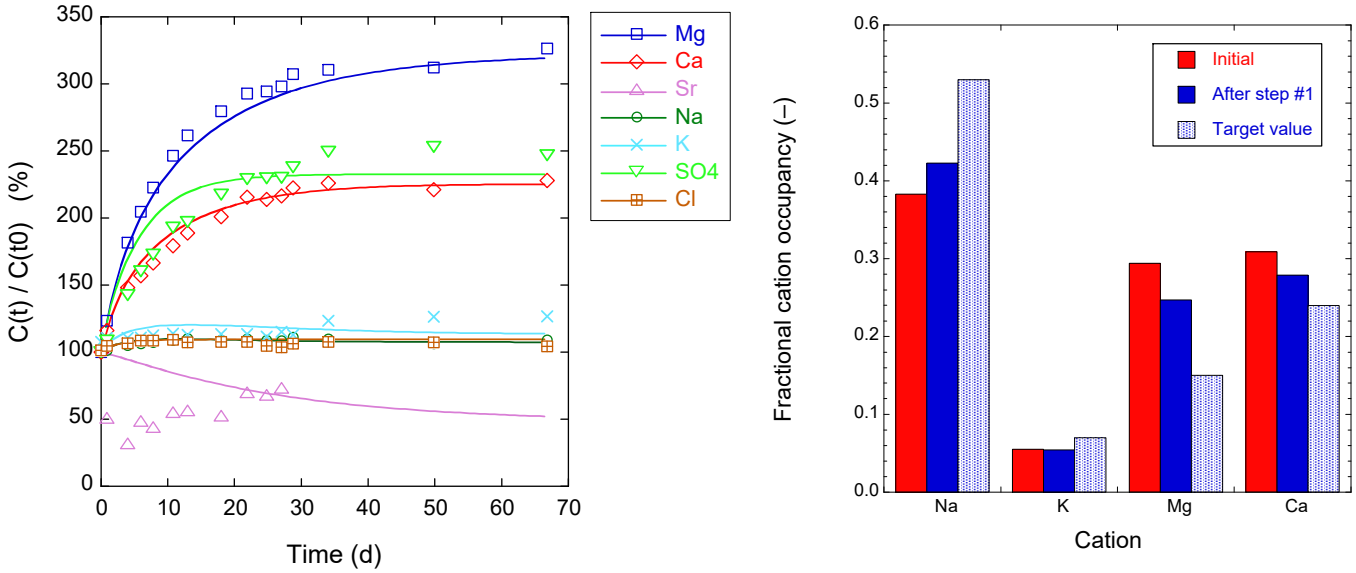

Fig. 3.2: Measured and modelled evolution of the solution composition relative to the initial composition of the SPW's in the external solution during re-saturation of a Lausen clay rock sample with SPW-A (plot left hand side) and modelled cation occupancy at the clay surface (plot right hand side). The latter plot also shows the calculated initial cation occupancy and the target values which would result from a homogeneous equilibration of the clay with an infinitely large solution volume.

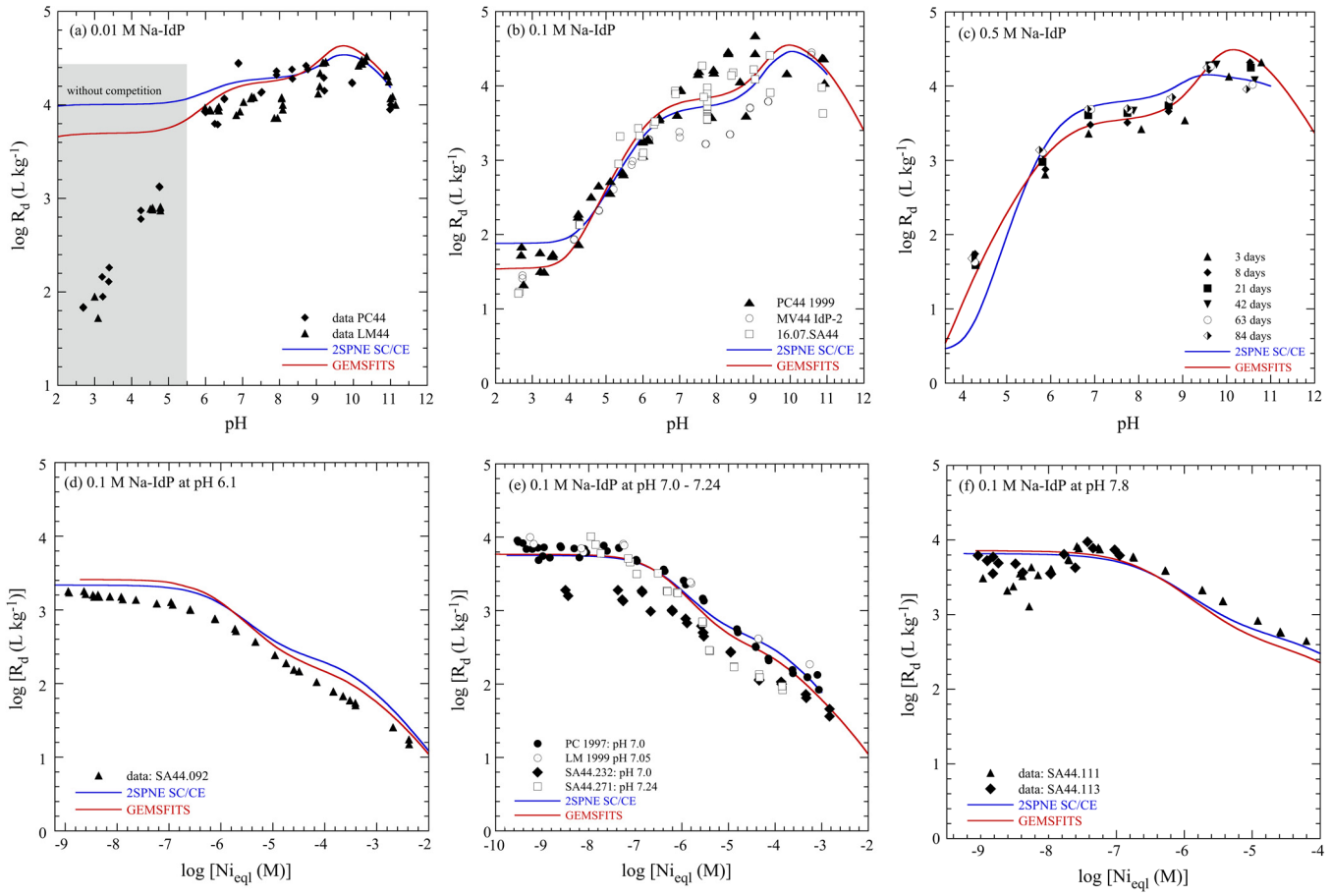

Fig. 3.3: Ni sorption data on Na-IdP. Experimental and model fitting by eye (blue curves) and with GEMSFITS (red curves).

the planar sites which become important when the Na background concentration is very low (0.01 M) (see also Bradbury & Baeyens 2005). These competitive cation exchange reactions have not been included in this fitting exercise.

The fits by eye do not allow a rigorous uncertainty analysis of the constants obtained from the fitting procedure. In order to estimate the uncertainty on the model parameters, the GEMSFITS code (Miron et al. 2015) was applied along with the ClaySor GEMS implementation (Kulik et al. 2018; NAB 18-27) of the 2SPNE-SCCE sorption model (Bradbury & Baeyens 1997; 2009a,b). GEMSFITS is a tool that can simultaneously refine multiple parameters such as thermodynamic constants against many various experimental data sets. GEMSFITS uses internally the GEMS3K code (Kulik et al. 2013; Wagner et al. 2012) to calculate equilibrium speciation for each experimental data point. The adjusted values of standard Gibbs energy of formation (for surface species) can be easily converted to equilibrium constants (of surface complexation reactions).

In the current context, GEMSFITS can refine the equilibrium constants for surface complexation and ion exchange to obtain best agreement between measured and calculated values for all used datasets. For evaluating the parameter uncertainty intervals of adjusted parameters, GEMSFITS uses the Monte Carlo sampling method. In brief, the available set of experimental data is sampled into 300 to 1000 pseudo-datasets by random variation of each measured property within its (analytical) error and assumed distribution, such that all pseudo-datasets are statistically equivalent. Then the parameter optimization is repeated automatically for all artificial pseudo-datasets. The retrieved best-fit parameters for all runs are collected into a table, where the confidence intervals of the adjusted parameters comprise a good approximation of their intrinsic uncertainty (Motulsky and Christopoulos 2004).

The intrinsic parameter uncertainties for Ni surface complexation on illite (Table 3.6) were estimated from 1000 synthetic datasets. These were generated by randomly changing the values of the experimental points (log R_d) within the scatter of the data, using a normal distribution with the variance equal to the difference between the measured and calculated value. This can be imagined as if the experiments would be repeated 1000 times under the same conditions, obtaining the best fit parameters each time, and then using parameter values to evaluate their averages and confidence intervals.

Tab. 3.6: Surface complexation and cation exchange parameters.

	Fit by eye	GEMSFITS
Surface complexation on strong sites	log ^{SC}K	
$\equiv^{S}SOH + Ni^{2+} \Leftrightarrow \equiv^{S}SONi^{+} + H^{+}$	0.6	0.76 ± 0.05
$\equiv^{S}SOH + Ni^{2+} + H_2O \Leftrightarrow \equiv^{S}SONiOH^{0} + 2H^{+}$	-8.4	-8.21 ± 0.24
$\equiv^{S}SOH + Ni^{2+} + 2H_2O \Leftrightarrow \equiv^{S}SONi(OH)_2^{-} + 3H^{+}$	-18.0	-17.96 ± 0.13
Surface complexation on weak sites		
$\equiv^{W1}SOH + Ni^{2+} \Leftrightarrow \equiv^{W1}SONi^{+} + H^{+}$	-1.8	-1.84 ± 0.14
Cation exchange on planar sites	log K_c	
$2Na\text{-}IdP + Ni^{2+} \Leftrightarrow Ni\text{-}IdP + 2\ Na^{+}$	1.04	0.44 ± 0.09

Thus, obtained uncertainties relate to random errors in the measured data and do not include any systematic error. The uncertainty interval does not necessarily cover all the variation and scatter in the experimental data. This is because the final parameter values have a certain degree of correlation with the other parameters; they are constrained by the species in the chemical system, and by the experimental points from many datasets. Therefore, having the model crossing some extreme experimental data points (outliers) is highly unlikely.

Future work is planned to refine the surface complexation reaction constants of other elements, to provide 95% confidence interval parameter uncertainties, and to make them consistent with the updated version of the PSI/Nagra database.

3.5 Contribution to the Eurad project FUTURE

3.5.1 Reversibility of sorption

The sorption of radionuclides on clay minerals in engineered and geological barrier systems is a key safety function in deep geological disposal of radioactive waste. The current sorption model used in the safety assessment assumes reversibility of sorption. One of the open questions is related to the adsorption reversibility and the nature of mechanism that controlling the retention in the long-term. Among others LES conducts wet chemical and spectroscopic investigations on the reversibility of Ni and Zn on 2:1 clay minerals. The first results from adsorption/ desorption experiments of Zn on illite (IdP) have become available in 2020.

An experimental protocol was applied to investigate reversibility of Zn on Na-IdP. To this end an adsorption experiment was set up in which Zn was equilibrated with Na-IdP in 0.1 M NaCl background electrolyte at pH 7 for 14 days at a high S/L ratio of 14 g/l. The experimentally measured adsorption data are shown in Fig. 3.4 as black symbols at log Zn_{eql} = -3.7 M and log Zn_{eql} = -4.2 M. Figs. 3.4a and 3.4b present the results as log adsorbed Zn *vs* log Zn_{eql} and log R_d *vs* log Zn_{eql}, respectively.

The 2SPNE SC/CE model was applied to simulate the adsorption data. At these Zn_{eql} loading, Zn is preferentially adsorbing on the weak sites as indicated by the modelling curves in Fig. 3.4. A log $^{W1}K_{SC}$ of -2.0 for the weak sites was adapted to these specific measurements. After the 14 days interaction time, a part of the Zn/Na-IdP suspension at high S/L was transfer to another container and diluted by a factor of 10 in 0.1 M NaCl at pH 7. Model calculations illustrate how the adsorbed Zn should move along the isotherm as shown by the blue symbols in Fig. 3.4. Upon dilution the Zn_{eql} concentration is expected to decrease initially by a factor of 10, but because of desorption its concentration is expected to increase steadily until an equilibrium is obtained. In the case of fully reversible Zn adsorption, the calculated blue symbols in Fig. 3.4 shows the expected Zn_{ads} (Fig. 3.4a) or Zn R_d values (Fig. 3.4b).

The data measured in the desorption experiments, however, show a totally different picture compared to the behaviour expected for a reversible equilibrium thermodynamic process. Decreasing the S/L ratio did not trigger Zn desorption as shown by the red symbols in Fig. 3.4. These measurements were obtained after 7 days reaction time. Even after 92 days reaction time no Zn desorption could be measured. The results of these wet chemistry measurements indicate clearly that Zn adsorption on the weak sites on Na-IdP is non-reversible.

Identical experiments with stable Zn were set up in parallel and samples have been prepared for the planned EXAFS investigations. However, the investigations of the bulk-XAS samples were severely hampered by the current COVID-19 situation. Several beamtime proposals to different synchrotron have been submitted in spring, but unfortunately, due to the given situation the operation of synchrotrons for non-COVID-19 research has been stopped worldwide. The EXAFS results are thus pending.

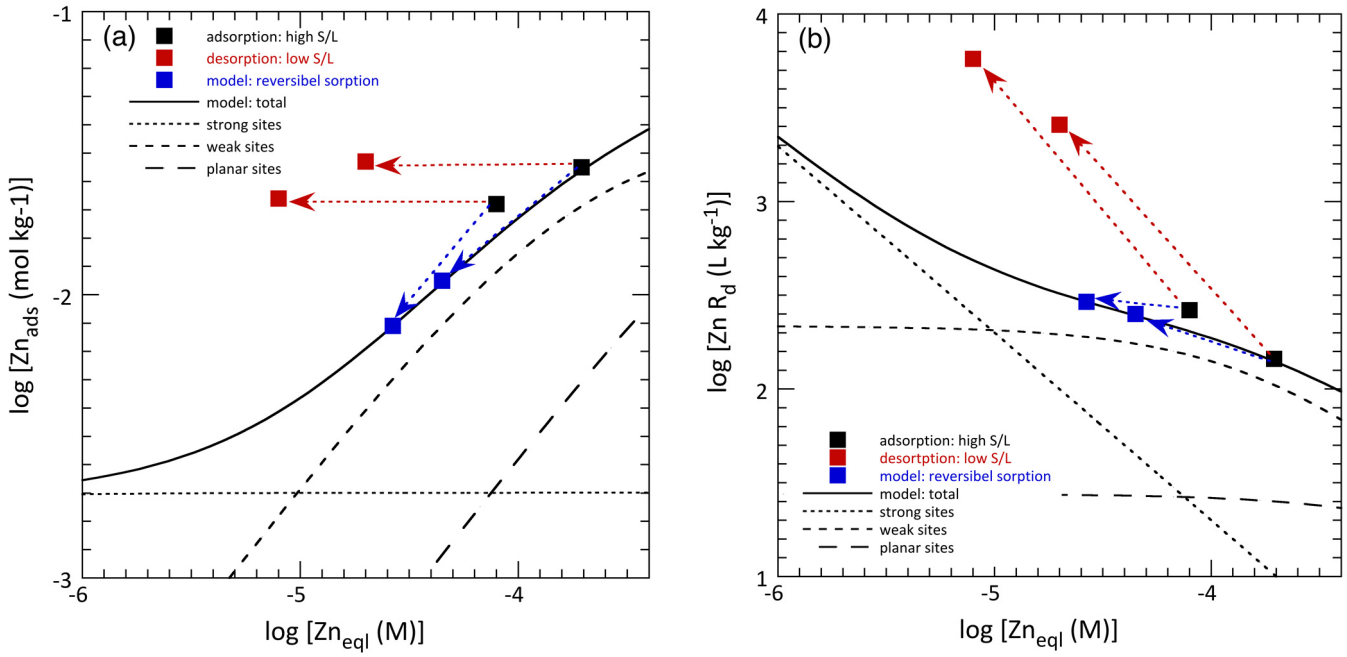

Fig. 3.4: Zn sorption and sorption reversibility on Na-IdP. Experimental and modelling (see text for details).

3.5.2 Redox reactivity of radionuclides on mineral surfaces

The PhD project of Yanting Qian entitled "*Coupled adsorption and electron transfer interface reactions governing the retention of redox-sensitive Se and Tc on $Fe^{II/III}$ bearing clay minerals*" started in November 2019. The project focuses on interface redox reactions between radionuclides Se/Tc and Fe of the clay. The aim of the project is to quantify and characterize the coupled sorption and reduction mechanism (*i.e.*, electron transfer, reactivity of Fe^{II} & influence of amount Fe^{II}, $Fe^{II/III}$ ratio, crystallographic location) of these redox sensitive radionuclides by iron bearing clay minerals.

The PhD student started with literature survey to achieve a comprehensive understanding of experimental challenges and methodological solutions. The experimental part started with purification and conditioning into the homoionic Na form of three types of clay minerals, Wyoming montmorillonite (SWy-2), Nontronite (NAu-2) and Texas montmorillonite (STx-1), which contain different structural iron contents. Afterwards, all three clays were reduced by a mixture of sodium citrate, sodium bicarbonate, and sodium dithionite following the citrate-bicarbonate-dithionite (CDB) method proposed by Stucki et al. (1984). The reduction process was carried out either with different amount of reduction agent or different contact time in order to obtain samples with different Fe^{II}/Fe^{III} ratios. After the reduction, the concentration of major elements in the clay suspension, such as Na, K, Mg, Ca, Si, S, Sr, Al, Fe, were measured using ICP-OES. The non-reduced and reduced clay suspensions are shown in Fig. 3.5. The interlayer (cation exchange) and edge sites availability of these reduced clays were evaluated by sorption experiments. ^{63}Ni sorption experiments on SWy-2 show that interlayer sites of reduced SWy-2 are nearly the same as non-reduced SWy-2, hence, interlayer sites are not affected by the reduction process. In the case of edge sites, ^{152}Eu sorption experiments are ongoing.

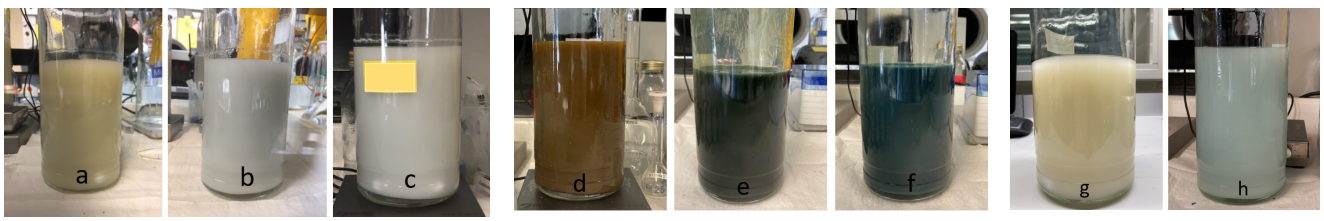

Fig. 3.5: Non-reduced and reduced clay suspensions. (a): non-reduced SWy-2, (b): 1 day CBD reduced SWy-2, (c): 7 days CBD reduced SWy-2, (d): non-reduced NAu-2, (e): high dithionite amount reduced NAu-2, (f): low dithionite amount reduced NAu-2,(g): non-reduced STx-1,(f): fully reduced STx-1.

3.6 Spectroscopic characterisation of cations uptake

The uptake of Zn on two argillaceous rocks, Opalinus Clay (OPA) and Boda Claystone (Boda) was investigated in 0.1 M NaCl electrolyte at pH 7.2 and in an synthetic pore waters (SPW) at pH 8.0 to evaluate the influence of pore water composition. The Zn loadings varied from 1.8 to 86 mmol/kg and from 1.7 to 60 mmol/kg for OPA and Boda, respectively.

The $k^3\chi(k)$ EXAFS spectra of the low loaded OPA and Boda (Zn1, Zn2) samples show remarkable similarities, indicating that Zn uptake in both systems can be explained by the formation of similar inner-sphere complexes (Fig. 3.6a, c). Also, no difference between OPA and Boda samples prepared in NaCl or in SPW were observed at low loadings (Fig. 3.6a, c). With increasing Zn loading the characteristic splitting of the oscillations at 3.8 $Å^{-1}$ is gradually attenuated.

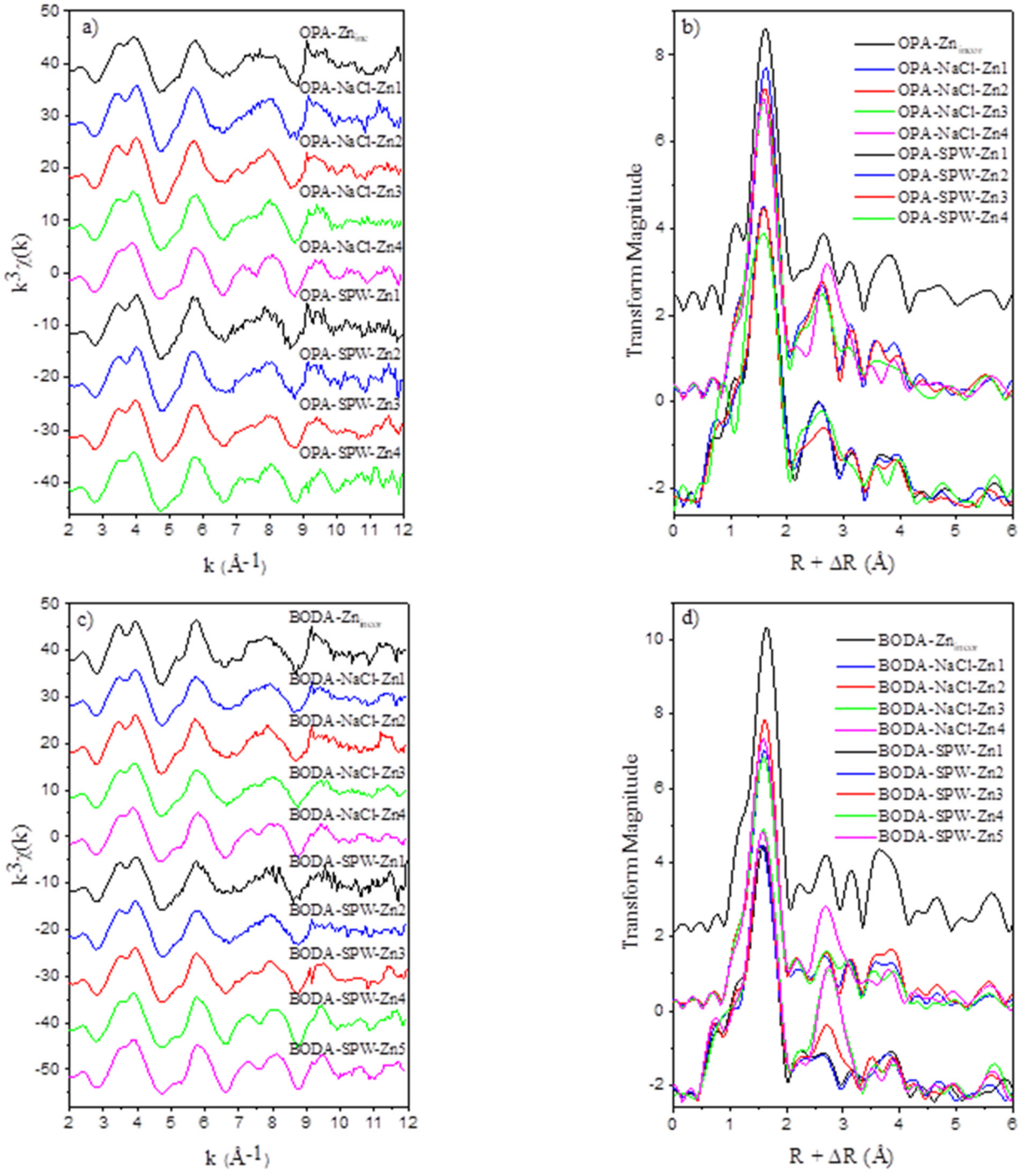

Fig. 3.6: (a,c) Comparison of k^3-weighted Zn K-edge EXAFS spectra of OPA and Boda in NaCl and SPW, (b,d) the corresponding RSFs.

For the samples with higher loadings (16 mmol/kg OPA-SPW-Zn3; 24 mmol/kg Boda-SPW-Zn4) the oscillation at ~8 $Å^{-1}$ show a splitting, indicating the formation of Zn-precipitates (Schlegel et al. 2001). Comparing the highest concentrated OPA (OPA-NaCl-Zn4 vs. OPA-SPW-Zn4) and Boda (Boda-NaCl-Zn4 vs. Boda-SPW-Zn5) samples seems to indicate that in this uptake system the use of SPW favours the formation of precipitates compared to the use of NaCl (Fig. 3.4a, c). The formation of Zn precipitates in the highest concentrated samples is further illustrated in the corresponding RSFs (Fig. 3.4b, d), were a strong RSF peak is observed at $R + \Delta R = 2.54$ Å. At low metal loadings three RSF peaks in the range $R + \Delta R$ between 2 and 4 Å are present.

The spectra of the samples with highest loadings (OPA-NaCl/SPW-Zn3/4, Boda-NaCl-Zn3/4 and Boda-SPW-Zn4/5) were therefore fitted with a model considering the formation of Zn precipitates as already indicated by the $k^3c(k)$ EXAFS spectra. The obtained structural parameters are consistent, in both systems, NaCl and SPW, with the formation of Zn-phyllosilicates at Zn loadings exceeding 16 mmol/kg and 24 mmol/kg for OPA and Boda, respectively.

The extended X-ray absorption fine structure (EXAFS) results support findings based on wet chemistry calculations using the 2SPNE SC/CE sorption model. The differences between argillaceous rock samples prepared in NaCl and SPW are modest indicating that in the case of Zn the clay minerals play a predominant role in the uptake process, and that the effects originating from the pore water are minor. Furthermore, despite the differences in mineralogy both argillaceous rocks show the same uptake behaviour, indicating that the clay minerals are predominantly responsible for the sorption at low and the precipitation processes at higher Zn concentrations.

3.7 COFUND project: Validation of Adsorption Models on Argillaceous Rocks Using Advanced Surface Spectroscopic Techniques

Waste management programmes consider argillaceous rocks as potential host formations for the deep geological repositories. Clay minerals such as illite, smectite, illite/smectite mixed layers and kaolinite are main components in such rock types. The most recognizable characteristic of various clay minerals is their strong cation retention capacity. The advective movement of the nuclides is negligible in clay-rich repositories due to the low water content and the presence of diffusive processes. Likewise, adsorption and precipitation are bound to limit the migration of nuclides. Adsorption, in most natural argillaceous rocks, is complex. The practice to understand these processes is a simplified-component additive approach, providing that only a few types of clay minerals are the preferential adsorbents for radionuclides in clay-dominated environments. This approach has proven to be successful in predicting adsorption on dispersed bentonite and Opalinus Clay systems by using the models for montmorillonite and illite, respectively (Bradbury & Baeyens 2011; Marques Fernandes et al. 2015).

Evaluating the risk related to the release of contaminants requires a comprehensive scientific approach based on a proficient understanding of the uptake mechanisms along the migration pathways. Indeed, the long-term evolution of radionuclides in compacted systems is one of the main pillars on which the safety analysis of future radioactive waste repositories rests. Thus, the retention processes of Zn and the redox sensitive U on intact argillaceous rocks is the focus of this project. Micro-spectroscopic techniques are foreseen to verify whether adsorption is taking place on the clay fraction or other minor phases. The precise nature of the retention mechanism (*i.e.* adsorption, neo-formation, co-precipitation) in both dispersed (extracted fraction) and compacted systems (thin sections) will be investigated with bulk-XAS. Currently, experimental links connecting results from dispersed to compacted systems are very sparse. By applying this approach, it will be possible to determine the spatial distribution of elements of interest, analyse the oxidation state and molecular structure of the adsorbed complexes, and identify reactive crystalline constituents of the heterogeneous rock material.

During this year, the samples related to this project have been prepared. Batch experiments of Zn and Ni with different loadings with montmorillonite and illite were performed and wet paste samples were extracted periodically. Additionally, thin sections from Opalinus Clay samples have been prepared. The samples were in contact with solutions of U at different redox states. Due to the U^{IV} easiness for oxidising, the samples were transported to the micro-XAS beamline for micro-XRF/XAS measurements, at SLS, in a liquid N_2 environment, and measured there in a He cryostat in order to avoid any oxidation. In addition, as reference Th treated Opalinus Clay samples were investigated with micro-XRF/XAS. The beamtime measurements took place very recently, and data analysis is ongoing.

3.8 References

Baes C., Mesmer R. (1976)
The Hydrolysis of Cations. John Wiley & Sons, New York.

Bradbury M.H., Baeyens B. (1997)
A mechanistic description of Ni and Zn sorption on Na-montmorillonite Part II: modelling. Journal of Contaminant Hydrology 27, 223-248.

Bradbury M.H., Baeyens B. (2009)
Sorption modelling on illite. Part II: Actinide sorption and linear free energy relationships. Geochimica et Cosmochimica Acta 73, 1004-1013.

Bradbury M.H., Baeyens B. (2011)
Predictive sorption modelling of Ni(II), Co(II), Eu(IIII), Th(IV) and U(VI) on MX-80 bentonite and Opalinus Clay: A "bottom-up" approach. Applied Clay Science 52, 27-33.

Bradbury M.H., Baeyens B. (2017)
The development of a thermodynamic sorption database for illite and the application to argillaceous rocks. PSI Bericht Nr. 17-06 and Nagra Technical Report NTB 17-14, Paul Scherrer Institut, Villigen PSI, Switzerland.

Dähn R., Baeyens B., Bradbury M.H. (2011)
Investigation of the different binding edge sites for Zn on montmorillonite using P-EXAFS – the strong/weak site concept in the 2SPNE SC/CE sorption model, Geochimica et Cosmochimica Acta 75, 5154-5168.

Hadi J., Wersin P., Mazurek M., Waber H.N., Marques Fernandes M., Baeyens B., Honty M., De Craen M., Frederickx L., Dohrmann R., Sitnikova M.A., Fernandez Diaz A.M. (2017)
Intercomparison of CEC method within the GD project. Mont Terri Technical Report TR 2017-06, Mont Terri, Switzerland.

Kulik D.A., Wagner T., Dmytrieva S.V., Kosakowski G., Hingerl F.F., Chudnenko K.V., Berner U.R. (2013)
GEM-Selektor geochemical modeling package: Revised algorithm and GEMS3K numerical kernel for coupled simulation codes. Comput. Geosci. 17, 1–24. https://doi.org/10.1007/s10596-012-9310-6

Kulik D.A., Marques Fernandes M., Baeyens B. (2018)
The 2SPNE SC/CE sorption model in GEM-Selektor v.3.4 code package (ClaySor): Implementation, tests, and user guide, Nagra NAB 18-27, Wettingen, Switzerland.

Marques Fernandes M., Vér N., Baeyens B. (2015)
Predicting the uptake of Cs, Co, Ni, Eu, Th and U on argillaceous rocks using sorption models for illite. Applied Geochemistry 59, 189-199.

Miron G.D., Kulik D.A., Dmytrieva S.V., Wagner T. (2015)
GEMSFITS: Code package for optimization of geochemical model parameters and inverse modeling. Appl. Geochemistry 55, 28-45.

Motulsky H.J., Christopoulos A. (2004)
Fitting models to biological data using linear and nonlinear regression: A Practical Guide to Curve Fitting. Oxford University Press p. 352.

Newville M. (2001)
IFFEFFIT: interactive XAFS analysis and FEFF fitting. Journal of Synchrotron Radiation 8, 322-324.

Ravel B., Newville M. (2005)
ATHENA, ARTEMIS, HEPHAESTUS: Data analysis for X-ray absorption spectroscopy using IFEFFIT. Journal of Synchrotron Radiation 12, 537-541.

Schlegel M.L., Manceau A., Charlet L., Chateigner D., Hazemann J.L. (2001)
Sorption of metal ions an clay minerals. 3. Nucleation and epitaxial growth of Zn phyllosilicate on the edges of hectorite. Geochimica et Cosmochimica Acta 65, 4155-4170.

Stucki J.W., Golden D., Roth C.B. (1984)
Preparation and handling of dithionite-reduced smectite suspensions. Clays and Clay Minerals 32, 191-197.

Wagner T., Kulik D.A., Hingerl F.F., Dmytrievava S.V. (2012)
Gem-selektor geochemical modeling package: TSolMod library and data interface for multicomponent phase models. Can. Mineral. 50, 1173–1195.

4 RADIONUCLIDES TRANSPORT AND RETENTION IN COMPACTED SYSTEMS AT FULL AND PARTIAL SATURATION

Van Loon L.R., Glaus M.A., Pfingsten W., Baeyens B., Marques Fernandes M., Frick S., Bunic P., Gimmi T., Churakov S.V., Chen Y. (postdoc), Krejci Ph. (PhD student), Chen P. (PhD student), Zerva D. (PhD student)

4.1 Introduction

The retention of radionuclides on clay minerals in engineered and geological barrier systems is a key safety function in the deep geological disposal of radioactive waste. Reliable sorption data (R_d values) and a mechanistic understanding of sorption and transport processes are thus mandatory for a proper evaluation of the barrier safety function. Sorption studies are mainly performed in batch systems using dispersed clay with a low solid to liquid ratio. In such an experimental setup the composition of the solution can be well controlled (e.g. pH, Eh, concentrations of anions and cations, organic and inorganic ligands) and/or varied in order to study their effect on the sorption. Real clay systems, however, are very dense and are characterised by a high solid-to-liquid ratio. It is still an unanswered question whether the data and models derived from dilute dispersed systems can be transferred to the real, compacted ones. The aim of this project is to resolve conceptual difficulties in applying the existing sorption models to diffusion in compacted argillaceous rocks.

A second focus of the project deals with the question whether adsorbed ions should be treated as immobile or only partially mobile species. These two conceptual model assumptions have fundamental implications for the transport behaviour of ions in compacted systems. In the case of full immobilisation, only aqueous ions contribute to the transport, whereas in the case of partial immobilisation both the aqueous and adsorbed ions contribute to the diffusive flux.

Significant quantities of gas are expected to be generated in a repository, either by corrosion of metallic materials or due to degradation of organic waste compounds. Molecular diffusion is an important gas dissipation mechanism helping to reducing potential pressure build-up in the repository near-field. Diffusion studies of gas molecules in fully and partially saturated compacted clay systems is ongoing in the framework of a Marie Skłodowska-Curie COFUND fellowship partially financed by the EU. First results for the diffusion of helium (He) in fully saturated compacted bentonite could be obtained.

4.2 Sorption and diffusion in compacted illite

The concept of the diffusion of charged species in the electrical double layer near the planar surfaces of charged clay minerals ("EDL diffusion") has been invoked to explain the diffusion behaviour of various types of cationic species (Glaus et al. 2015; 2020). Within the scope of this concept, competition effects between different metal cations are not only expected regarding sorption but also for the concentrations of mobile species in the diffuse layer which have a direct impact on the overall diffusive fluxes. In the Donnan approximations, the equilibrium distribution of charged species between the bulk aqueous phase and the diffuse layer is governed by the following equation (Appelo & Wersin 2007) in which c_i refers to the molal concentration of species i with the subscript DL referring to the diffuse layer, z is the charge number, F the Faraday constant, Ψ_{DL} the Donnan equilibrium potential, R the universal gas constant and T the temperature:

$$c_{i,DL} = c_i \exp\left(\frac{-z_i F \Psi_{DL}}{RT}\right) \quad (4.1)$$

The resulting equilibrium species distribution is obtained by solving this equation for all species and taking into account the condition of electroneutrality within the solution and solid phases. The fraction of mobile surface species is therefore directly affected by the presence of competing species in the bulk aqueous phase. Such effects may be of particular importance in the process of compiling diffusion databases for repository conditions. Typical pore waters of Opalinus Clay contain alkaline earth cations, such as Ca^{2+} and Mg^{2+} in concentration ranges of several millimolar. The majority of diffusion experiments performed at LES on pure clay minerals were carried out using simple electrolytes such as NaCl or $NaClO_4$. For the process of upscaling diffusion coefficients from such pure clay systems to clay rocks, it is imperative to take into account adequately the effects of sorption competition between cations present in the electrolyte. Diffusion experiments with different test radionuclides are therefore conducted using compacted illite under variable concentrations of Ca^{2+} in a given NaCl electrolyte. First in-diffusion experiments under such

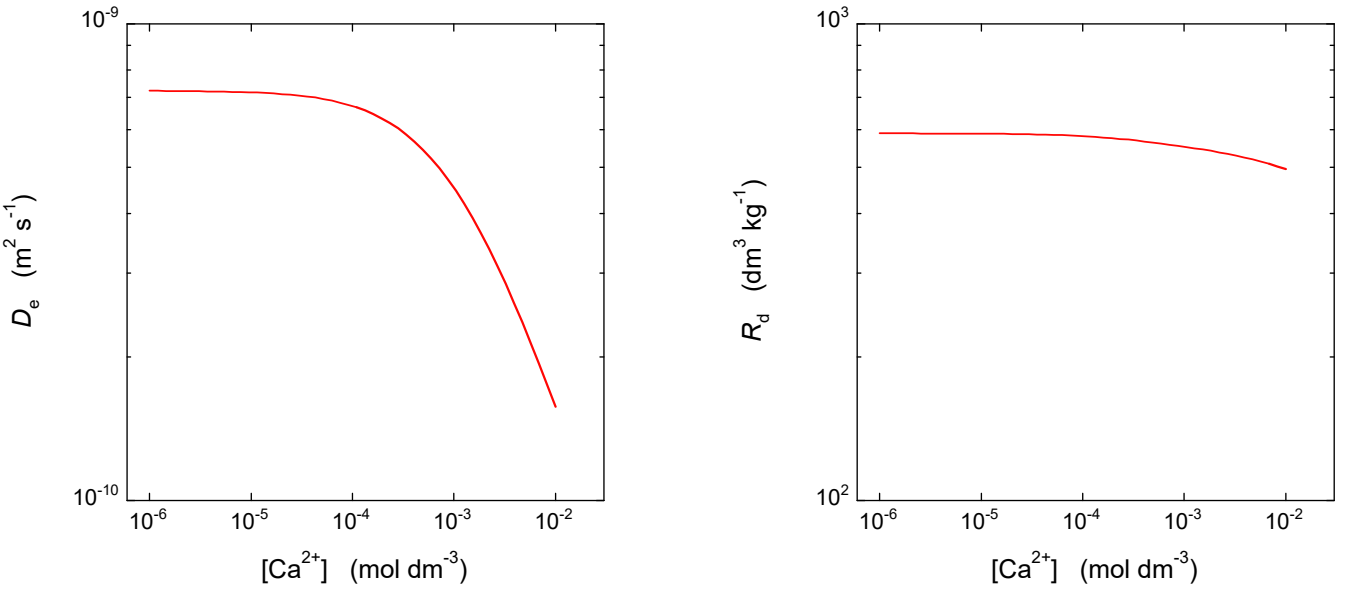

Fig. 4.1: Predicted dependence of D_e and R_d on the Ca^{2+} concentration for the diffusion of a Co^{2+} tracer in homo-ionic Na^+-illite compacted to a bulk dry density of 1700 kg m^{-3} at pH 5 in a 0.1 M NaCl electrolyte containing Ca^{2+} as the competing species.

conditions with Co^{2+} as radiotracer are currently running. Fig. 4.1 shows a blind prediction of the expected effective diffusion coefficients (D_e) and the respective sorption distribution ratios (R_d) for such experiments. As can be seen from Fig. 4.1, the impact of Ca^{2+} on D_e values is stronger than on R_d values. The reason for this behaviour can be found in the different types of surface species of Co^{2+} and their different competition behaviour with Ca^{2+}. According to eq. 4.1, Ca^{2+} can directly compete with Co^{2+} for the presence in the diffuse layer. Both cations bear the same charge. For this reason, D_e values for Co^{2+} show a significant dependence on the concentration of Ca^{2+}. In contrast, R_d values represent the sum of surface species at the planar and the edge surfaces of illite. No competition is expected between Co^{2+} and Ca^{2+} for the latter surface species, which contribute to a major part to sorption under the conditions of the experiment. For this reason, R_d values are expected to be less affected by the presence of Ca^{2+}. No data are available from literature, in which such preferential effects of competing species on diffusion have been demonstrated so far.

4.3 Eurad project FUTURE: Subtask mobility

The experimental programme of the Eurad project FUTURE has been severely affected by the Covid-19 lockdown. Instead a theoretical development of a model for the modified in-/out(I/O)-diffusion method which allows to measure diffusion parameters using small samples of compacted clay minerals has been accomplished and tested based on the data from existing experiments. This technique shall be applied in a later phase of the work to size-fractioned vermiculite. Those experiments will be carried out in close collaboration with the partners from the University of Poitiers, who kindly provided this material to PSI. The practical knowledge gained shall also be applied in the FUTURE project to specially designed diffusion cells used for spectroscopic measurements with synchrotron-based X-ray techniques.

The general idea of the I/O-diffusion method is an optimisation of existing techniques (Van Loon et al. 2003; Van Loon & Jakob 2005). The classical setup used for through-diffusion experiments requires up to 10 g of dry clay material for a single experiment. For many applications, the amount of available purified material is much less. One possibility to solve this problem would be the use of the membrane-confined diffusion cells (Glaus et al. 2015) which require only a few hundreds of milligrams of clay material. These cells were designed for in-diffusion, but not for through-diffusion experiments. However, they could be used in an out-diffusion mode after homogeneous full saturation of the clay with the tracer. Design calculations have shown that parameters discrimination would be feasible with an accuracy of 10-15% regarding effective diffusion coefficients and rock capacity factors, which is adequate for many purposes.

Diffusion measurements of HTO and $^{36}Cl^-$ as the test radionuclides are being carried out by the I/O-method using compacted homoionic Na^+ and K^+ illite equilibrated with Na^+ or K^+, respectively, electrolytes at various concentrations. The comparison of electrical double layer (EDL) diffusion in homoionic K^+ illite is unexplored and has not been published yet. The variation of the ionic strength will give new insights in

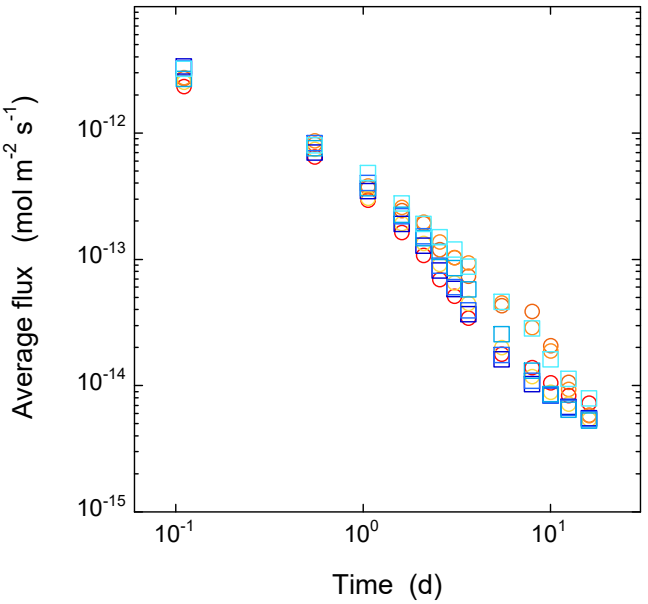

Fig. 4.2: HTO fluxes measured using the I/O method from compacted illite samples (1500 kg m^{-3}), previously saturated homogeneously with HTO tracer. Red colours refer to experiments with homo-ionic Na^+-illite, blue colours to experiments with K^+-illite. Colour gradations indicate increasing ionic strength of the bulk aqueous phase (0.01, 0.03, 0.1, 0.3 M) with increasing colour intensity.

the parametrisation of the EDL diffusion and sorption model and may serve as a basis for potential discrimination of related models (e.g. pure cation exchange). First results for the out-diffusion of HTO are shown in Fig. 4.2. As can be expected for an uncharged tracer, the results of HTO diffusion experiments do not exhibit a measurable dependence on the salinity of the bulk aqueous phase. Further, no significant difference between the results of the Na^+- and the K^+-conditioned illite could be seen. In that sense, the eight datasets directly reflect the intrinsic precision of the I/O-diffusion method, which is within the scope of classical through- and out-diffusion tests.

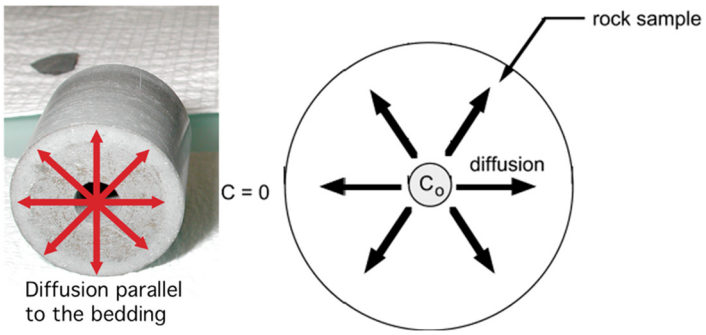

Fig. 4.3: Experimental set-up of the radial diffusion experiment from Van Loon et al. (2004).

The reliability of the average fluxes measured after short times might be rather poor, because the experiments start with a discontinuity of tracer concentration between the clay and the solution phase. Whether such a discontinuity will lead to useful results, was not clear from the beginning. The homogeneity of the data in the first measuring point indicates that they are rather trustworthy. However, this question and the validity of the technique can only be assessed finally after quantitative numerical simulation of the experiments.

4.4 Sequential modelling of the diffusion of cations, anions and neutral tracers through Opalinus Clay

Diffusion of HTO, Cl and Na in Opalinus Clay was modelled applying a sequential modelling framework to experimental data of Van Loon et al. (2004) (see Figure 4.3 for the experimental set-up).

First, accessible porosity and tortuosity of water and anions were determined from HTO (Figure 4.4a) and Cl diffusion experiments, respectively, using a classical Fickian pore diffusion model. Second, Cl diffusion (Figure 4.4b) was modelled again with the found tortuosity, but now applying the anion exclusion model of Wigger and Van Loon (2018). Here, the pore space is divided in a free (of charge) porosity, diffuse-layer (DL) porosity and an anion inaccessible porosity (interlayer and bottleneck porosity). DL diffusion was modelled using the Donnan approach (Gimmi & Alt-Epping 2018) with 45% of the surface charge being compensated in the DL. Third, Na diffusion was modelled with the Donnan approach (45% charge in the DL, the remaining 55% by ion exchange) using the tortuosity of water and diving the water accessible porosity into a free porosity (same as for Cl) and DL porosity (the same porosity found for Cl plus the interlayer and bottleneck porosity). A surface mobility of 0.32 of more specifically sorbed Na had to be included in order to match the experimental data (Figure 4.4c). The use of this sequential modelling framework allows for a description of diffusion of HTO, Cl and Na with a consistent set of parameters.

4.5 Gas diffusion in partially saturated clay systems

Large amounts of gas will be produced in a repository due to corrosion of steel and degradation of organic waste forms (Diomidis et al. 2016). Whether these gases have a negative effect on the barrier system depends strongly on the permeability of the barrier systems for gases. An institutional Marie Skłodowska-Curie COFUND postdoc project (Yanhua Chen) on gas diffusion in compacted clay systems is ongoing since August 2019. The main emphasis of the project is on

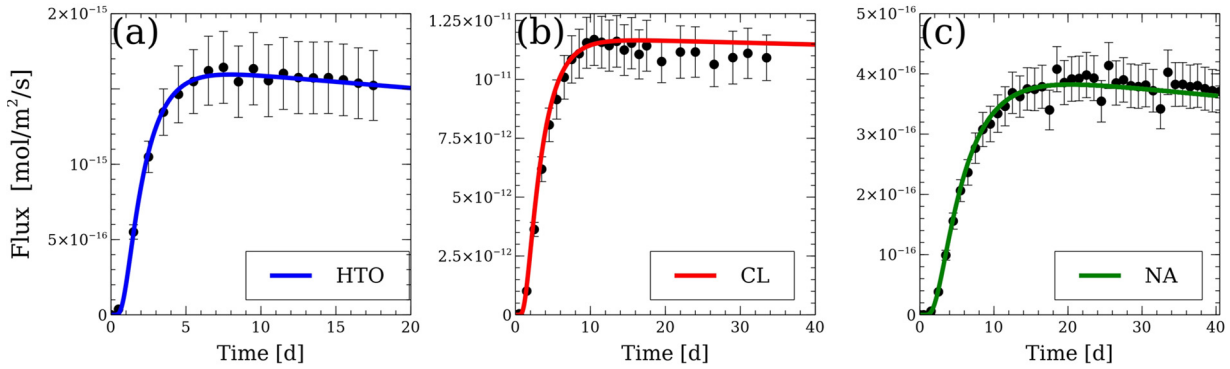

Fig. 4.4: Results of the radial diffusion experiment: HTO flux (left, blue line), Cl flux (middle, red line) and Na flux (right, green line) on the outer boundary of the Opalinus Clay sample; Black dots with error bars: experimental data.

measuring the diffusion of selected gases in partially saturated clay systems such as compacted bentonite, bentonite/sand mixtures and Opalinus Clay. A new gas-tight equipment was designed and developed to keep the clay sample at a well-defined saturation degree during a through-diffusion experiment. A schematic overview of the equipment (a gas diffusion cell coupled with a mass spectrometer - GD-MS) is shown in Fig. 4.5.

Two reservoirs are separated from each other by a sample holder, in which the clay sample is confined between two porous filters. The reservoirs are filled with a saturated salt solution and selected gases at a given pressure. Saturation of the clay materials is achieved by equilibrating the clay sample with a controlled water vapour phase at a relative humidity (RH) given by the salt solution (Wexler & Hasegawa

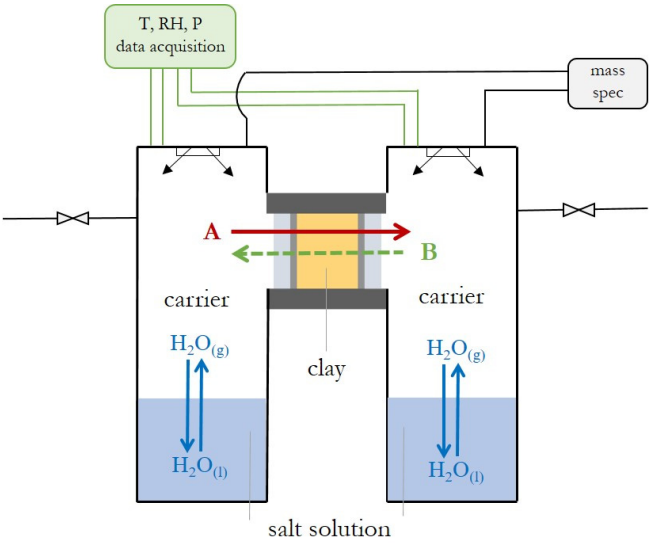

Fig. 4.5: Schematic overview of GD-MS A: a gas tracer (B: optional tracer gas).

1954). Time series data of temperature, pressure and RH in both reservoirs are recorded with Labview. Gas compositions in both reservoirs are measured in line with the Mini-Ruedi mass spectrometric (MS) system (Brennwald et al. 2016).

Prototype performance test was started in July 2020 with the focus on gas tightness of the experimental system and the Mini-Ruedi analytical feasibility. Prior to the diffusion experiment, the system (without clay sample, not connected to MS) was checked for its airtightness at 1.8 bar for 5 days. The pressure remained constant during this period, and the system was considered to be airtight. Argon (Ar)-tightness was confirmed in a similar way where the system was pressurised with 2 bar Ar for 7 days.

A compact Volclay sample (φ_{tot}=0.42, "Øxd" = 2.56 cm x 0.97 cm, ρ_{db}=1626 kg/m^3) was used for a first diffusion experiment. The Volclay sample was saturated with water vapour in a desiccator (RH=100%) and had an initial saturation degree (Ω) of 1 before the assembly to the GD-MS. Both reservoirs were filled with water and gases at 1.5 bar, where helium (He) and argon (He:38.7 vol %) were used in the upstream and argon was used in the downstream reservoir. A He and Ar mixture (He: 50 vol%) was used as standard gas for MS measurements. The He concentrations in both reservoirs were measured with MS (Fig. 4.6).

100% mass recovery was not achieved for He. The reasons are 1) gas consumption due to MS, and 2) helium leakage in the upstream reservoir. The gas flow rate through the MS capillary was determined to be 0.1 cm^{3}STP min^{-1}. The total gas flow through the capillary is not a perfectly linear function of the total gas pressure at the capillary inlet; therefore, the actual flowrate under the experimental conditions is larger than 0.1 cm^3 min^{-1}. Gas properties, especially the viscosity, affect the gas flow through the MS as well.

The total pressures at the last measurement were 1.12 bar (upstream) and 1.46 bar (downstream), suggesting that there was a He leakage in the system. The leakage rate was determined to be less than 1×10^{-5} atm cc/s. The He-tightness is currently improved by adding extra copper sealings and replacing connections and threads in the GD-MS. A thermodynamic conductivity gas analyser (FT300, Messkonzept GmbH, Germany) is planned to be tested for the online gas measurements, with which no gas consumption due to analytics should be observed. Gas transport modelling is carried out with FEniCS-GEMS (Kosakowski & Damiani 2020), which is used to model the Mont Terri Hydrogen Transfer (HT) experiment (Vinsot et al. 2017). Calculations are alternatively performed with COMSOL Multiphysics®.

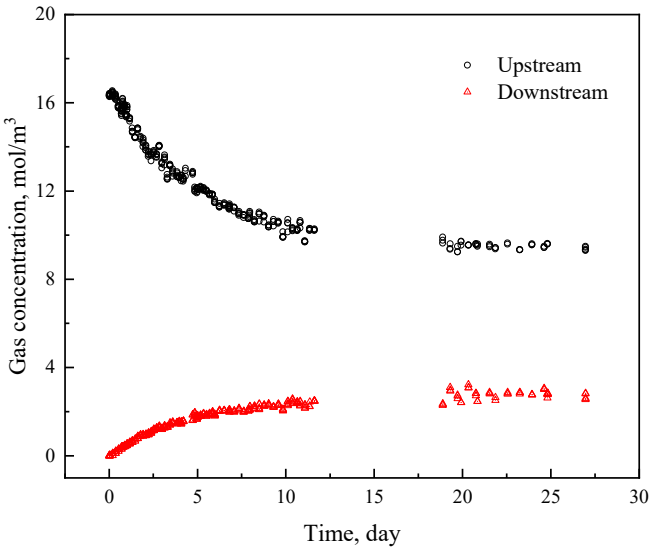

Fig. 4.6: Evolution of the upstream and downstream helium concentration with time.

4.6 References

Appelo C.A.J., Wersin P. (2007)
Multicomponent diffusion modeling in clay systems with application to the diffusion of tritium, iodide, and sodium in Opalinus Clay. Environmental Science and Technology 41, 5002–5007.

Brennwald M., Schmidt M., Oser J., Kipfer R. (2016)
A Portable and autonomous mass spectrometric system for on-site environmental gas analysis. Environmental Science and Technology 50, 13455-13463.

Diomidis N., Cloet V., Leupin O.X., Marschall P., Poller A., Stein M. (2016)
Production, consumption and transport of gases in deep geological repositories according to the Swiss disposal concept. Nagra Technical Report NTB 16-03, Nagra, Wettingen, Switzerland.

Gimmi T., Alt-Epping P. (2018)
Simulating Donnan equilibria based on the Nernst-Planck equation. Geochimica et Cosmochimica Acta 232, 1–13.

Glaus M.A., Aertsens M., Appelo C.A.J., Kupcik T., Maes N., Van Laer L., Van Loon L.R. (2015)
Cation diffusion in the electrical double layer enhances the mass transfer rates for Sr^{2+}, Co^{2+} and Zn^{2+} in compacted illite. Geochimica et Cosmochimica Acta 165, 376–388.

Glaus M.A., Frick S., Van Loon L.R. (2020)
A coherent approach for cation surface diffusion in clay minerals and cation sorption models: Diffusion of Cs^{+} and Eu^{3+} in compacted illite as case examples. Geochimica et Cosmochimica Acta 274, 79–96.

Kosakowski G., Damiani L.H. (2020)
Modeling gas fluxes for the Mont Terri experiment. TM-44-19-24.

Van Loon L.R., Soler J.M., Bradbury M.H. (2003)
Diffusion of HTO, $^{36}Cl^{-}$ and $^{125}I^{-}$ in Opalinus Clay samples from Mont Terri. Effect of confining pressure. Journal of Contaminant Hydrology 61, 73–83.

Van Loon L.R., Soler J.M., Müller W., Bradbury M.H. (2004)
Anisotropic diffusion in layered argillaceous rocks: A case study with Opalinus Clay. Environmental Science and Technology 38, 5721–5728.

Van Loon L.R., Jakob A. (2005)
Evidence for a second transport porosity for the diffusion of tritiated water (HTO) in a sedimentary rock (Opalinus Clay - OPA): application of through- and out-diffusion techniques. Transport in Porous Media 61, 193–214.

Vinsot A., Appelo C.A.J., Lundy M., Wechner S., Cailteau-Fischbach C., de Donato P., Pironon J., Lettry Y., Lerouge C., De Cannière P. (2017)
Natural gas extraction and artificial gas injection experiments in Opalinus Clay, Mont Terri rock laboratory (Switzerland). Swiss Journal of Geosciences 110, 375–390.

Wexler A., Hasegawa S. (1954)
Relative humidity-temperature relationships of some saturated salt solutions in the temperature range 0 degree to 50 degrees C. Journal of Research of the National Bureau of Standards 53, 19.

Wigger C., Van Loon L.R. (2018)
Effect of the pore water composition on the diffusive anion transport in argillaceous, low permeability sedimentary rocks. Journal of Contaminant Hydrology 213, 40–48.

5 RADIOACTIVE WASTE CHARACTERISATION

Wieland E., Curti E., Kulik D.A., Miron D.G., Tits J., Kunz D., Laube A., Guillemot T. (postdoc)

5.1 Introduction

This chapter summarises the research activities related to the characterisation of radioactive waste materials, currently focusing on activated steel, spent fuel and vitrified high-level waste. This project aims at providing important information on the source term (e.g. release rates, speciation) of the radionuclides released from the waste materials in the planned repositories for high-level (HLW) and low- and intermediate-level waste (L/ILW). The source term influences directly and indirectly several safety assessment parameters and calculations related to the other repository compartments (near-field, geosphere, biosphere). The source term is a time-dependent parameter strongly affected by the temporal evolution of the waste materials, which are subjected to chemical degradation processes, such as corrosion of irradiated steel, (bio-) chemical degradation of organic matter, or the dissolution of spent fuel and vitrified high-level waste. Besides changes caused by the evolution of the physical-chemical conditions such as pH, temperature and redox potential, time dependence of radionuclide release from waste materials is thus a direct consequence of the degradation of waste materials themselves. For this reason, investigations of the waste properties have been identified as an area of research that is important for the Swiss waste disposal programme over the coming years and possibly also beyond the general licence application.

5.2 C-14 Project: Release and speciation of ^{14}C-bearing compounds

In Switzerland, the ^{14}C inventory in the L/ILW is mainly associated with irradiated metallic waste components (~ 75 %) (Johnson & Schwyn 2008). The largest portion of ^{14}C-bearing compounds is therefore released to the aqueous and gas phases of the near-field of a deep geological L/ILW repository during corrosion of irradiated steel. The presence of ^{14}C in irradiated steel can be attributed to the activation of nitrogen impurities contained in nuclear fuel and reactor core components of nuclear power plants through the nuclear reaction ^{14}N(n,p)^{14}C. ^{14}C is considered as a significant dose-contributing radionuclide in safety assessments due to its long half-life (5730 years), the high mobility of ^{14}C-carrying gaseous and dissolved compounds caused by weak interaction with mineral surfaces in the far-field, and because it might be incorporated in the human food chain (Nagra 2002; Nuclear Decommissioning Authority 2012). The chemical form of the ^{14}C-carrying species dictates the routes of ^{14}C migration in the engineered barrier system of a deep geological repository and the surrounding host rock, and therefore determines the long-term contribution of ^{14}C to dose release from a repository for radioactive waste. Current safety assessments are based on simplifying assumptions regarding the ^{14}C speciation because of missing comprehensive corrosion studies with irradiated metals allowing long-term monitoring of the ^{14}C compounds formed (Wieland & Hummel 2015; Swanton et al. 2015). To support future safety assessment, a laboratory-scale experiment is being carrying out with the aim of identifying and quantifying the ^{14}C-bearing carbon compounds released during corrosion of irradiated steel in anoxic and highly alkaline conditions. The latter conditions simulate the long-term chemical environment in a cement-based L/ILW repository.

Acknowledgement: Compound-specific radiocarbon analysis (CSRA) was developed in co-operation with Prof. Dr. S. Szidat, Dr. G. Salazar and M. Rauber (Department of Chemistry & Biochemistry at the University of Bern, Switzerland). The project has been partially funded by Nagra in the framework of an ongoing postdoctoral study (Dr. T. Guillemot (postdoc): *"Carbon-14 project: Investigation of the C-14-containing species released during corrosion of irradiated steel"*. Start date: January 2019; Funding: Nagra).

5.2.1 Corrosion experiment with irradiated steel

Since May 2016, a long-term corrosion experiment with irradiated steel is running at the Paul Scherrer Institut and allows regular samplings of both liquid and gas phases from a reactor (Cvetković et al. 2018a). Inside the gas-tight reactor, two 1 g specimens prepared from steel nuts irradiated in nuclear power plant Gösgen (Schumann et al. 2014) are immersed in alkaline cement-type pore solution ($Ca(OH)_2$ saturated solution, pH = 12.5) under a N_2 atmosphere (Wieland et al. 2018). Scoping calculations carried out prior to the start of the experiment suggested that extremely low ^{14}C concentrations can be expected to release to the liquid and gas phases due to the very low corrosion rate of irradiated steel in alkaline solution, the limited sample size and the relatively low ^{14}C inventory of the irradiated steel specimens mounted in the reactor (Wieland & Cvetković 2015). Thus, these constraints required the development of very sensitive compound-specific radiocarbon analysis (CSRA) based on

chromatographic separation techniques in combination with ^{14}C quantification by accelerator mass spectrometry (AMS) both for application in solution and gas phase (Cvetković et al. 2018b; Guillemot et al. 2020a).

5.2.2 Development of CSRA for gaseous carbon compounds

In 2020, we focused on the final development of CSRA for the gaseous ^{14}C-bearing compounds. It is expected that small ^{14}C-containing hydrocarbons (HCs), such as methane, ethane etc., are formed during corrosion of irradiated steel, according to the results from previous batch-type experiments performed with non-irradiated zero-valent iron powders in anoxic alkaline conditions (LES progress report 2019; Cvetković et al. 2018c; Guillemot et al. 2020b).

The development of CSRA for the gaseous HCs is based on the separation of individual ^{14}C-bearing carbon compounds by gas chromatography (GC) and ^{14}C quantification by AMS. In the PSI Hotlab, the gas samples are injected into a GC to separate the HCs from each other. Then, the individual HCs are oxidised to $^{14}CO_2$ in an oxidation oven, which is connected to the GC, and $^{14}CO_2$ is collected in separate sampling loops of a custom-made fraction collector (Fig. 5.1). Each sampling loop allows the $^{14}CO_2$ equivalent of an individual ^{14}C-carrying hydrocarbon to be trapped from a gas mixture based on its retention time during chromatographic separation. Afterwards, the fraction collector is brought to the Laboratory for the Analysis of Radiocarbon (LARA) at the University of Bern and connected to the MIni CArbon DAting System (MICADAS) for ^{14}C AMS measurements. At LARA, the CO_2 trapped in the sampling loops of the fraction collector is purged into a gas interface system (GIS), from which it is subsequently injected into the AMS ion source (Fig. 5.1).

The major challenge in the course of the development of CSRA for ^{14}C-bearing HCs was to ensure that a minimal amount of ^{12}C, in the chemical form of ^{14}C-free stable carbon compounds, is injected into the GC, trapped in the sampling loops of the fraction collector and finally released into the AMS to obtain reliable and reproducible measurements of the $^{14}C/^{12}C$ ratio by AMS. A series of tests were previously carried out in 2019 with the aim of identifying potential losses of stable carbon in the different parts of the entire analytical set-up and optimising injection of stable carbon. The injection mode of the gas samples into the GC, *i.e.* the splitless time that was set, was identified as the only source of stable carbon loss in the device, reaching a 20 % loss of the initial stable carbon injected. The efficiencies of both oxidation and reduction ovens were also checked but no loss of stable carbon was observed when passing though these devices. The same conclusion was drawn for the water separator and the sampling loops of the fraction collector, which were found to be perfectly gas-tight. In 2020, the capacity of the oxidation oven was tested after five years of operation. The oxidation oven has a limited capacity to oxidise hydrocarbons into CO_2. Oxidation of the hydrocarbons to CO_2 fails once this limit is reached and the catalyst of the oxidation oven has to be regenerated. Failure of the oxidation process gives rise to erroneous ^{14}C measurements by AMS, which requires injection of CO_2.

The limit of capacity was first determined by a series of consecutive injections with 50 µg stable carbon in the chemical form of fossil CH_4 (Fig. 5.2; dark filled circles; left y-axis) (Guillemot et al. 2020a). The amount of stable carbon was injected into the GC via a 100 µL injection loop (sample loop) simultaneously with 500 µL He via a second injection loop (carrier loop).

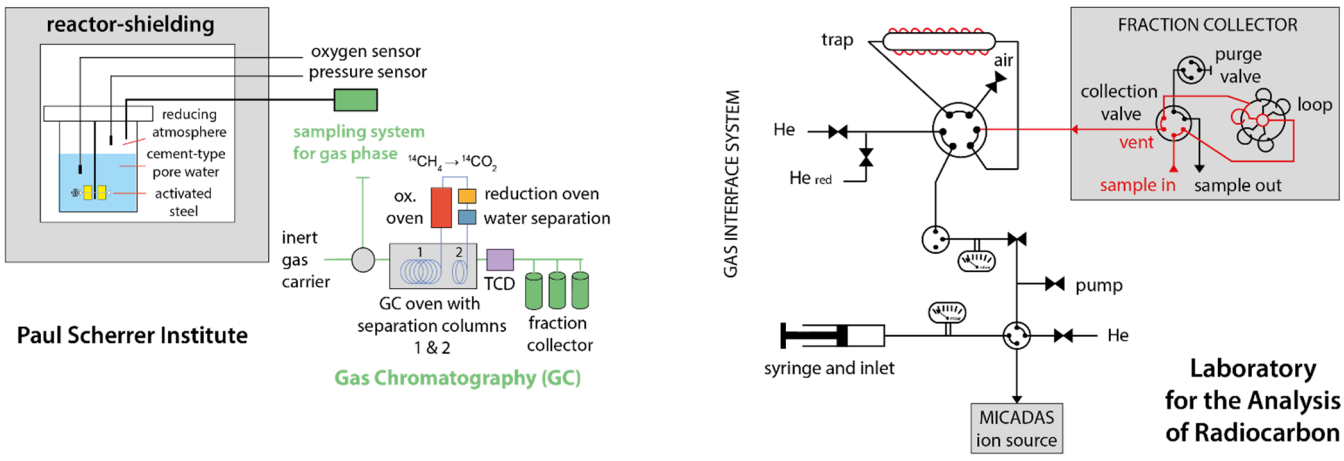

Fig. 5.1: Left: Set-up of the reactor and the GC system used to separate and collect ^{14}C-carrying carbon compounds. Samples were prepared in the PSI Hotlab. Right: Connection between the fraction collector and the AMS through the GIS for ^{14}C quantification.

It was anticipated that the appearance in the thermal conductivity detector (TCD) of a small peak of CH_4 in addition to the one of CO_2 would indicate the limit of capacity of the oxidation oven. However, it was not possible to detect any CH_4 peak, even after injecting more than 2500 µg C (data not shown). Nevertheless, a decrease of the CO_2 peak area was observed after the injection of 600 µg C into the GC, which corresponds to a capacity of 480 µg C by taking into account the 20 % loss of carbon attributed to the applied injection mode (Fig. 5.2). A decrease of the peak area is an indication of incomplete C oxidation. It cannot be attributed to a loss of sensitivity by the TCD because injections of 50 µg C as fossil CH_4 were also realised with the oxidation oven turned off (T = 400 °C), thus impeding oxidation of CH_4 into CO_2, which resulted in identical peak areas (Fig. 5.2; open squares; right y-axis). The capacity was further determined by conducting a series of consecutive injections with 60 µg C in the chemical form of fossil C_2H_6 along with 500 µL He (Fig. 5.2; grey filled circles; left y-axis) (Guillemot et al. 2020a). The same trend in the CO_2 peak areas was observed as in the case of CH_4 injection, thus confirming that the limit of capacity of the oxidation oven is reached at approximately 600 µg injected C (*i.e.* effective 480 µg C) (Guillemot et al. 2020a).

The CO_2 peak area detected by the TCD linearly increases as a function of increasing amounts of C injected (*i.e.* 20, 30, 40, 50, 60 and 100 µg C) as shown in Fig. 5.2b. This proves that complete oxidation of the HCs occurs when the oxidation oven was operated at T = 1000 °C and its capacity limit was not reach.

In the course of CSRA development for gaseous carbon compounds, the optimal amount of injected stable carbon was found to be 50 µg for obtaining stable and reproducible measurements of the $^{14}C/^{12}C$ ratio by the AMS. It was therefore decided to regenerate the catalyst of the oxidation oven after the trapping of one compound in the seven loops of the fraction collector, which results in totally seven injections and a maximum loading of ~ 280 µg C of the catalyst.

The carbon recovery of the AMS was determined by sequentially injecting 50 µg C in the chemical form of fossil CH_4 into the GC, oxidising fossil CH_4 to CO_2 in the oxidation oven and trapping CO_2 in the sampling loops of the fraction collector (Guillemot et al. 2020a). The CO_2 was then released into the MICADAS via the GIS for ^{14}C AMS measurements. Out of the 50 µg C injected into the GC, about 40 µg should reach the MICADAS ion source by taking into account the 20 % loss of stable carbon due to the applied injection mode (splitless time). This statement can be verified as the amount of CO_2 released into the AMS source can be manometrically quantified by the syringe mounted in the GIS (Fig. 5.1). The results showed that only between 18 and 34 µg CO_2 were detected by the GIS, which corresponds to an overall carbon recovery ranging between 36 and 68 % from the initial injection into the GC to the AMS detection (Tab. 5.1; Run A). These lower values reveal that a portion of stable carbon was lost between CO_2 release from the fraction collector and its injection into the AMS ion source. Even if the origin of this new loss is still not perfectly determined (*i.e.* too short collection time or efficiency of the GIS trap), the ^{12}C-related current detected by the Faraday cup was always > 5 µA (Tab. 5.1; Run A), which is above the minimum current of 2 µA required for robust ^{14}C AMS measurements at LARA. No further attempts were made to unravel the reason for the reduced carbon recovery in the GIS/AMS system because the ^{14}C measurements were highly

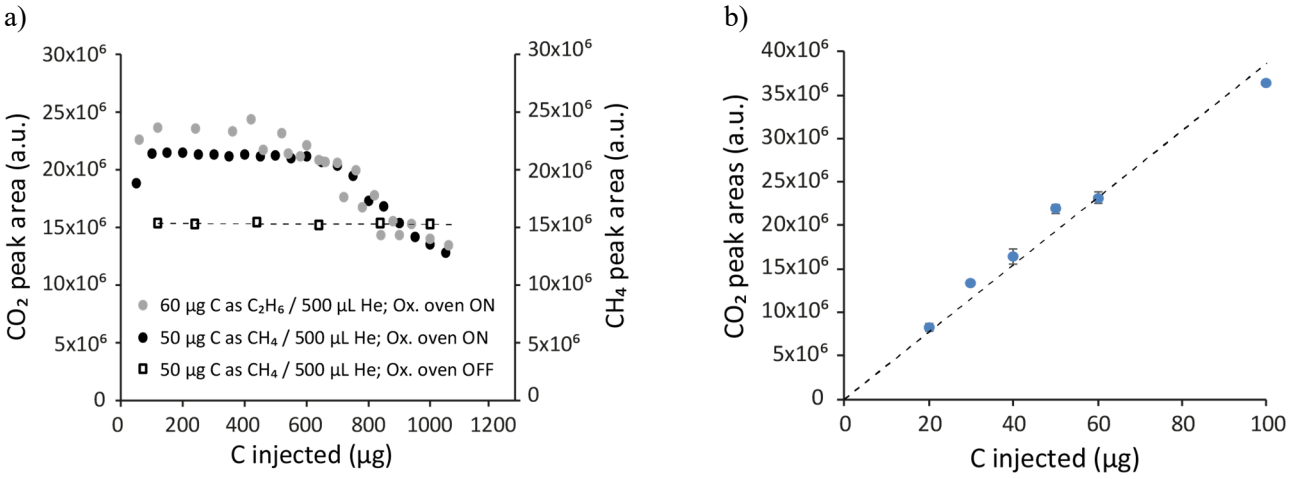

Fig. 5.2: a) Capacity tests of the oxidation oven at 1000 °C. Black filled circles: CO_2 peak areas obtained by subsequently injecting 50 µg C as fossil CH_4. Grey filled circles: CO_2 peak areas obtained by subsequently injecting 60 µg C as fossil C_2H_6. Open squares: CH_4 peak area obtained by subsequently injecting 50 µg C as fossil CH_4 with the oxidation oven switched off. b) CO_2 peak area (oxidised CH_4) as a function of the amount of C injected.

Tab. 5.1: $F^{14}C$ (fraction modern carbon) records obtained when 50 µg stable carbon (as fossil CH_4) were injected into the GC, oxidised to CO_2, trapped by the sampling loops of the fraction collector and released into the AMS through the GIS. The $F^{14}C$ values were corrected with the AMS blank (fossil $^{12}CO_2$) at the beginning of each sequence. The weight of carbon injected into the AMS was determined by the manometric system of the GIS and allowed the calculation of the overall total carbon recovery. The reference $F^{14}C$ value of the modern CH_4 is 1.024 ± 0.003 (Espic et al. 2019).

Run	Fraction collector loop	Sample	^{12}C (µA)	$F^{14}C$	Uncertainties (%)	Carbon injected into the AMS (µg)	Overall carbon recovery (%)
A	-	AMS blank	5.91	0.010	8.3	-	-
B			6.81	0.011	7.6		
A	#2	fossil CH_4	5.72	0.021	8.0	21	42
B			5.15	0.038	7.3	26	52
A	#3	fossil CH_4	6.05	0.011	13.4	18	36
B		modern CH_4	4.76	1.005	1.1	39	78
A	#4	fossil CH_4	5.60	0.003	45.5	34	68
B		modern CH_4	5.67	1.017	1.1	32	64
A	#5	fossil CH_4	5.09	0.029	6.5	27	54
B			5.84	0.035	5.9	32	64
A	#6	fossil CH_4	5.47	0.007	20.3	28	56
B		modern CH_4	5.17	0.997	1.1	31	62
A	#7	fossil CH_4	5.65	0.010	17.4	23	46
B		modern CH_4	6.17	1.023	1.1	24	48
A	#8	fossil CH_4	5.81	0.007	22.1	33	66
B			6.32	0.024	8.9	22	44

reproducible and resulted in a mean value of the background of 0.012 $F^{14}C$ (fraction modern carbon) with a very low standard deviation of 0.008 $F^{14}C$ (Tab. 5.1; Run A).

A second run was conducted by injecting 50 µg C as fossil CH_4 and 50 µg C as modern CH_4 (Tab. 5.1; Run B) with the aim of detecting a potential cross-contamination during the successive release of samples having different ^{14}C contents. Fossil and modern CH_4 were alternatively trapped in the different loops of the fraction collector and released into the AMS. For example, fossil (^{14}C-free) CH_4 was trapped in sampling loops #2, #5 and #8, while modern CH_4 was trapped in the sampling loops #3, #4, #6 and #7. As expected, fossil and modern CH_4 have distinct $F^{14}C$ signatures with an average of 0.032 ± 0.007 $F^{14}C$ and 1.010 ± 0.011 $F^{14}C$, respectively (Tab. 5.1; Run B). The low standard deviation shows a good reproducibility of the measurements. Furthermore, no cross-contamination occurred when different ^{14}C contents were successively injected into the AMS (Tab. 5.1; Run B).

5.2.3 Determination of the speciation of ^{14}C in the corrosion experiment with irradiated steel

In May 2020, an additional sampling of the liquid and gaseous phases of the corrosion experiment with irradiated steel was carried out. The analytical developments pursued in the last years enable us to quantify several ^{14}C-related parameters in both phases: 1) the total organic ^{14}C content ($TO^{14}C$) of the solution, 2) the total inorganic ^{14}C content ($TI^{14}C$) of the solution, 3) CSRA of dissolved, single ^{14}C-carrying organic compounds, 4) the total ^{14}C content of the gas phase ($TG^{14}C$), and 5) CSRA of gaseous, single ^{14}C-carrying compounds.

The $TO^{14}C$ is a measure of ^{14}C associated with dissolved organic carbon compounds, which was determined by adapting the classical procedure (wet oxidation in 10 % $K_2S_2O_8$/5 % H_3PO_4 solution) for AMS-based ^{14}C analysis (Rauber 2018). This parameter was determined before and after filtrating the sample solution through an anion exchanger

cartridge (OnGuard Ag/Ba/H-cartridge, ThermoFisher Scientific/Dionex, Sunnyvale, CA, USA) to remove interfering anions (e.g. Cl^-) and to adjust pH ~ 6, which was required to improved peak resolution during chromatographic separation of single compounds by ion chromatography (IC). $TI^{14}C$ corresponds to ^{14}C associated with ^{14}C-carrying carbonate and was determined by adapting the classical procedure (acidification with 8.5 % H_3PO_4 and removing CO_2 by a gas purge) for use in ^{14}C quantification by AMS. The protocol used for the $TO^{14}C$ and $TI^{14}C$ measurements were developed by Rauber (2018). $TG^{14}C$ corresponds to the total ^{14}C content in the gas phase, which was determined by oxidising a small volume in the oxidation oven to $^{14}CO_2$ and quantifying ^{14}C by AMS (Guillemot et al. 2020a). CSRA for the liquid and gaseous phases were carried out by chromatographically separating single carbon compounds by IC in case of dissolved carbon compounds or GC in the case of HCs, respectively, with subsequent oxidation to $^{14}CO_2$ in the case of the gaseous carbon compounds and ^{14}C quantification by AMS.

Fig. 5.3 shows a comparison of the proportions of ^{14}C in the gas phase ($TG^{14}C$) and in the liquid phase ($TI^{14}C$, $TO^{14}C$) for the samplings carried out in 2019 (day 1114, day 1252) and in 2020 (day 1462). The results show that the ^{14}C content in the gas phase tends to increase with time, *i.e.* from 42 ± 2 % to 50 ± 4 %, while the proportions of ^{14}C associated with dissolved carbon compounds (organics, carbonate) correspondingly decrease with time (^{14}C proportions normalised to the total ^{14}C for a sampling). This finding is further illustrated in Fig. 5.4, which shows time-dependent changes in $TO^{14}C$ and $TG^{14}C$. The release rate of ^{14}C determined by $TO^{14}C$ (expressed in moles per surface are of the corroding irradiated steel nuts specimens) is constant over time after an initial rapid increase within the first ~ 30 days of corrosion (Fig. 5.4a), while the release rate of ^{14}C to the gas phase ($TG^{14}C$) slowly but steadily increases with time (Fig. 5.4b). The rapid increase of ^{14}C in the chemical form of organic carbon compounds ($TO^{14}C$) in the first stage of the corrosion process is attributed to the release of oxidised chemical forms of carbon, such as carboxylic acids. In previous studies with non-irradiated iron powders we showed that the carboxylic acids might form during exposure of iron to oxic conditions, that they can be accommodated in the oxide layer on the surface of iron and eventually instantaneously released to the alkaline solution by desorption (Cvetković et al. 2018a; Guillemot et al. 2020b). The rate of release of $TO^{14}C$ observed in the corrosion experiment with irradiated steel corroborates these earlier conclusions. Note that the first measurements also indicate that $TI^{14}C$ was stable within the error range over time (data not shown), similar to $TO^{14}C$ (Fig. 5.4a), indicating that ^{14}C-carrying carbonate was also released to solution in an early stage of the corrosion process. $TI^{14}C$ reached ~ 15 % in proportion to $TO^{14}C$ and total ^{14}C in the gas phase (Fig. 5.3). We can exclude that the presence of ^{14}C-carrying carbonate is the consequence of initial contamination as the ^{14}C background associated with the alkaline solution in the reactor was subtracted from the measured $F^{14}C$ values and contamination due to ingress of air (naturally produced $^{14}CO_2$) would result in an increase in $TI^{14}C$ with time.

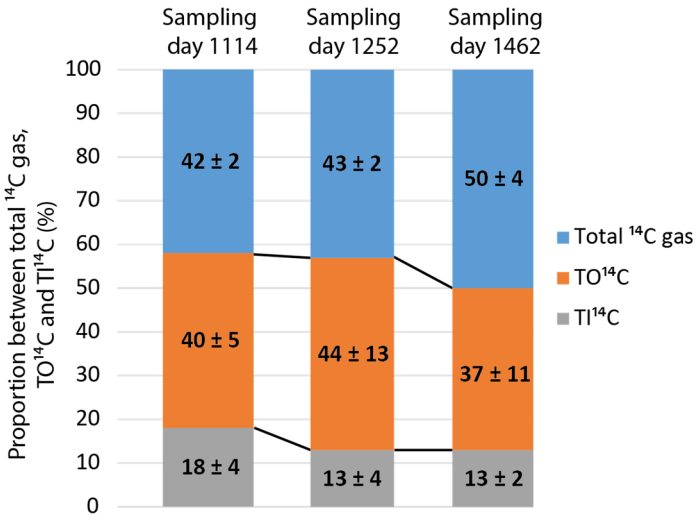

Fig. 5.3: Distribution of the ^{14}C-bearing compounds in the liquid and gas phases of the reactor after four and five years of alkaline anoxic corrosion of irradiated steel (samplings in 2019 and 2020).

We also performed CSRA of the solutions and gas phases sampled in 2019 and 2020. ^{14}C-carrying carboxylic acids (formic acid, acetic acid, malonic acid, oxalic acid and lactic acid) were found to be the main carbon compounds contributing ~ 50 % to the $TO^{14}C$. Carboxylic acids were already identified in solutions sampled before 2019 (Cvetković et al. 2018a). The $TO^{14}C$ portion that cannot be attributed to the ^{14}C-bearing carboxylic acids could be associated with ^{14}C-bearing organic colloids. Thanks to CSRA developed for the gas phase in the last two years (Guillemot et al. 2020a), we have been able to identify for the first time the ^{14}C-bearing HCs produced in the anoxic corrosion experiment with irradiated steel. Only two HCs were quantified in the gas phase of the reactor, $^{14}CH_4$ and $^{14}C_2H_6$. $^{14}CH_4$ was the most abundant one, corresponding to the total ^{14}C content in the gas phase within the uncertainty range, whereas the $^{14}C_2H_6$ concentration was found to be close to the detection limit of the analytical method (Guillemot et al. 2020a).

5.2.4 Rate of release of ^{14}C-bearing compounds during corrosion of irradiated steel

Time-dependent quantification of TO^{14}C and TG^{14}C enables a comparison with theoretical predictions of ^{14}C release made on the basis of corrosion rates for stainless steel. It is expected that the nuts were produced from one of the following alloys: X6CrNiTi18-10, X6CrNiNb18-10 or X6CrNiMoTi17-12-2, respectively. The corrosion of stainless steel in strongly alkaline conditions has extensively been investigated in the past. The corrosion rates for stainless steel in alkaline anoxic conditions are typically ≤ 10 nm/a (a: annum) (e.g. Diomidis 2014, Swanton et al. 2015). For the current predictions of ^{14}C release, it was assumed that the entire ^{14}C inventory of the irradiated steel nut specimens may either released into solution or gas phase. The ^{14}C activity of irradiated steel was determined to be 17.8 ± 2.5 kBq per gram of steel, which corresponds to a ^{14}C content of 0.107 ± 0.015 µg ^{14}C per gram of steel (Schumann et al. 2014). Predictions and experimental results are compared in Fig. 5.4.

During the first ~ 30 days of corrosion of irradiated steel, the ^{14}C release to solution in the organic chemical form (TO^{14}C) can be modelled on the assumption that a fast corrosion of 20 nm/a occurred (Fig. 5.4a). Afterwards, TO^{14}C was constant. Notably, TO^{14}C did not increase in accordance with the corrosion process (Fig. 5.4a). This observation led us to the aforementioned assumption that oxidised ^{14}C-carrying carbon compounds, mainly carboxylic acids, were released during the early step of corrosion and subsequently remained in solution. Note that the same assumption holds for ^{14}C-carrying carbonate. In contrast, the increase in total ^{14}C present in the gas phases can be modelled in accordance with the corrosion of irradiated steel at a rate of ~ 1 nm/a since the onset of corrosion in May 2016 (Fig. 5.4b). This statement actually highlights that ^{14}C-bearing HCs are continuously released during the course of corrosion, as previously observed with stable HCs in the corrosion studies with non-irradiated iron powders (Cvetković et al. 2018a; Guillemot et al. 2020b). In the light of these results, release rates for ^{14}C corrosion products to solution and gas phase can be estimated. While a fast release of ^{14}C occurred to solution during the first ~ 30 days (initial release), mimicked by a corrosion rate of 20 nm/a, homogenous corrosion of irradiated steel seems to proceed at a rate of ~ 1 nm/a. This rate is in accordance with corrosion rates reported for stainless steel in anoxic, strongly alkaline conditions (Diomidis 2014; Swanton et al. 2015).

Corrosion rates in anoxic conditions are usually determined from the time-dependent increase of the H_2 concentration based on the reaction: 3 Fe + 4 H_2O → Fe_3O_4 + 4 H_2 (*i.e.* Jelinek and Neufeld 1982). It was challenging to quantify H_2 in the corrosion experiment with irradiated steel because of its low molar mass, which is difficult to detect by GC-MS (Varlet et al. 2013). Nevertheless, it was possible to measure H_2 concentrations above the detection limit since the sampling at day 1114. The time-dependent release of H_2 can be modelled on the assumption of the corrosion of stainless steel at a rate of 10 nm/a. The latter rate corresponds to the upper bound of rates previously reported in the literature (e.g. Diomidis 2014) and further, it is a factor 10 higher than the corrosion rate estimated based on the gaseous ^{14}C concentration. This discrepancy can currently not be explained conclusively.

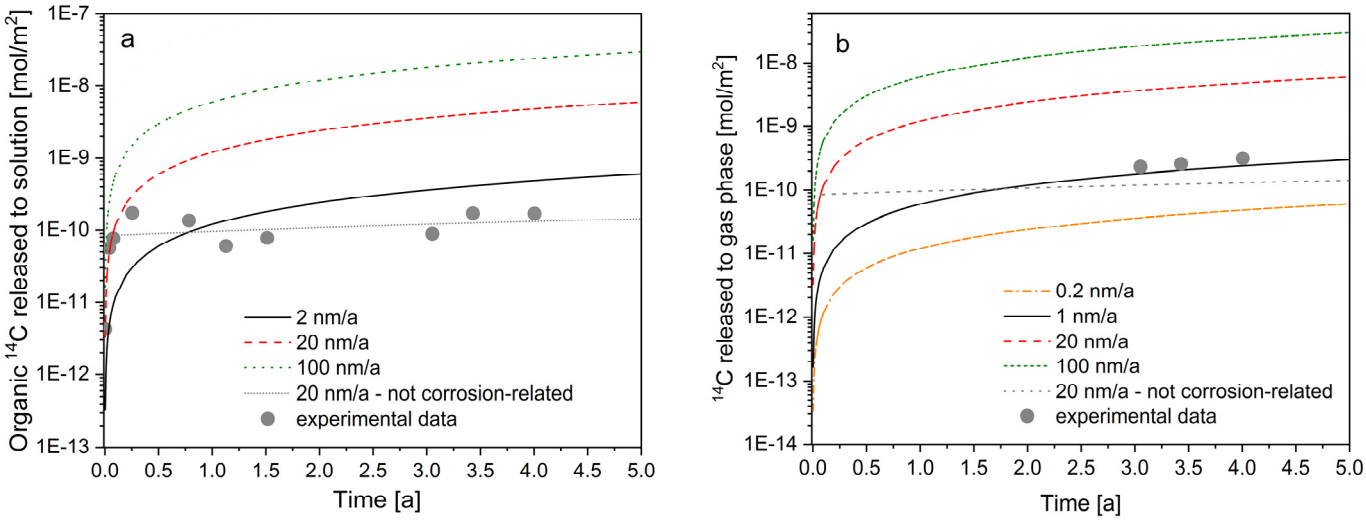

Fig. 5.4: Prediction of the time-dependent evolution of a) TO^{14}C in solution and b) TG^{14}C (gas phase) expressed in terms of surface normalised release as a function of corrosion rates (lines) and comparison with the experimental data.

5.2.5 Chemical stability of organic compounds in repository relevant conditions

It is expected that the anaerobic corrosion of irradiated steel in the near-field of a L/ILW radioactive waste repository will be accompanied by the release of significant quantities of ^{14}C-bearing low molecular weight (LMW) organic compounds such as ^{14}C-carrying formate and ^{14}C-carrying acetate (Wieland & Hummel 2015; Cvetković et al. 2018a). These LMW organic compounds are thermodynamically unstable and their oxidation to $^{14}CO_2$ or reduction to $^{14}CH_4$ would result in the undesired release of ^{14}C from the repository via the gas phase.

Under the moderate temperatures (< 65 °C) and pressures (< 80 bar) prevailing in the near-field of a cementitious repository (Nagra 2004; Kosakowski et al. 2014), these decomposition reactions proceed very slowly (Wieland & Hummel 2015) although some reactions may be accelerated by the presence of catalytic surfaces such as Fe(II,III) oxides on steel surfaces. There is limited literature available on the abiotic degradation of LMW organic compounds at temperatures below 100 °C. Most studies on degradation processes have been conducted under hydrothermal conditions (high temperature and pressure). Although the outcomes of such studies cannot be used directly to assess the long-term fate of LMW organic compounds in the cementitious near-field of an L/ILW repository where temperatures and pressures are much lower (see above, $T \leq 65$ °C, $P \leq 80$ bar), they may provide an insight into the nature and the kinetics of the reactions by which LMW organic compounds can decompose in the long-term.

The stability of formate in alkaline solutions was studied in air-tight reactors at different temperatures ($50\ °C \leq T \leq 200\ °C$) and pressures ($2\ bar \leq P \leq 16\ bar$) to explore whether the observations made on the degradation behaviour of LMW organic compounds under hydrothermal conditions are transferable to conditions relevant to a repository for radioactive waste. The results of these formate stability experiments have been described previously (LES progress reports 2018 and 2019). In brief, they confirmed that formate decomposition is very slow at ambient temperature while it is accelerated with increasing temperatures and in the presence of $Ca(OH)_2(s)$ and Fe powder. Significant formate decomposition followed by the production of carbonate was only observed at T > 120 °C. Increasing temperatures clearly enhance the rate of the decomposition reaction. It is further postulated that the presence of $Ca(OH)_2(s)$ accelerates formate decomposition by reaction with the decomposition product, carbonate, to form $CaCO_3(s)$. Decomposition rates derived from our experimental results at temperatures of 150 °C and 200 °C and pressures of 5.5 bar to 15.5 bar are similar to those observed in the literature under hydrothermal conditions ($175\ °C \leq T \leq 260\ °C$; P = 350 bar) (McCollom & Seewald 2003) reaching values of $k = 3.0 \cdot 10^{-7}\ s^{-1}$ in experiments oversaturated w.r.t. portlandite (Fig. 5.5a) and $k = 2.0 \cdot 10^{-8}\ s^{-1}$ in experiments undersaturated w.r.t. portlandite (Fig. 5.5b).

The outcomes of these experiments were compared with the results from thermodynamic carbon speciation calculations performed with the Gibbs Energy Minimization Selektor (GEMS) code. Seewald et al. (2006) reported that, under hydrothermal conditions, formate oxidation to CO_2 and reduction to formaldehyde (CH_2O) and methanol (CH_3OH) proceed quite fast. Further reduction to CH_4, however, is a very slow process. We assumed a similar kinetic behaviour in our experiments and, thus, in the present thermodynamic calculations, only formate oxidation to CO_2 and reduction to CH_2O and CH_3OH were allowed. Any further reduction reactions were blocked.

Fig. 5.6 shows the results of carbon speciation calculations at thermodynamic equilibrium as a function of temperature in the formate degradation experiments. In all cases, it is predicted that, at thermodynamic equilibrium, the large portion of formate is decomposed and only a very small fraction of the initial formate concentration is present. The major decomposition product is carbonate, thus confirming the observations from the experiments. In the presence of Ca, formate is even more destabilised (Figs. 5.6b and e) due to the precipitation of $CaCO_3(s)$ (Figs. 5.6c and f). Contact with the reactor steel surface (Figs. 5.6d, e and f) results in a lower redox potential due to iron corrosion and the formation of magnetite (Fig. 5.1f) resulting in a stabilisation of formate in solution (compare formate concentrations in Figs. 5.1d and e to those in Figs. 5.1a and b). This latter prediction made with the speciation calculations contradicts the experimental observations that suggest a catalytic effect in the presence of steel surfaces on the formate decomposition. The reason for this discrepancy is presently unknown. The detailed results of this study are described in a PSI Technical Report (Tits et al. 2019).

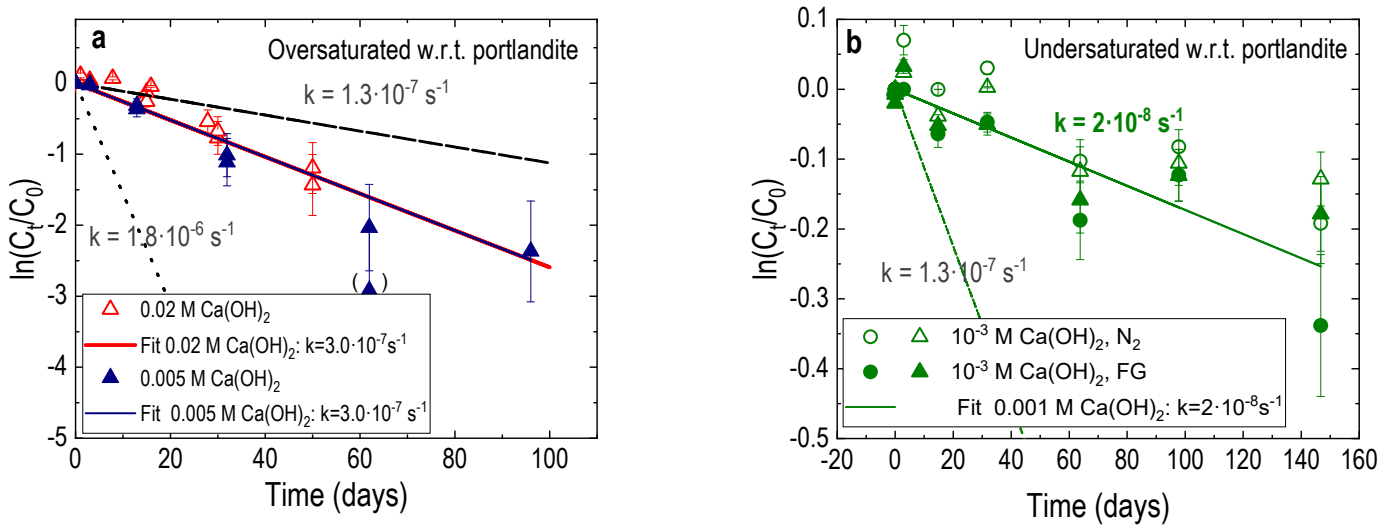

Fig. 5.5: Formate decomposition kinetics measured in Versoclave pressure reactors at 150 °C under saturated vapor pressure in contact with the stainless steel reactor wall in the systems a) oversaturated w.r.t. portlandite and b) undersaturated w.r.t. portlandite. Data are plotted as the natural logarithm of the ratio of the formate concentration at time, t, to the initial formate concentration (C_t/C_0) as a function of reaction time. Dashed and dotted lines represent 1st order kinetic behavior with decomposition rate constants determined by McCollom & Seewald (2003) in the presence of NiFe alloy ($k = 1.3 \cdot 10^{-7}$ s^{-1}) and in presence of a hematite+magnetite mixture ($1.8 \cdot 10^{-6}$ s^{-1}).

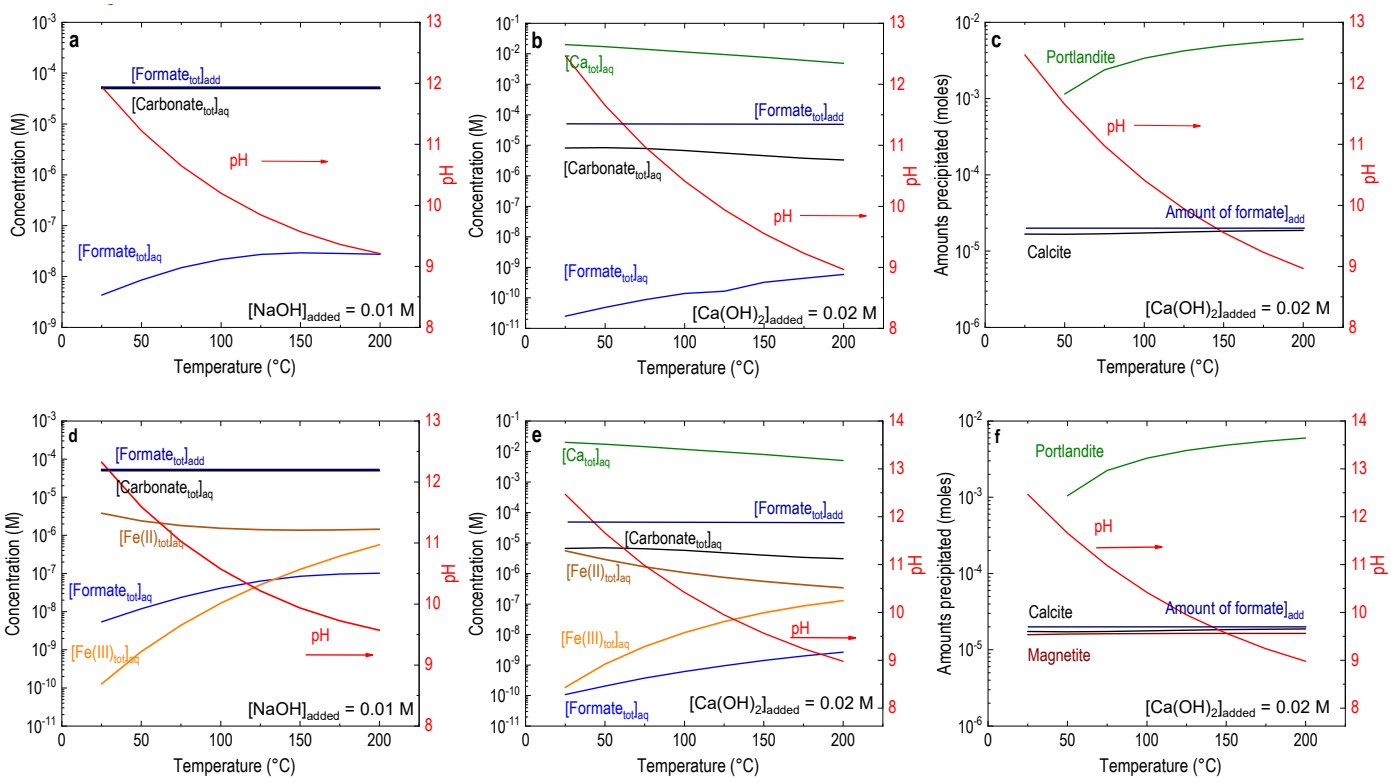

Fig. 5.6: Carbon speciation at thermodynamic equilibrium in alkaline formate solutions in a Versoclave reactor under N_2 atmosphere as a function of temperature in absence of metallic iron (Fe) (a, b, c) and in the presence of ~7 mg metallic iron due to corrosion of the reactor surface (d, e, f). $[Formate]_{tot} = 5 \cdot 10^{-5}$ M. Figs. a, b, d and e show aqueous concentrations. Figs. c and f show amounts of solid precipitated in the experiments. pH values are read on the right y axis.

5.3 DisCo Project

In the framework of the HORIZON 2020 EU project DisCo (Modern spent fuel Dissolution and chemistry in failed Container conditions) LES is responsible to develop thermodynamic models of UO_2 fuels under in-pile conditions. The objective is to assess whether or not dopants such as chromia (Cr_2O_3) could lead to higher oxygen potentials susceptible to oxidise UO_2 and redox-sensitive radionuclides in the fuel, leading to enhanced spent fuel dissolution and faster radionuclide release under repository conditions. Based on the results presented in the LES progress report 2019, it was concluded that no detrimental effects are to be expected. However, these results were based on a still incomplete thermodynamic model including, besides a number of stoichiometric solids, three solid solutions: a 19 end-member non-ideal UO_2 solid solution, an ideal binary $(Sr,Ba)ZrO_3$ phase and an ideal quinary noble metal (model '3 ss', see Table 5.2). In this contribution, we summarise the impact of model refinements and provide an analysis of the results in terms of temperature-dependent reactions.

Fig. 5.7 shows the equilibrium amounts of pure solids and solid solution end-members as a function of temperature, as calculated from the unrefined model. The corresponding oxygen potentials are shown in Fig. 5.8 as curve labelled '3 ss', along with other calculations discussed later. When Fig. 5.7 is analysed from left to right, reactions predicted to occur in the fuel with increasing in-pile temperature (*i.e.* from the pellet rim toward the pellet centre) can be identified (Table 5.3). They are evidenced by mirror-symmetrical amounts of reactants and products. Changes in dominant reactions are marked by sharp discontinuities (vertical dotted lines). All reactions except reaction 6 produce or consume $O_2(g)$ and may therefore influence the oxygen partial pressure (pO_2) and consequently the oxygen potential ($RT \ln pO_2$).

Up to 660 °C, pO_2 is controlled by the equilibrium between the Mo component in the ε-particle solid solution and pure $MoO_2(cr)$ (reaction 1). Between 660 °C and 780 °C a complex reaction involving formation of Ba molybdate, metallic Mo and zirconia takes over at the expense of Mo^{IV} oxide and Ba

Tab. 5.2: Solid solutions considered in the thermodynamic fuel model with corresponding lists of end-members.

UO_2 solid solution		**(Ba,Sr)-ZrO_3**	**ε-particle**	***Acronyms (Fig. 5.8)***
non-ideal		ideal	ideal	*3ss*
non-ideal		ideal	non-ideal	*3ss (non ideal ε)*
$(NpO_2)_2$	Ce_2O_3	$BaZrO_3$	Mo	
$(NpO_{2.5})_2$	$Cm^{III}U^{V}O_4$	$SrZrO_3$	Pd	
Am_2O_3	Cr_2O_3		Rh	
Cm_2O_3	$La^{III}U^{V}O_4$		Ru	
$(CeO_2)_2$	La_2O_3		Tc	
$(PuO_2)_2$	$Nd^{III}U^{V}O_4$			
$U^{IV}U^{V}O_{4.5}$	Nd_2O_3			
$(UO_2)_2$	$Pu^{III}U^{V}O_4$			
$Am^{III}U^{V}O_4$	Pu_2O_3			
$Ce^{III}U^{V}O_4$				

Tab. 5.3: Main reactions predicted across the temperature range 400 °C - 1400 °C in Cr-doped UO_2 fuel among stoichiometric solids (cr) solid solution end-members (ss) and gaseous species (g).

Reaction	**#**	**T /°C**
$Mo^0(ss) + O_2(g) \rightarrow Mo^{IV}O_2(cr)$	1	400-660
$2\ Mo^{IV}O_2(cr) + BaZrO_3(ss) \rightarrow 1/2\ O_2(g) + BaMo^{VI}O_4(cr) + Mo^0(ss) + ZrO_2(cr)$	2	660-780
$BaZrO_3(ss) + Mo^0(ss) + 3/2\ O_2(g) \leftrightarrow ZrO_2(cr) + BaMo^{VI}O_4(cr)$	3	780-1400
$2\ Ce^{III}U^{V}O_4(ss) + 1/4\ O_2(g) \rightarrow\ 2\ Ce^{IV}O_2(ss) + U^{IV}U^{V}O_{4.5}(ss)$	4	800-1250
$2\ U^{IV}O_2(ss) + 1/4\ O_2(g) \rightarrow U^{IV}U^{V}O_{4.5}(ss)$	5	1250-1400
$Ru^{IV}Te^{-II}2(cr) \rightarrow 2\ Ru^0(ss) + Te^0{}_2(g)$	6	840-1100
$Ce^{III}U^{V}O_4(ss) \rightarrow U^{IV}O_2(ss) + 1/2\ Ce^{III}{}_2O_3(ss) + 1/4\ O_2(g)$	7	1270 -1300

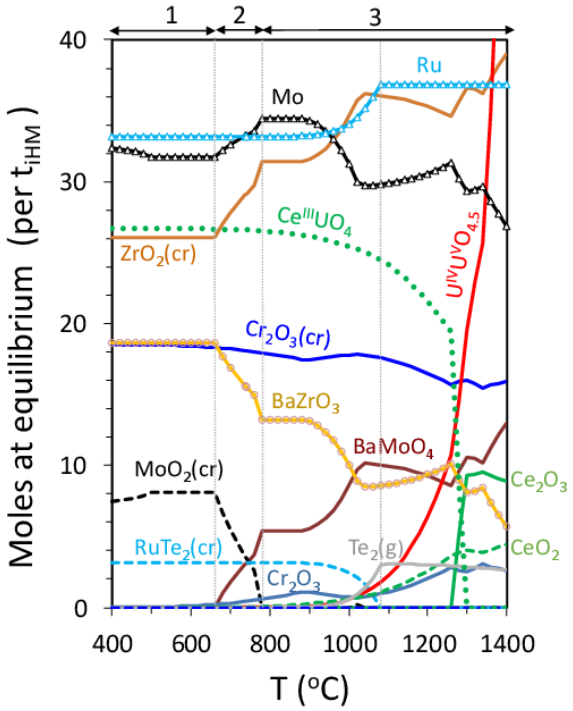

Fig. 5.7: Calculated equilibrium amounts of stoichiometric solids (cr) and solid solution end-members (without suffix) in one ton of Cr-doped fuel for the three solid solution model with ideal mixing in ε-particles (labelled "3ss" in Fig. 5.8). Numbered arrows correspond to reactions in Table 5.2.

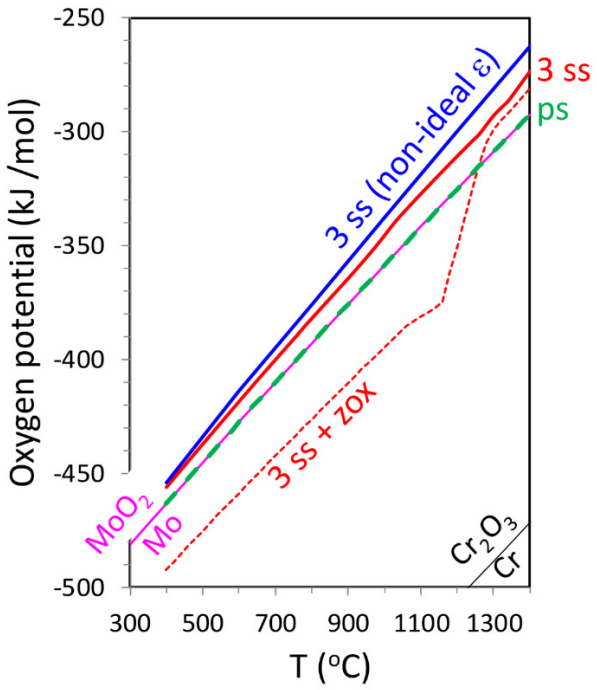

Fig. 5.8: Oxygen potential calculations for Cr-doped UO_2 fuel with 60 GW/t_{iHM} burnup and equilibrium lines for coexisting Mo-MoO_2 and Cr-Cr_2O_3 pure compounds.

zirconate (reaction 2). At T > 800 °C, pO_2 is controlled by the interplay of reactions 3, 4, 5 and 7, all involving one or more of the three solid solutions defined in the thermodynamic model. Equilibria 1, 2 and 3 buffer the oxygen potential up to about 1000 °C, illustrating the importance of molybdenum in controlling the oxidation state of the fuel.

Only at higher temperatures, the UO_2 solid solution starts to play a major role (reactions 4, 5 and 7). This is indicated by the steep increase of the $U^{IV}U^{V}O_{4.5}$ end-member at the expense of $Ce^{III}U^{V}O_4$, which is the predominant cerium end-member in UO_2 up to 1300 °C. The decrease of the $Ce^{III}U^{V}O_4$ mole fraction in the UO_2 phase correlates with the increase of $Ce^{III}_2O_3$ and $U^{IV}U^{V}O_{4.5}$ (reaction 7), occurring within a small temperature interval (1270 °C - 1300 °C). This reflects a change in U(IV) substitution mechanism within the UO_2 solid solution. The replacement of U^{4+} by Ce^{3+} with simultaneous oxidation of an U^{4+} neighbour to U^{5+} ($2\ U^{4+} \rightarrow Ce^{3+} + U^{5+}$) goes over to the substitution of two U^{4+} ions by a pair of Ce^{3+} with simultaneous formation of a vacancy (V_a) in the anionic sublattice ($2\ U^{4+} + O^{2-} \rightarrow 2\ Ce^{3+} + V_a$). In spite of the increase in $U^{IV}U^{V}O_{4.5}$ mole fraction, the UO_2 solid solution does not become hyperstoichiometric because of compensation by the (hypostoichiometric) $Ce^{III}_2O_3$ end-member. The calculated O/M ratios in the urania solid solution (where M includes U and all dissolved metals) remain therefore always very close to perfect stoichiometry (1.993 to 2.000), in agreement with the experimental findings of Matzke (1995).

Between 400 °C and 1400 °C, the speciation of chromium is dominated by Cr_2O_3(cr). Only a minor fraction of Cr^{III} remains as solid solution component in the UO_2 phase. This implies that most of the initially fully dissolved chromium is predicted to segregate from UO_2 during reactor operation.

The results shown in Fig. 5.7 refer to the oxygen potential curve labelled '3 ss' in Fig. 5.8, based on the thermodynamic model including an optimised multicomponent UO_2 solid solution, an ideal (Sr,Ba)ZrO_3 solid solution and an ideal five-component (Ru, Pd, Tc, Mo, Rh) solid solution representing the noble metal inclusions (ε-particles) found in high-burnup UO_2 fuel. An important and non-trivial part of the model refinement carried out during the last project year was to include non-ideality for this phase. This was achieved by transferring the model of Thompson et al. (2012) to the Berman-type solid solution model

used in our calculations. The curve labelled '3ss (non ideal ε)' shows that introducing non-ideal mixing in the ε-phase increases the calculated oxygen potentials by about 2 kJ/mol at 400 ºC up to 11 kJ/mol at 1400 ºC. This increase is however not sufficient to invalidate the former conclusion drawn from the results of the unrefined model (Curti & Kulik 2020), namely that Cr-doping will not lead to UO_2 or radionuclide oxidation.

The curve labelled 'ps' in Fig. 5.8 was computed by replacing the three solid solutions with simple stoichiometric solids (including pure UO_2). In this calculation pure Mo metal and pure MoO_2 are predicted to coexist at all temperatures, therefore constraining the fuel oxygen potential exactly along the corresponding buffer line.

Finally, the calculation labelled '3 ss + zox' shows the mitigating effect of Zircaloy oxidation on the calculated oxygen potential. This process was simulated by including in the GEM-Selektor input an amount of metallic Zr corresponding to the formation of a 10 μm thick ZrO_2 layer at the inner side of the cladding. The results indicate substantial oxygen potential reductions of up to 40-60 kJ/mol. Thus, to some extent the Zircaloy could act as buffer and protect the pellet-cladding interface against a local pO_2 increase, as recognized by Rondinella (2015).

5.4 References

Curti E., Kulik D.A. (2020)
Oxygen potential calculations for conventional and Cr-doped UO_2 fuels based on solid solution thermodynamics. Journal of Nuclear Materials 534, 152140.

Cvetković B.Z., Salazar G., Kunz D., Tits J., Szidat S., Wieland E. (2018a)
Quantification of dissolved organic ^{14}C-containing compounds by accelerator mass spectrometry in a corrosion experiment with irradiated steel. Radiocarbon 60, 1711-1727.

Cvetković B.Z., Salazar G., Kunz D., Szidat S., Wieland E. (2018b)
Analysis of ^{14}C-containing compounds released by corrosion of irradiated steel using accelerator mass spectrometry. Analyst 143, 3059-3067.

Cvetković B.Z, Rothardt J., Büttler A., Kunz D., Schlotterbeck G., Wieland E. (2018c)
Formation of low-molecular-weight organic compounds during anoxic corrosion of zero-valent iron. Environmental Engineering Science 35, 447-461.

Diomidis N. (2014)
Scientific basis for the production of gas due to corrosion in a deep geological repository. Nagra Work Report NAB 14-21.

Espic C., Liechti M., Battaglia M., Paul D., Röckmann T., Szidat S. (2019)
Compound-specific radiocarbon analysis of atmospheric methane: a new pre-concentration and purification set-up. Radiocarbon 61, 1461-1476.

Guillemot T., Salazar G., Cvetković B.Z., Kunz D., Szidat S., Wieland E. (2020a)
Determination of ultra-low concentrations of gaseous ^{14}C-bearing hydrocarbons produced during corrosion of irradiated steel using accelerator mass spectrometry. Analyst (accepted), doi: 10.1039/D0AN01517B.

Guillemot T., Cvetković B.Z., Kunz D., Wieland E. (2020b)
Processes leading to reduced and oxidised carbon compounds during corrosion of zero-valent iron in alkaline anoxic conditions. Chemosphere 250, 126230.

Jelinek J., Neufeld P. (1982)
Kinetics of hydrogen formation from mild steel in water under anaerobic conditions. Corrosion 38, 98-104.

Johnson L., Schwyn B. (2008)
Proceedings of a Nagra/RWMC workshop on the release and transport of C-14 in repository environments. Nagra Work Report NAB 08-22.

Kosakowski G., Berner U., Wieland E., Glaus M., Degueldre C. (2014)
Geochemical evolution of the L/ILW near-field. Nagra Technical Report NTB 14-11.

Matzke H.-J. (1995)
Oxygen potential measurements in high burnup LWR UO_2 fuel. Journal of Nuclear Materials 223, 1–5.

McCollom T.M., Seewald J.S. (2003)
Experimental constraints on the hydrothermal reactivity of organic acids and acid anions: I. Formic acid and formate. Geochimica Cosmochimica Acta 67, 3625 - 3644.

Nagra (2002)
Project Opalinus Clay - Safety Report. Demonstration of disposal feasibility for spent fuel, vitrified high-level waste and long-lived intermediate-level waste (Entsorgungsnachweis). Nagra Technical Report NTB 02-05.

Nagra (2004)
Effects of post-disposal gas generation in a repository for spent-fuel, high level waste and long-lived intermediate level waste sited in Opalinus Clay. Nagra Technical Report NTB 04-06.

Nuclear Decommissioning Authority (2012)
Geological disposal. Carbon-14 project - Phase 1 Report. Technical Report NDA/RWMD/092, Harwell Oxford, United Kingdom.

Rauber M. (2018)
Compound-specific radiocarbon analysis of aerosols, Master thesis, Faculty of Science. Bern, p. 80.

Rondinella V. (2015)
Oxygen potential of high burnup UO_2, American Nuclear Society Annual Meeting Proc. Vol. 112, 397–399.

Schumann D., Stowasser T., Volmert B., Günther-Leopold I., Linder H.-P., Wieland E. (2014)
Determination of the ^{14}C content in activated steel components from a neutron spallation source and a nuclear power plant. Analytical Chemistry 86, 5448-5454.

Seewald J.S., Zolotov M.Y., McCollom T.M. (2006)
Experimental investigation of single carbon compounds under hydrothermal conditions. Geochimica et Cosmochimica Acta 70, 446-460.

Swanton S.W., Baston G.M.N., Smart N.S. (2015)
Rates of steel corrosion and carbon-14 release from irradiated steels - state of the art review. CAST WP2 Deliverable 2.1, European Commission, Brussels.

Thompson W.T., Lewis B.J., Piro M.H., Corcoran E.C., Kaye M.H., Higgs J.D., Akbari F., Thompson D.M. (2012)
RMC Fuel Thermochemical Treatment, an online appendix to Lewis B.J., Thompson W.T., Iglesias F.C., Fission Product Chemistry in Oxide Fuels in: Konings R.J.M. (Eds.), Comprehensive Nuclear Materials, Elsevier, 2012.

Tits J., Miron D.G., Guillemot T., Kunz D., Laube A., Wieland E. (2019)
Experimental investigations on the stability of formate and acetate under cementitious near-field conditions. PSI Technical Report TM-44-19-21.

Varlet V., Smith F., Augsburger M. (2013)
Indirect hydrogen analysis by gas chromatography coupled to mass spectrometry (GC-MS). Journal of Mass Spectrometry 48, 914-918.

Wieland E., Hummel W. (2015)
Formation and stability of carbon-14 containing organic compounds in alkaline iron-water systems: Preliminary assessment based on a literature survey and thermodynamic modelling. Mineralogical Magazine 79, 1275-1286.

Wieland E., Cvetković B.Z. (2015)
Development of a compound-specific C-14 AMS technique for the detection of C-14 labelled organic compounds at very low concentrations. CAST WP2 Deliverable 2.19, European Commission, Brussels.

Wieland E., Cvetković B.Z., Kunz D., Salazar G., Szidat S. (2018)
Carbon-14 speciation during anoxic corrosion of activated steel in a repository environment. Atw - International Journal of Nuclear Power 63, 34-38.

6 THERMODYNAMIC MODELS AND DATABASES

Hummel W., Kulik D.A., Laube A., Miron G.D., Thoenen T., Tits J., Wieland E.

6.1 Introduction

The aim of this project is to develop thermodynamic models and databases to be applied in the preparation of various reports for the general license applications (RBG). Solubility and sorption databases and synthesis reports are an important part of the documentation for RBG. The carefully selected thermodynamic data provide the basis for defining pore water models, for the solubility databases, the development of the sorption databases and simulation of the repository *in situ* conditions. The consistent and consequent use of the approved thermodynamic dataset throughout all types of thermodynamic calculations is of crucial importance.

In the framework of the ThermAc project (2015-2020), supported by the German Federal Ministry of Education and Research (BMBF) a systematic evaluation of iso-coulombic reactions has been conducted to estimate the temperature dependence of lanthanide and actinide complexes in order to improve the chemical understanding and available thermodynamic data for these elements at elevated temperatures.

The cement sorption database has to be updated by the end of 2022 for use in safety assessments for RBG. In preparation for this report, an experimental study was launched in 2019 to determine the sorption values (R_d) for ^{26}Al, ^{32}Si and ^{45}Ca, safety-relevant radionuclides that had not been taken into account in previous sorption databases. This year, sorption kinetic studies with ^{45}Ca and ^{32}Si on C-S-H phases, portlandite and degraded hardened cement paste were completed. In addition, ^{45}Ca, ^{35}S and $^{14}CO_3^{2-}$ sorption studies on monocarbonate, hemicarbonate and on ettringite were launched.

In connection with the German project THEREDA (Thermodynamic Reference Database), presently funded by BGE (Bundesgesellschaft für Endlagerung), LES is in charge of maintaining the thermodynamic data for cement systems and was engaged this year in finalising the update of THEREDA by including the thermodynamic data of CEMDATA18 (Lothenbach et al. 2019) and in contributing to the preparations of the latest data release.

To support the thermodynamic calculations and management of thermodynamic databases, the GEM Software (GEMS) code collection has been developed at PSI/LES since 2000 by a community team lead by D. Kulik. The most recent application of GEMS focuses on the development of a new, flexible and extendable calcium aluminium silicate hydrate (CASH+) sublattice solid solution model describing well the stability, solubility, density, water content and mean silicate chain length of CASH phases – the main product of cement hydration.

6.2 Update of the Thermodynamic Data Base (TDB)

A high quality Thermodynamic Data Base (TDB) is currently in place. This database needs to be kept state-of-the-art and remaining gaps need to be filled where this is safety relevant. As the availability of an approved TDB is an essential prerequisite for defining pore water models and for preparing solubility limits and sorption database reports for the next safety assessments related to Nagra's general license applications (RBG). The TDB needs to be updated and existing gaps have to be filled before work on solubility and sorption databases commences. The development of the solubility and sorption databases is planned for 2021 – 2022. The current update of the TDB to "TDB 2020" has been planned for the period 2017 – 2020 with a final document to be published in 2021.

TDB 2020 includes reviews for the new elements Ac, Ag, Cd, Cf, Cu, Hg, Ho, Pa, Pb, Po, Sm, Ti and Zn, and updates of former data for Al, alkali (Li, Na, K) and alkaline earth elements (Mg, Ca, Sr, Ba), Eu, Fe, Mn, Mo, Nb, Pd, Ra, S, Se, silicates and Sn. The TDB revision has been finalised in 2020 with a review of selected organic ligands (Hummel 2020) and a review of alkali (Li, Na, K) and alkaline earth (Mg, Ca, Sr, Ba) phosphate compounds and complexes (Hummel & Curti 2020). Data for Fe have been updated this year according to the second volume of the NEA TDB on the Chemical Thermodynamics of Iron (Lemire et al. 2020). Last but not least, new and updated data from the NEA TDB Second Update on the Chemical Thermodynamics of Uranium, Neptunium, Plutonium, Americium and Technetium (Grenthe et al. 2020) have been included in TDB 2020.

A graphical representation of data considered in TDB 2020 is shown in Fig. 6.1. All data are made available as ready-to-use electronic database of the geochemical speciation code GEMS (http://gems.web.psi.ch/). An example of the electronic database as implemented

with the GUI module ThermoMatch for thermodynamic database management and consistency improvement (https://thermohub.org/thermomatch/thermomatch/) is shown in Fig. 6.2. A detailed documentation of the data sources will be published in 2021 as Nagra Technical Report (NTB).

6.2.1 Data selection for alkali and alkaline-earth phosphate compounds and complexes

Chemical thermodynamic data for alkali (Li, Na, K) and alkaline earth (Mg, Ca, Sr, Ba) phosphate compounds and complexes have not been considered in the previous versions of the data base (Pearson & Berner 1991; Pearson et al. 1992), and were also ignored in all later updates. However, this omission may lead to spurious results of model calculations for radioactive or chemical toxic contaminants involving phosphate. These concerns triggered a detailed review of published data for alkali and alkaline-earth phosphate compounds and complexes. The results of this review (Hummel & Curti 2020) have been included in TDB 2020. As an example, the solubility of apatite is discussed here.

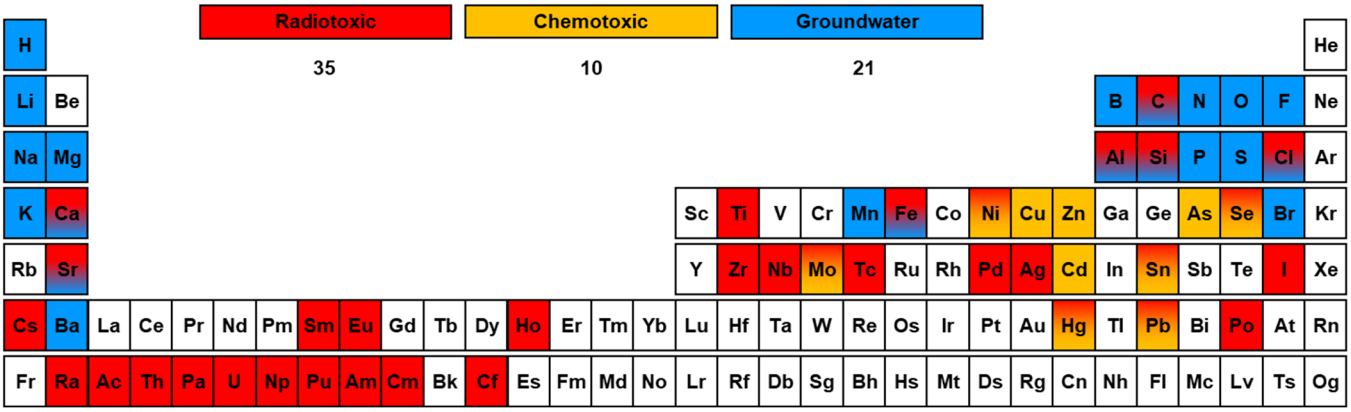

Fig. 6.1: Chemical elements considered in the PSI Chemical Thermodynamic Data Base 2020 (TDB 2020).

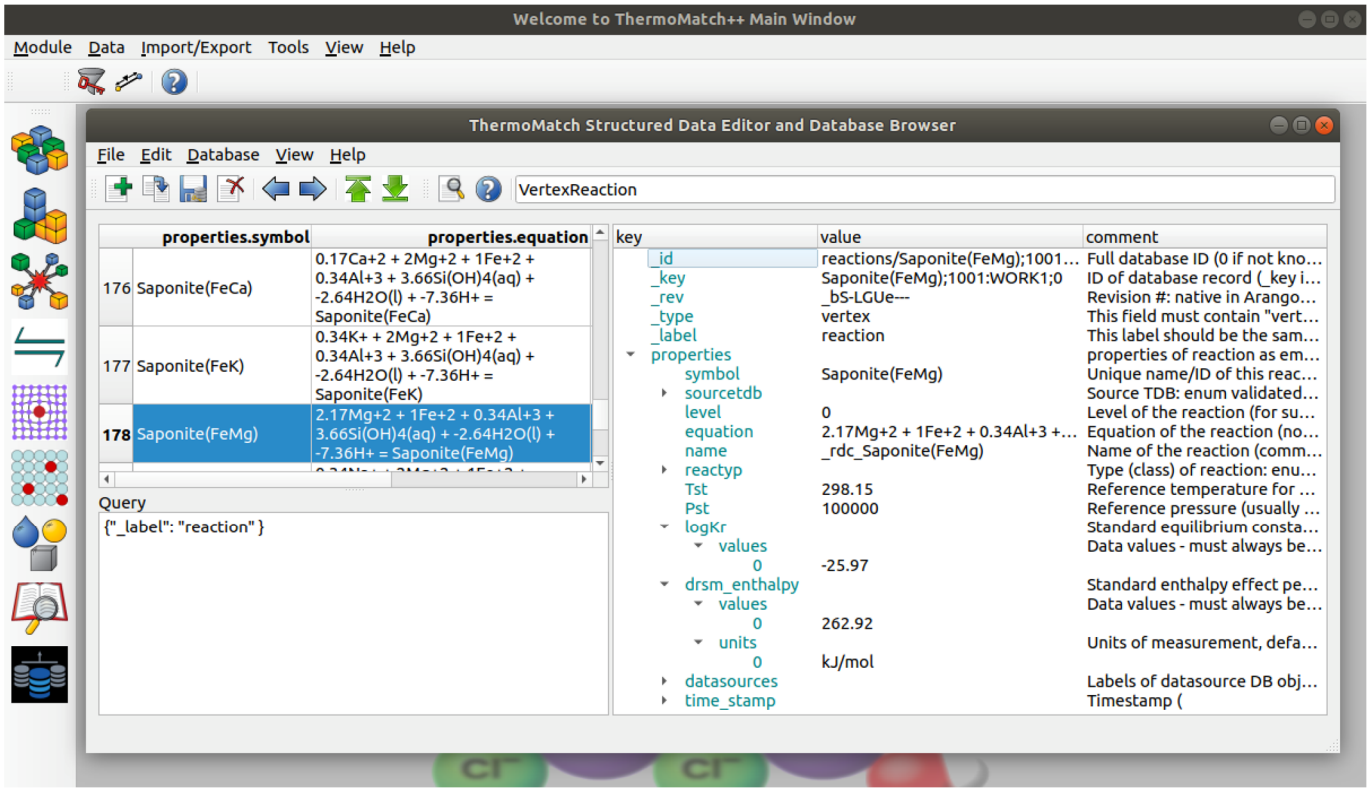

Fig. 6.2: An illustrative screenshot of a data information sheet in the electronic version of TDB 2020 as implemented with ThermoMatch.

Being the principal phosphorus phase in the earth's crust, apatite is of great industrial importance and of great interest to geochemists. Depending on the predominance of fluorine, chlorine or hydroxyl, the mineral is called fluorapatite, $Ca_5(PO_4)_3F(s)$, chlorapatite, $Ca_5(PO_4)_3Cl(s)$, or hydroxyapatite (also called hydroxylapatite), $Ca_5(PO_4)_3OH(s)$. Fluorapatite is the most abundant of the three endmembers. Pure hydroxyapatites and chlorine-bearing hydroxyapatites are common, but pure chlorapatites have not been observed in nature. Our review started by considering a synthesis of thermodynamic data for hydroxy- and fluorapatite published in 1968 by the group of I. L. Khodakovskiy (Valyashko et al. 1968). They accepted measured low-temperature heat capacity and entropy data of hydroxyapatite and fluorapatite, and were using solubility products at 25°C reported at that time, combined with entropy and enthalpy of formation data for aqueous species, to calculate the enthalpy of formation of hydroxyapatite and fluorapatite. We followed the approach of Valyashko et al. (1968), accepted the same measured low-temperature heat capacity and entropy data of hydroxyapatite and fluorapatite, but derived new solubility products at 25°C considering all published data, and used more recent entropy and enthalpy of formation data for aqueous species. As can be seen in Fig. 6.3, the experimental solubility data at other temperatures than 25°C of McDowell et al. (1971) for hydroxyapatite and

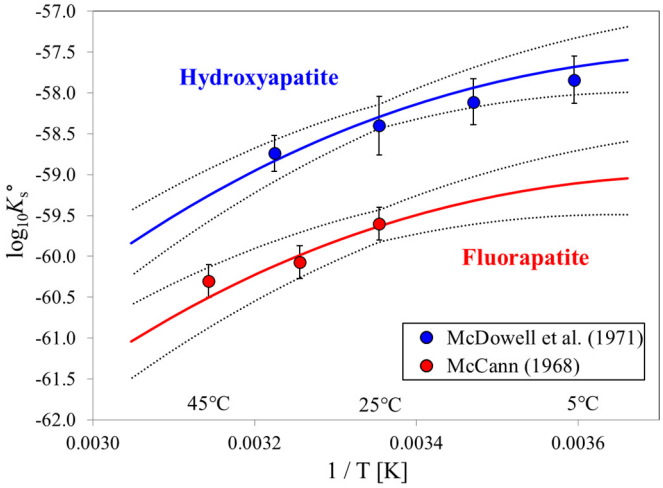

Fig. 6.3: The equilibrium constants $log_{10}K_s°$ for hydroxyapatite, $Ca_5(PO_4)_3OH(cr) \rightleftharpoons 5\ Ca^{2+} + 3\ PO_4^{3-} + OH^-$, and fluorapatite, $Ca_5(PO_4)_3F(cr) \rightleftharpoons 5\ Ca^{2+} + 3\ PO_4^{3-} + F^-$, as functions of temperature in the range 5 – 45°C. Solid lines: obtained from $log_{10}K_s°(298.15\ K)$, $\Delta_r H_m°(298.15\ K)$ and $\Delta_r C_{p,m}°(298.15\ K)$ values as derived by Hummel & Curti (2020). Dotted lines: lower and upper limits using the uncertainties of the above constants at 25°C and extrapolated to lower and higher temperatures.

McCann (1968) for fluorapatite, which have not been used in the derivation of the temperature functions of the apatites, are in good agreement with the calculated solubilities (lines in Fig. 6.3).

6.3 Systematic evaluation of isocoulombic reactions for estimating the temperature dependence of lanthanide and actinide complexes

Most of the available thermodynamic data on the stability of lanthanide and actinide complexes are restricted to values of reaction constants at 25 °C and 1 bar. While some new experimental data have become available, they are by far not sufficient to cover the large number of species of interest. Hence, theoretical estimation methods such as the isocoulombic reaction method still have to be used for covering the existing knowledge gaps. Isocoulombic reactions have the same number of like-charged species on the reactant and on the product side; in some cases, they can be used to accurately extrapolate the standard thermodynamic properties from low to elevated temperatures (Gu et al. 1994; Miron et al. 2020).

Several alternative isocoulombic reactions can be generated for the same set of chemical species, but not all provide the same degree of accuracy for temperature extrapolations. Ideally, "model reactions" (with well-known temperature dependence) are combined with the reactions of interest (with unknown temperature dependence) to generate isocoulombic reactions. To identify the optimal reactions that produce the best estimates, we systematically tested the isocoulombic method against available experimental data on the temperature dependence of aqueous complexation and solubility reactions of lanthanides and actinides. Using a new methodology (Fig. 6.4), streamlined using a dedicated database and efficient tools (https://thermohub.org/thermomatch/isoc/), we generated all possible alternative isocoulombic reactions and identified criteria for choosing the optimal ones.

Our results show that actinides and lanthanides ions having the ionic radius and solvation properties similar to the actinide or lanthanide of interest, can be used as analogues for setting the temperature dependence that, when combined into isocoulombic reactions, can be derived just from the $\log K°_{298}$ only (Fig. 6.5). Common dissolution and complexation reactions have large entropy and heat capacity effects (Gu et al. 1994; Miron et al. 2020). These effects cancel out in the case of a well-balanced isocoulombic reaction, which has on both sides (to the largest possible extent) ions with the same oxidation state, coordination number, and with similar ionic radii, hydration properties, and hydration shell structures of ionic species. Knowledge of $\log K°_{298}$

is sufficient to extrapolate the equilibrium constant of such a reaction to elevated temperatures. If accurate data on the temperature dependence of the model reaction is available, the isocoulombic method can be used to estimate $\log^{e}K^{\circ}_{T}$ of the reaction of interest with unknown temperature dependence (Fig. 6.5). This is of great importance for closing the existing gaps and thereby enhancing the applicability of thermodynamic calculations of chemical equilibria, until new experimental data on the temperature trends of complexation reactions become available.

To generate a suitable isocoulombic reaction and to use it for estimating the thermodynamic properties for reactions with unknown temperature dependence, a three-step methodology is recommended (Miron et al. 2020): Step 1: use similarities between reactants (hydrated ionic radius, structure of the hydration shell, and solvation properties) in search for a suitable model reaction to construct an isocoulombic reaction; Step 2: extrapolate $\log^{i}K^{\circ}_{T}$ of the isocoulombic reaction to elevated temperatures; and Step 3: estimate $\log^{e}K^{\circ}_{T}$ of the reaction of interest as a function of temperature from the extrapolated $\log^{i}K^{\circ}_{T}$ values and the known $\log^{m}K^{\circ}_{T}$ values at elevated temperature of the model reaction.

This work was part of the ThermAc project (2015-2020), supported by the German Federal Ministry of Education and Research. The goal of the project was to extend the chemical understanding and available thermodynamic data for actinides to elevated temperatures, using a combination of experiments, estimation methods, and quantum chemical calculations.

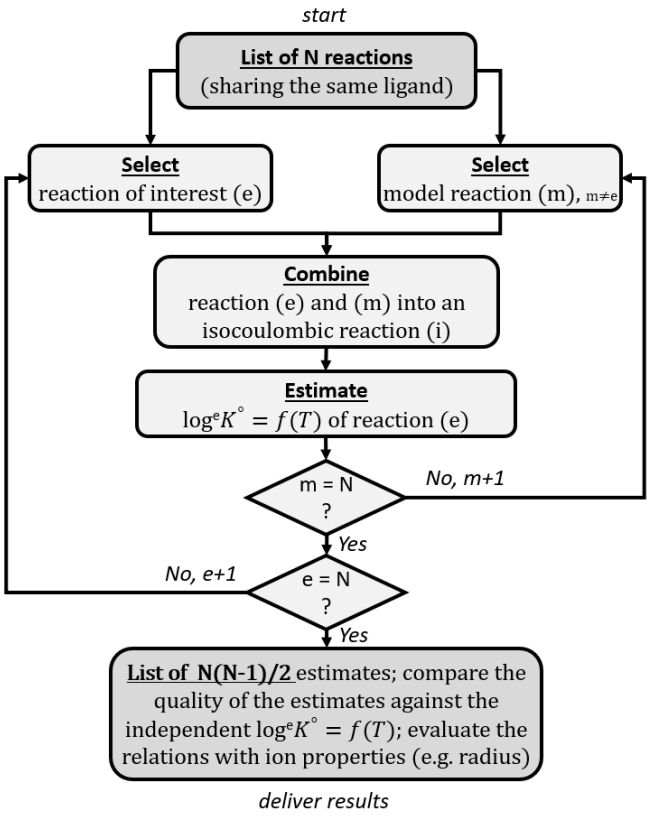

Fig. 6.4: Flow-chart for the systematic evaluation of $\log K^{\circ}_{T}$ temperature trends by generating all possible isocoulombic combinations from a list of selected reactions, and quality-testing of the $\log^{e}K^{\circ}_{T}$ estimates (Miron et al. 2020).

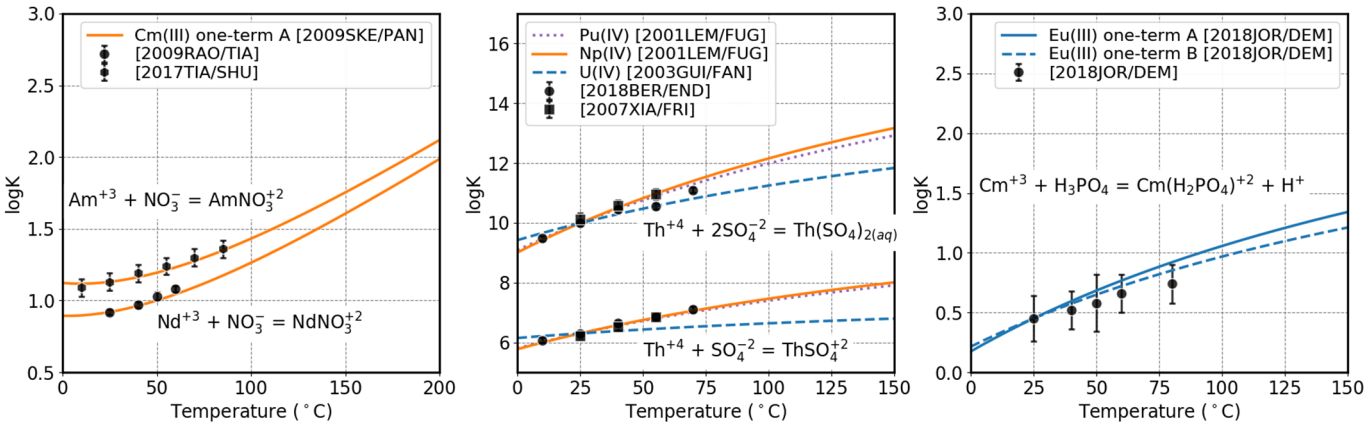

Fig. 6.5: Experimental data (symbols) compared with estimated $\log K^{\circ}_{T}$ (lines) for the displayed reactions using isocoulombic reactions constructed with analogue model reactions of the elements in the legend. Experimental data (Di Bernardo et al. 2018; Jordan et al. 2018; Rao and Tian 2009; Tian and Shuh 2014; Xia et al. 2007) and data for model reactions from (Guillaumont et al. 2003; Jordan et al. 2018; Lemire et al. 2001; Skerencak et al. 2009).

6.4 Supplementary sorption data for the update of the cement sorption database

A new update of the cement sorption database has to be developed by the end of 2022 for use in safety assessments in SGT-E3. In preparation for this report, an experimental study was launched in 2019 to determine the sorption values (R_d) for selected safety-relevant radionuclides that had not been taken into account in previous sorption databases. These include ^{26}Al, ^{32}Si and ^{45}Ca. The approach used to assess the sorption behaviour of these radionuclides is based upon the hypothesis that their retention by cementitious materials is controlled by isotopic exchange with stable Al, Si and Ca during recrystallization of the main cement minerals, such as C-(A)-S-H phases (Ca, Si, Al), portlandite (Ca), ettringite (Ca, Al) and AFm phases (Ca, Al). To confirm this hypothesis, the sorption of ^{32}Si and ^{45}Ca, ^{35}S, and $^{14}CO_3^{2-}$ on the above-mentioned cement minerals is investigated as function of time in batch sorption experiments. The observed kinetic sorption behaviour will reveal whether or not the uptake is controlled by isotope exchange and recrystallization processes. Sorption experiments with ^{26}Al are not planned because this radionuclide is very rare and cannot be purchased. R_d values for ^{26}Al in the sorption database will be estimated by assuming that the isotopic exchange behaviour with stable Al in ettringite (SO_4-AFt) and AFm phases (monocarbonate: CO_3-AFm; hemicarbonate: $OHCO_3$-AFm) is identical to that of ^{45}Ca, $^{14}CO_3$ and ^{35}S. Isotopic exchange of the latter radioisotopes can be determined experimentally.

In 2020, sorption kinetic studies with ^{45}Ca and ^{32}Si on C-S-H phases, portlandite and degraded hardened cement paste started the year before, were completed. In addition, ^{45}Ca, ^{35}S and $^{14}CO_3^{2-}$ sorption studies on monocarbonate, hemicarbonate and on ettringite were launched. These experiments have been rescheduled to cope with the COVID-19 pandemic, meaning that the last samplings of these kinetic tests will be completed in 2021.

R_d values for ^{45}Ca and ^{32}Si sorption onto C-S-H phases increased slowly over the entire duration of the experiments (>1 year) without reaching a plateau value although the increase in the case of ^{32}Si is less clear (Fig. 6.6a). Such a sorption behaviour suggests that the uptake controlling process may be recrystallization. A detailed analysis of the sorption kinetics is underway. ^{45}Ca sorption kinetic tests on portlandite using different S:L ratios show a similar kinetic behaviour as on C-S-H phases suggesting that the ^{45}Ca sorption on this mineral is also controlled by a recrystallization process (Fig. 6.6c). The small effect of the S:L ratio visible in Figure 6.6b is probably accidental as it only occurs in the last two measurements and this effect falls within the uncertainty of the data. ^{45}Ca, $^{14}CO_3^{2-}$ and ^{35}S sorption kinetic tests onto CO_3-AFm, $OHCO_3$-AFm and ettringite are still ongoing (Figs. 6.6d, 6.6e and 6.6f). R_d values for these three radionuclides onto AFm phases are increasing slowly with time in a similar way as observed for ^{45}Ca and ^{32}Si uptake by C-S-H phases and portlandite. Only the sorption of ^{14}C on $OHCO_3$-AFm shows an abnormal behaviour and seems to decrease as a function of time (Fig. 6.6e). The reason for this anomalous behaviour is presently not clear and additional data are awaited for final interpretation of the experimental results.

Chemical analysis of the equilibrium solutions at the end of the experiments and the mass balances derived from them allow to calculate theoretical equilibrium R_d values for ^{45}Ca and ^{32}Si ($R_d^{Ca}(eq)$, $R_d^{Si}(eq)$) assuming that homogeneous recrystallization (homogeneous distribution of ^{45}Ca and ^{32}Si in the solid and the aqueous phase) of the solid phases is the dominant sorption process:

$$R_d^{Ca}(eq) = \frac{Ca_{CSH}}{[Ca]_{eq}} \qquad R_d^{Si}(eq) = \frac{Si_{CSH}}{[Si]_{eq}} \quad (L\ kg^{-1})$$

Ca_{CSH} and Si_{CSH} are the amount of Ca and Si in the C-S-H solid phase (mol kg^{-1}) and $[Ca]_{eq}$ and $[Si]_{eq}$, the aqueous Ca and Si concentrations at equilibrium (M). These theoretical R_d values are in all cases higher than the values obtained from the experimental sorption tests and the trends in all sorption kinetics experiments tend towards the theoretical $R_d(eq)$ value in the long-term (thick horizontal lines in Figs. 6.6a, 6.6b and 6.6c). A recrystallization process also explains the effect of the C-S-H composition ($CaO:SiO_2$ or C:S ratio) on ^{45}Ca and ^{32}Si R_d values: R_d values mainly depend on $[Ca]_{eq}$ and $[Si]_{eq}$ which change by a factor of 20 for Ca increasing from $[Ca]_{eq} \sim 10^{-3}$ M at C:S = 0.7 to $[Ca]_{eq} \sim 2 \cdot 10^{-2}$ M at C:S = 1.65 and a factor of ~300 for Si decreasing from $[Si]_{eq} \sim 3 \cdot 10^{-3}$ M at C:S = 0.7 to $[Si]_{eq} \sim 10^{-5}$ M at C:S = 1.65 whereas the amounts of Ca and Si in the solid only vary by a factor of ~1.5.

For portlandite the theoretical equilibrium R_d value for ^{45}Ca sorption assuming homogeneous recrystallization was calculated to be 620 L kg^{-1}. This value is very similar to the theoretical R_d value obtained for C-S-H phases with a C:S ratio of 1.7 suggesting that portlandite may be an important sink as well for ^{45}Ca in HCP.

For the AFm phases and ettringite, theoretical equilibrium R_d values could not be calculated yet because measurements of the equilibrium solution compositions are still underway.

^{45}Ca and ^{32}Si sorption behaviour onto degraded hardened cement paste (HCP) is very similar to that onto pure cement phases (Figs. 6.6g and 6.6h): R_d values increase steadily with increasing reaction time without reaching a plateau value. ^{45}Ca R_d values are of the same order of magnitude as those found onto C-S-H phases with high C:S ratios and portlandite and also ^{32}Si R_d values are similar to those found on C-S-H phases with C:S = 1.7. The ^{32}Si R_d values measured on HCP are significantly higher than the ^{45}Ca R_d values.

These observations are a strong indication that the sorption of these two radionuclides on degraded HCP is controlled by recrystallization of the C-S-H fraction or portlandite.

In a next step, it will be tested whether a homogeneous or a heterogeneous recrystallization model best describes the experimental sorption measurements.

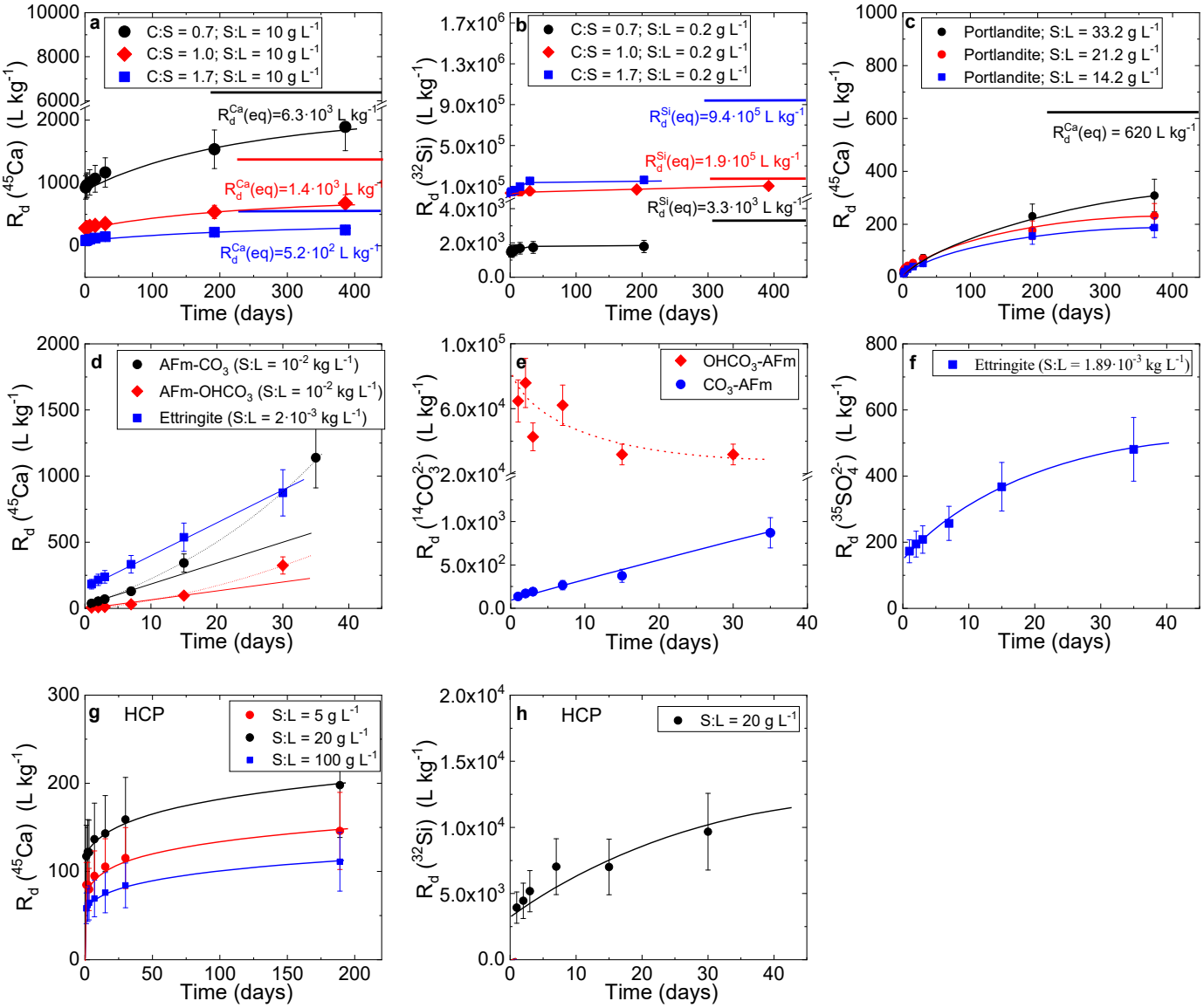

Fig. 6.6: ^{45}Ca, ^{32}Si, ^{35}S and $^{14}CO_3^{2-}$ sorption kinetics on different cement phases and degraded HCP. a) ^{45}Ca sorption on C-S-H phases with varying C:S ratios. b) ^{32}Si sorption on C-S-H phases with varying C:S ratios. c) ^{45}Ca sorption on portlandite. d) ^{45}Ca sorption onto CO_3-AFm, $OHCO_3$-AFm and ettringite. e) $^{14}CO_3^{2-}$ sorption on CO_3-AFm and $OHCO_3$-AFm. f) $^{35}SO_4$-sorption onto ettringite. g and h) ^{45}Ca and ^{32}Si sorption on degraded HCP. Lines through the experimental points were drawn to guide the eye. Thick horizontal lines in Figs. a, b and c. represent theoretical equilibrium R_d values assuming complete homogeneous recrystallization.

6.5 Initial estimation of standard thermodynamic properties of CASH+ solid solution end members

In a collaborative SNSF project "CASH-2", we developed a new, flexible and extendable CASH+ sublattice solid solution model, consistent with the C-S-H defect-tobermorite structure, and describing well the stability, solubility, density, water content and mean silicate chain length (MCL) of C-S-H phases – the main product of cement hydration. The CASH+ model considers simultaneous substitutions of chemical moieties in BT (bridging tetrahedral silicate chain) and IC (interlayer cation exchange) sublattices, *i.e.* sets of structurally equivalent sites. All possible solid solution end members (at least 20) were generated by permutating the moieties on their respective sublattices. Most of the end members do not exist as pure mineral substances, hence, their standard thermodynamic properties cannot be directly obtained. However, to start parameter optimization of CASH+ model, the initial standard Gibbs energy per mole G^*_{298} values of end members must lie within a ±50 kJ/mol (~1%) uncertainty interval. Besides, the model must reproduce temperature trends and known values of density d, enthalpy H and heat capacity Cp of C-S-H phases. For that, we used a systematic approach for consistent prediction of standard molar volume V°_{298}, absolute entropy S^*_{298}, heat capacity Cp^*_{298}, and enthalpy H^*_{298} values for all CASH+ end members in the system Ca-Si-K-Na-Al-Fe-Si-H_2O with uncertainty of 10% for S°_{298} and 30% for Cp°_{298} estimates.

Recent literature data suggest the solid density $d = 2.5$ g/cm^3 for C-S-H with molar Ca/Si < 0.75, while for C-S-H with Ca/Si > 0.99, $d = 2.7$ g/cm^3 can be set, with 0.1 g/cm^3 uncertainty. Accurate V°_{298} values (obtained from densities) can be used for predicting S°_{298} and Cp°_{298} values of substances from VBT (volume-based thermodynamics) equations ((Glasser & Jenkins 2016) and refs. therein). Absolute S°_{298} values can be estimated (see also Ghazizadeh et al. 2020) from the formula unit volume $V_m = {10^{21} \cdot V^\circ_{298}}/{N_A}$ in nm^3 ($N_A = 6.022 \cdot 10^{23}$ is the Avogadro's number and V°_{298} is in cm^3/mol), and the empirical constants k and c :

$$S^\circ_{298} = V_m k + c \quad \text{(in J/K/mol)} \qquad (1)$$

For hydrated ionic salts (including C-S-H), $k = 1579 \pm 30$ and $c = 6 \pm 6$, with S°_{298} uncertainty of $\pm$7.4 J/K/mol ((Glasser and Jenkins 2016), Table 2). A similar, but less accurate equation exists for the standard heat capacity:

$$Cp^\circ_{298} = V_m k' + c' \quad \text{(in J/K/mol)} \qquad (2)$$

C-S-H is a non-framework silicate, hence $k' = 1465$ and $c' = 11$ ((Glasser & Jenkins 2016), Table 2). The uncertainty of such Cp°_{298} estimate is given by the authors as 25% of the value. Therefore, we decided to compare it with other simple predictions, for instance the Dulong-Petit limit for the high-temperature heat capacity:

$$Cp^\circ_{298} = \mathrm{m} \cdot 3R = \mathrm{m} \cdot 25 \text{ (in J/K/mol)} \qquad (3)$$

where $R = 8.31451$ (J/K/mol) is the universal gas constant, and m is the number of atoms in the formula. We found the Dulong-Petit limit values from eq (3) too high, up to 200 J/K/mol above those obtained from eq (2). Next, we tried the modified Kopp rule (Hurst and Harrison 1992) that estimates Cp°_{298} value of a condensed substance as

$$Cp^\circ_{298} = \sum_i \mathrm{m}_i Cp_i \qquad \text{(in J/K/mol)} \qquad (4)$$

where m_i is the number of *i*-th element atoms in the substance formula, and Cp_i is the contribution per mole of *i*-th element (regressed from known heat capacities). Contributions for elements involved in C-S-H are: H: 7.56; O: 13.42; Si: 17.00; Ca: 28.25; K: 28.78; Na: 26.19; Al: 18.07; Fe: 29.08 (all in J/K/mol, from (Hurst & Harrison 1992) Table 1). Values of Cp°_{298} from eq (4) are similar to the respective values obtained from eq (2). Hence, we decided to use Cp°_{298} estimates from eq (2) as acceptable with 30% uncertainty. The obtained dataset of densities, V°_{298} and VBT-estimated S°_{298} and Cp°_{298} values for C-S-H end members is provided in Tab. 6.1.

Initial G^*_{298} estimates for CASH+ end members were obtained from isocoulombic or isoelectric reactions with $\Delta_r G^*_{298} = 0$, involving the T5C, T2C and TobH end member analogues from our previous CSH3T model ((Kulik 2011), Tables 7,8).

To obtain G^*_{298} estimates for Na, K and Al-containing end members, the reaction-estimated ("re") values using exchange reactions (with $\Delta_r G^*_{298} = 0$) were found inappropriate because there were no end member analogues. Instead, we used a simple method of polyhedral contributions ("pc") (Chermak & Rimstidt 1989) for estimating G^*_{298} and H^*_{298} values of minerals in the system Al-Si-Ca-Mg-Fe-Na-K-O-H.

Tab. 6.1: Estimates of standard molar volumes, absolute entropies and heat capacities of CASH+ core model end members at T=25 °C (298.15 K), P = 1 bar (0.1 MPa).

Name	Bulk formula	d g/cm^3	V°_{298} cm^3/mol	V_m nm^3/fun	S°_{298} J/K/mol	Cp°_{298} J/K/mol	Cp°_{298} m.K.	ΔCp°_{298} VBT-m.K.
TSvh	$Ca_2Si_3O_{11}H_6$	2.5	138.6	0.2301	369.4	348.1	300.5	47.6
TSCh	$Ca_3Si_3O_{13}H_8$	2.7	155.8	0.2586	414.4	389.9	370.7	19.2
Tvvh	$Ca_2Si_2O_9H_6$	2.7	106.1	0.1761	284.1	269.0	256.6	12.4
TCvh	$Ca_3Si_2O_{10}H_6$	2.7	126.8	0.2106	338.6	319.6	298.3	21.3
TvCh	$Ca_3Si_2O_{11}H_8$	2.7	133.5	0.2217	356.1	335.8	326.9	8.90
TCCh	$Ca_4Si_2O_{12}H_8$	2.7	154.3	0.2562	410.5	386.3	368.5	17.8
TSNh	$Ca_2Na_1Si_3O_{12}H_7$	2.5	143.1	0.2377	381.3	359.2	347.7	11.5
TvNh	$Ca_2Na_1Si_2O_{10}H_7$	2.7	120.9	0.2007	322.9	305.1	303.8	1.3
TCNh	$Ca_3Na_1Si_2O_{11}H_7$	2.7	141.6	0.2352	377.4	355.6	345.5	10.1
TSKh	$Ca_2K_1Si_3O_{12}H_7$	2.5	149.1	0.2476	396.9	373.7	350.2	23.5
TvKh	$Ca_2K_1Si_2O_{10}H_7$	2.7	126.8	0.2106	338.6	319.6	306.4	13.2
TCKh	$Ca_3K_1Si_2O_{11}H_7$	2.7	147.6	0.2451	393.0	370.1	348.1	22.0
TAvh	$Ca_2Al_1Si_2O_{12}H_9$	2.5	135.0	0.2241	359.9	339.3	337.7	1.6
TACh	$Ca_3Al_1Si_2O_{14}H_{11}$	2.7	162.4	0.2697	431.8	406.1	407.9	-1.8
TANh	$Ca_2Al_1Na_1Si_2O_{13}H_{10}$	2.5	149.8	0.2487	398.7	375.3	384.8	-9.5
TAKh	$Ca_2Al_1K_1Si_2O_{13}H_{10}$	2.5	155.7	0.2586	414.3	389.9	387.4	2.5
TSFh	$Ca_2Fe_1Si_3O_{13}H_7$	2.6	174.4	0.2895	463.2	435.2	392.5	42.7
TCFh	$Ca_3Fe_1Si_2O_{12}H_7$	2.8	160.5	0.2665	426.8	401.4	390.3	11.1
TvFh	$Ca_2Fe_1Si_2O_{11}H_7$	2.8	140.4	0.2332	374.2	352.7	335.2	17.4
TAFh	$Ca_2Al_1Fe_1Si_2O_{14}H_{10}$	2.8	168.3	0.2795	447.3	420.4	429.7	-9.2

Density d with $\pm$ 4% (0.1 g/cm^3) uncertainty. S°_{298} calculated from VBT eq (1), $\pm$ 10%. Cp°_{298} obtained from VBT eq (2), $\pm$ 30%. "fun" stands for the formula unit; "m.K." for the modified Kopp method (eq 4); "VBT-m.K" means the difference of values obtained using the VBT equation (2) and the modified Kopp equation (4). Details about CASH+ model setup, end member names nomenclature, end member generation can be found in (Kulik et al. 2020, submitted manuscript).

The contributions g_i to Gibbs energy and h_i to standard enthalpy (at 25 °C, 1 bar) from polyhedral units like octahedral $^{(6)}Al(OH)_3$, tetrahedral $^{(4)}SiO_2$, H_2O, etc. ((Chermak & Rimstidt 1989) Table 2), allow the following estimates with uncertainties from 4.6 to 35.6 kJ/mol:

$$G^*_{298} = \sum_i n_i g_i \quad (5)$$

$$H^*_{298} = \sum_i n_i h_i \quad (6)$$

where n_i is the number of moles of i-th polyhedral component per mole of the mineral.

Table 6.2 compares G^*_{298} and H^*_{298} "pc" estimates (5), (6) with "re" values. The "pc" values of G^*_{298} and H^*_{298} deviate less than 50 kJ/mol or 1% of the value from the "re" values. Estimated H^*_{298}(pc) values are also consistent with H^*_{298}(re) values computed from G^*_{298}(re) values (Table 6.2) and VBT-estimated S°_{298} values (Table 6.1). The differences $\Delta H^*_{298} = H^*_{298}$(pc) - H^*_{298}(re) lie within -8.2 and 41.0 kJ/mol, or within 1% uncertainty.

Therefore, combining VBT, polyhedral contributions and isocoulombic reaction methods, one can obtain fairly consistent initial estimates of all standard molar properties for CASH+ sub-system end members. To some extent, this conclusion is validated in Fig. 6.7, where the C-S-H solubility is predicted using G°_{298} values fitted at room temperature, and S°_{298}, Cp°_{298} values from Tab. 6.2. of CASH+ core model end members, without any further adjustment to the experimental data at elevated temperatures.

Tab. 6.2: Initial estimates of G^*_{298} and H^*_{298} of Ca-Si-H_2O end members of the CASH+ model at T=25 °C (298.15 K), P = 1 bar (0.1 MPa).

Name	G^*_{298} from reaction	G^*_{298}(re) kJ/mol	G^*_{298}(pc) kJ/mol	ΔG^*_{298} pc-re	H^*_{298}(re) J/K/mol	H^*_{298}(pc) J/K/mol	ΔH^*_{298} pc-re
TSvh	2TobH = TSvh + $2H_2O$	**-4648.70**	-4619.84	28.86	-5033.47	-5003.32	30.15
TSCh	2.4T5C = TSCh + $2H_2O$	**-5570.42**	-5569.83	0.59	-6054.30	-6031.73	22.57
Tvvh	TSvh = Tvvh + $SiO_{2(am)}$	**-3770.93**	-3765.89	5.04	-4114.37	-4092.35	22.02
TCvh	2T2C = TCvh + $2H_2O$	**-4459.85**	-4435.02	24.83	-4830.02	-4789.00	41.02
TvCh	TCvh + H_2O = TvCh	**-4688.16**	-4715.88	-27.72	-5122.65	-5120.76	1.89
TCCh	TCvh + $Ca(OH)_{2(cr)}$ = TCCh	**-5347.99**	-5385.01	-37.02	-5809.24	-5817.41	-8.17

Standard properties of $Ca(OH)_{2(cr)}$ and $SiO_{2(am)}$ taken from PSI/Nagra 12/07 and Cemdata 18 databases, respectively. Standard properties of liquid H_2O taken from Wagman et al. (1982). The values of G^*_{298}(re) calculated from indicated reactions with $\Delta_r G^*_{298} = 0$. The value of H^*_{298}(re) calculated from G^*_{298}(re) and S°_{298} VBT-predicted value given in Table 6.1. G^*_{298}(pc) from eq (5), H^*_{298}(pc) from eq (6). The G^*_{298} values taken as initial for the GEMSFITS parameterization are shown in boldface.

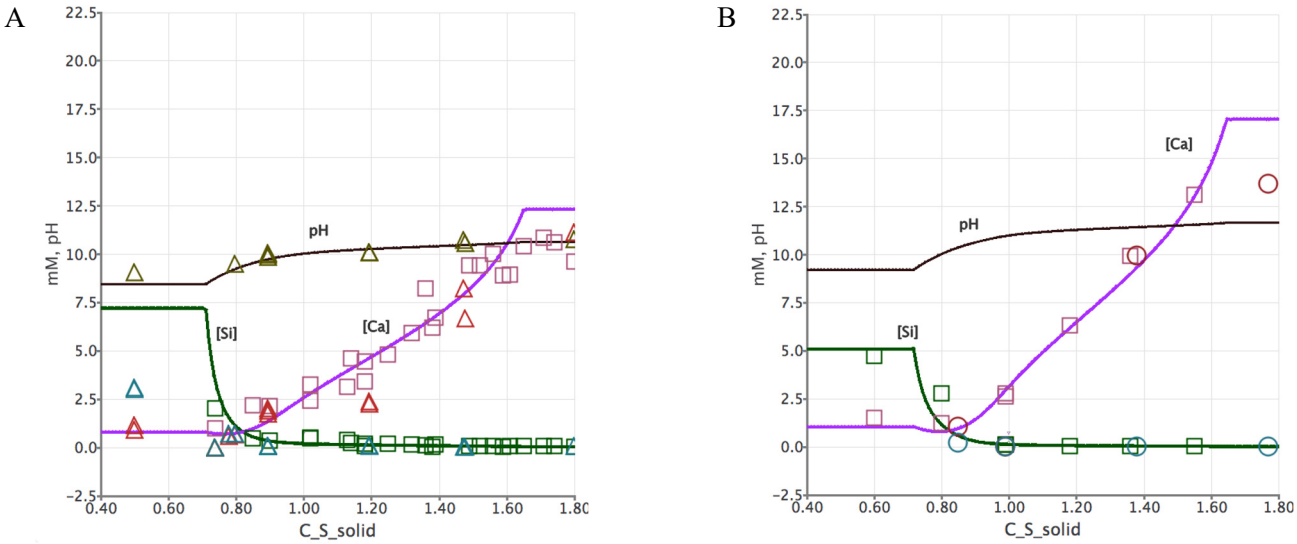

Fig. 6.7: Profiles of total dissolved $[Ca]_{aq}$, $[Si]_{aq}$ and pH predicted by the CASH+ core model for T = 90 °C (A) and T = 50 °C (B). C_S_solid is the molar Ca/Si ratio in the solid part of the system. Experimental data in (A): (Courault 2000), 90 °C, squares; (Atkins et al. 1994), 85 °C, triangles; data in (B): (Glasser et al. 1999), 55 °C, circles; (Myers et al. 2015), 50 °C, squares. Screen images from GEM-Selektor v.3.7.0 code. From (Kulik et al. 2020, submitted manuscript).

6.6 References

Atkins M., Glasser F.P., Moroni L.P., Jack J.J. (1994) Thermodynamic modelling of blended cements at elevated temperature (50-90 °C). Department of the Environment (UK), HMIP Report, 193.

Courault E. (2000)
Simulation experimentale des C-S-H dans les betons modernes: etude de la composition et des proprietes a l'equilibre dans des milieux complexes, PhD thesis, Universite de Bourgogne, Dijon, France.

Di Bernardo P., Endrizzi F., Melchior A., Zhang Z., Zanonato P.L., Rao L. (2018)
Complexation of Th(IV) with sulfate in aqueous solution at 10–70 °C. J. Chem. Thermodyn. 116, 273–278.

Grenthe I., Gaona X., Plyasunov A.V., Rao L., Runde W.H., Grambow B., Konings R.J.M., Smith A.L., Moore E.E. (2020)
Second Update on the Chemical Thermodynamics of Uranium, Neptunium, Plutonium, Americium and Technetium. Chemical Thermodynamics, Vol. 14. OECD Publications, Paris, France, 1503.

Glasser L., Jenkins H.D.B. (2016)
Predictive thermodynamics for ionic solids and liquids. Physical Chemistry and Chemical Physics 18, 21226-21240.

Chermak J.A., Rimstidt J.D. (1989)
Estimating the thermodynamic properties (ΔG_f° and ΔH_f°) of silicate minerals at 298 K from the sum of polyhedral contributions. American Mineralogist 74, 1023-103.

Ghazizadeh S., Hanein T., Provis J.L., Matschei T. (2020)
Estimation of standard molar entropy of cement hydrates and clinker minerals. Cement and Concrete Research 136, 106188.

Gu Y., Gammons C.H., Bloom M.S. (1994)
A one-term extrapolation method for estimating equilibrium constants of aqueous reactions at elevated temperatures. Geochim. Cosmochim. Acta 58, 3545–3560.

Guillaumont R., Fanghänel T., Neck V., Fuger J., Palmer D.A., Grenthe I., Rand M.H. (2003)
Update on the chemical thermodynamics of uranium, neptunium, plutonium, americium and technetium. Chemical Thermodynamics, Vol. 5. Elsevier, Amsterdam, The Netherlands, 919.

Hummel W. (2020)
The PSI Chemical Thermodynamic Database 2020: Data Selection for Organic Ligands. PSI Internal Report, TM-44-20-01, Paul Scherrer Institut, Villigen, Switzerland.

Hummel W., Curti E. (2020)
The PSI Chemical Thermodynamic Database 2020: Data Selection for Phosphorus and Application to HLW near-field pore water modelling. PSI Internal Report, TM-44-20-06, Paul Scherrer Institut, Villigen, Switzerland.

Hurst J.E., Harrison K. (1992)
Estimation of liquid and solid heat capacities using a modified Kopp's rule. Chemical Engineering Communications 112, 21-30.

Jordan N., Demnitz M., Lösch H., Starke S., Brendler V., Huittinen N. (2018)
Complexation of Trivalent Lanthanides (Eu) and Actinides (Cm) with Aqueous Phosphates at Elevated Temperatures. Inorg. Chem. 57, 7015–7024.

Kulik D.A. (2011)
Improving the structural consistency of C-S-H solid solution thermodynamic models. Cement and Concrete Research 41, 477-495.

Kulik D.A., Miron G.D., Lothenbach B. (2020)
A structurally-consistent CASH+ sublattice solid solution model of fully hydrated C-S-H phases: Thermodynamic basis, methods, and Ca-Si-H_2O core sub-model. In submission.

Lemire R.J., Fuger J., Spahiu K., Sullivan J.C., Nitsche H., Ullman W.J., Potter P., Vitorge P., Rand M.H., Wanner H., Rydberg J. (2001)
Chemical Thermodynamics of Neptunium and Plutonium. Chemical Thermodynamics, Vol. 4, Elsevier, Amsterdam, The Netherlands, 845.

Lemire R.J., Palmer D.A., Schlenz H., Taylor P. (2020)
Chemical Thermodynamics of Iron, Part 2. Chemical Thermodynamics, Vol. 13b. OECD Publications, Paris, France, 882.

Lothenbach B., Kulik D.A., Matschei T., Balonis M., Baquerizo L., Dilnesa B., Miron G.D., Myers R.J. (2019)
Cemdata18: A chemical thermodynamic database for hydrated Portland cements and alkali-activated materials. Cement and Concrete Research, 115, 472–506.

McCann H.G. (1968)
The solubility of fluorapatite and its relationship to that of calcium fluoride. Arch. oral Biol., 13, 987-1001.

McDowell H., Brown W.E., Sutter J.R. (1971)
Solubility study of calcium hydrogen phosphate. Ion-pair formation. Inorg. Chem., 10, 1638-1643.

Miron G.D., Kulik D.A., Thoenen T. (2020)
Generating isocoulombic reactions as a tool for systematic evaluation of temperature trends of thermodynamic properties: Application to aquocomplexes of lanthanides and actinides. Geochim. Cosmochim. Acta 286, 119–142.

Myers R.J., L'Hôpital E., Provis J. L., Lothenbach L. (2015)
Effect of temperature and aluminium on calcium (alumino) silicate hydrate chemistry under equilibrium conditions. Cement and Concrete Research 68, 83-93.

Pearson F.J., Berner U. (1991)
Nagra Thermochemical Data Base I. Core Data. Nagra Technical Report 91-17, Nagra, Wettingen, Switzerland.

Pearson F.J., Berner U., Hummel W. (1992)
Nagra Thermochemical Data Base II. Supplemental Data 05/92. Nagra Technical Report 91-18, Nagra, Wettingen, Switzerland.

Rao L., Tian G. (2009)
Complexation of Lanthanides with Nitrate at Variable Temperatures: Thermodynamics and Coordination Modes. Inorg. Chem. 48, 964–970.

Skerencak A., Panak P.J., Hauser W., Neck V., Klenze R., Lindqvist-Reis P., Fanghänel T. (2009) TRLFS study on the complexation of Cm(III) with nitrate in the temperature range from 5 to 200 °C. Radiochim. Acta 97, 385–393.

Tian G., Shuh D.K. (2014) A spectrophotometric study of Am(III) complexation with nitrate in aqueous solution at elevated temperatures. Dalt. Trans. 43, 14565–14569.

Valyashko V.M., Kogaro L.N., Khodakovskiy I.L. (1968) Stability of fluorapatite, chlorapatite and hydroxyapatite in aqueous solutions at different temperatures. Geochemistry International 5, 21-30.

Wagman D.D., Evans W.H., Parker V.B., Schumm R.H., Halow I., Bailey S.M., Churney K.L., Nuttall R.L. (1982) The NBS Tables of Chemical Thermodynamic Properties. J. Phys. Chem. Ref. Data 11, Suppl. 2. 336.

Xia Y.X., Friese J.I., Moore D.A., Bachelor P.P., Rao L. (2007) Complexation of plutonium(IV) with sulfate at variable temperatures. J. Radioanal. Nucl. Chem. 274, 79–86.

7 FUNDAMENTAL ASPECTS OF MINERAL REACTIVITY AND STRUCTURAL TRANSFORMATIONS

Churakov S.V., Cametti G., Di Lorenzo F., Adams D., Schliemann R. (PhD student), Krattiger N. (MSc student), Roos D. (MSc student), Steiner K. (MSc student), Arnold T. (BSc student)

7.1 Introduction

PSI/LES and the Institute for Geological Science at the University of Bern (UBERN/IfG) collaborate in the field of mineralogy, crystallography and environmental geochemistry. The research field of the Mineralogy group at the University of Bern covers fundamental aspects of mineral dissolution and precipitation mechanisms, chemical aspects of crystal structure stability and temperature driven phase transitions in minerals. The dedicated laboratories operated by the group are equipped with powder and single-crystal diffractometers for structural studies of minerals and an atomic force microscopy laboratory for *in situ* characterisation of mineral surfaces. The experimental studies are widely supported by modelling activities. In particular, we develop and apply numerical methods for investigations of reaction mechanisms and theoretical predictions of mineral thermodynamics. Main research activities are focused on the characterisation of mineral structure transformations in natural and synthetic zeolite materials as result of dehydration and cation exchange processes. These structural characterisation studies are conducted combining single crystal X-ray diffraction experiments, spectroscopic measurements, and molecular simulations. *Ab initio* molecular dynamics simulations are further used to elucidate the mechanism of clay minerals dissolution at an atomic-scale. Dedicated laboratory nucleation and re-crystallisation experiments, surface characterisations and geochemical modelling are applied to develop sustainable strategies for heavy metal extraction from contaminated water via carbonates precipitation.

7.2 The interaction of carbonate minerals with aqueous Pb^{2+}

Many divalent hazardous metals are known to form insoluble carbonate minerals. Their solubility products are up to five orders of magnitude lower than that of abundant materials like magnesite (MGS), calcite (CAL), aragonite (ARG) and dolomite (Fig. 7.1 A). These highly abundant Ca and Mg carbonate minerals can be used for remediation of contaminated waters and binding hazardous metal as insoluble carbonates. As an example, the highly toxic Pb^{2+} a carbonate minerals called cerussite (CER, $PbCO_3$) is formed by conversion of MGS, CAL and ARG when they are in contact with a Pb^{2+} bearing solution (Fig. 7.1 B-C). The large difference in solubility between substrates and product determine a strongly negative Gibbs free energy of reaction, which means that the process is spontaneous even in conditions of standard pressure and temperature (Putnis 2009). Kinetic effects could substantially modify the behaviour of the system (Di Lorenzo et al. 2017). The lack of reliable tools to predict the existence of kinetic barriers makes crucial to derive experimentally the kinetic information relevant for the specific system. The experimental determination of the kinetic effects that are relevant for heavy metal uptake by abundant carbonate minerals has been in focus of our studies aimed at the development of novel remediation techniques.

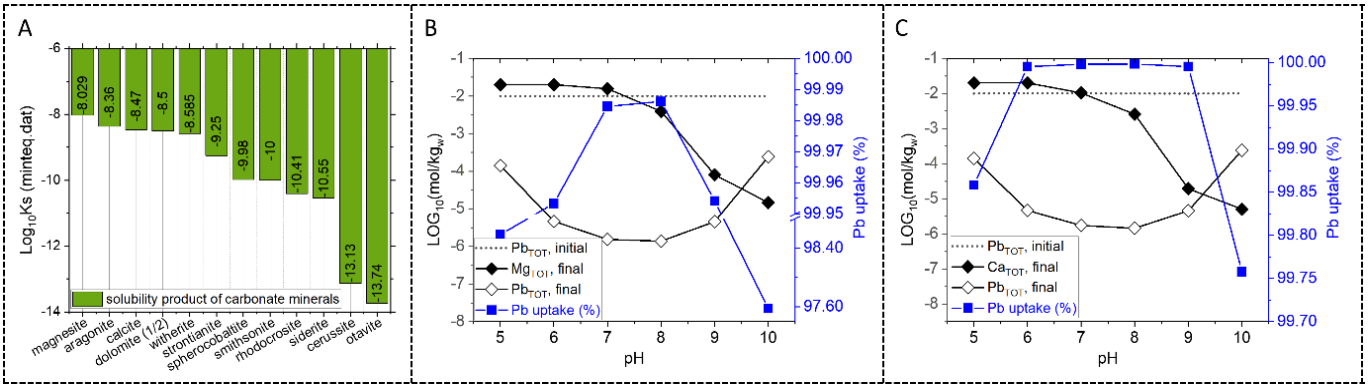

Fig. 7.1: A) Compilation of the solubility products of carbonate minerals. B) The interaction of magnesite with a Pb-bearing solution results in strong incorporation of Pb^{2+} into the solid phase, if equilibrium is reached. C) Analogously to magnesite, calcite is also efficient for Pb^{2+} removal. Similar results are obtained from simulations performed using aragonite and dolomite as remediation agents.

7.2.1 The effect of solid-liquid interface in controlling the Pb^{2+} uptake efficiency by $CaCO_3$

Recently we have performed a comparative experimental study of the Pb^{2+} uptake by calcite and aragonite, which are the two most abundant $CaCO_3$ polymorphs. Despite the very similar solubility of these two phases, their overall ability to uptake Pb^{2+} is significantly different (Di Lorenzo et al. 2019). The moles of Pb precipitated in the experiments with CAL, normalised by surface area, doubles the amount precipitated with ARG, during batch re-crystallisation experiments over the period between 12 hours and 10 days (Figure 7.2). In 2020, we successfully provided a mechanistic interpretation to the different reaction behaviours and validated our theory with experimental observations. (Di Lorenzo et al. 2020) Atomic Force Microscopy (AFM), Transmission Electron Microscopy (TEM), Electron BackScattered Diffraction (EBSD) and two-dimensional-single crystal x-ray diffraction (2D-SCXRD) show that cerussite crystals grow in random directions on calcite. When these techniques are applied to a reacted aragonite grain, they show the formation of an oriented cerussite powder. In Figure 7.2, we highlight the main differences between the two polymorphs after the interaction with Pb^{2+}. Cerussite crystals grown on CAL shows a random orientation as confirmed by electron microscopy and by the presence of perfect Debye rings in the 2D-SCXRD frame. On the other hand, CER crystals forms an almost perfect layer on ARG. Aragonite grains are perfectly coated by $PbCO_3$ and a 2D-SCXRD frame shows that CER is an oriented powder co-aligned with the substrate.

Aragonite surfaces acts as a template for cerussite nucleation and growth, thus they decrease the critical supersaturation (SI) necessary to nucleate the product phase. A low critical supersaturation promotes the formation of the product phase in the boundary layer rather than in bulk solution. Our mechanistic interpretation of the process can be described as follows (Fig. 7.3). The system is subdivided into three compartments: solid phase, the boundary layer and the bulk solution. Four reactive processes can be identified. The path "*1*", with a kinetic corresponding to "r_1", corresponds to the delivery of ions from the dissolving mineral to the boundary layer. Assuming calcite and aragonite to have the same dissolution rate, the rate "r_1" is the same in both systems. The process "*2*" correspond to the migration of ions from the boundary layer to the bulk solution. This process depends on atomic properties such as hydration and diffusion. Thus, the rate "r_2"should be the same because the starting materials are polymorphs. The process "*4*" is the homogenous nucleation of the product phase and it is an intrinsic property of the solid product. Finally, the process "*3*" is highly dependent on the template effect exerted by the substrate to favour the heterogeneous nucleation of the product. Therefore, the rates "r_2"and "r_3" determine the possibility for the system to transform via an interface-coupled dissolution-precipitation reaction.

It has been demonstrated that the reason behind the different reactivity of calcite and aragonite towards divalent lead uptake is the differences in reaction mechanism. In the case of calcite, the process is a simple solvent-mediated transformation. Instead, aragonite transformation occurs as an interface coupled dissolution-precipitation reaction that leads to a self-inhibited mineral replacement.

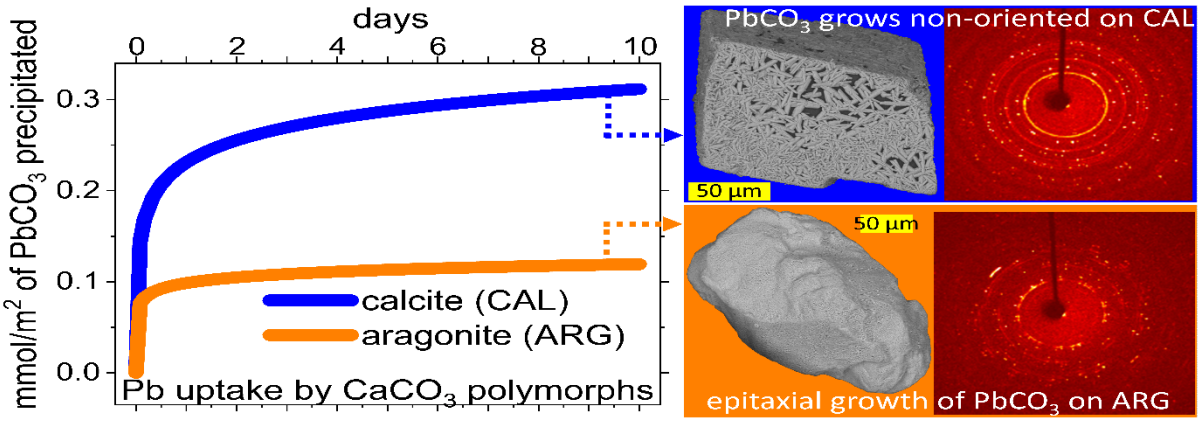

Fig. 7.2: Comparison of the uptake of Pb^{2+} by the two most abundant carbonate minerals (calcite and aragonite). The isostructural relationship between ARG and cerussite (both phases are orthorhombic) favors the epitaxial growth of the product on the substrate, and leads quickly to surface passivation. The absence of epitaxial growth in the CAL-cerussite system allows a higher Pb removal efficiency (Di Lorenzo et al. 2020).

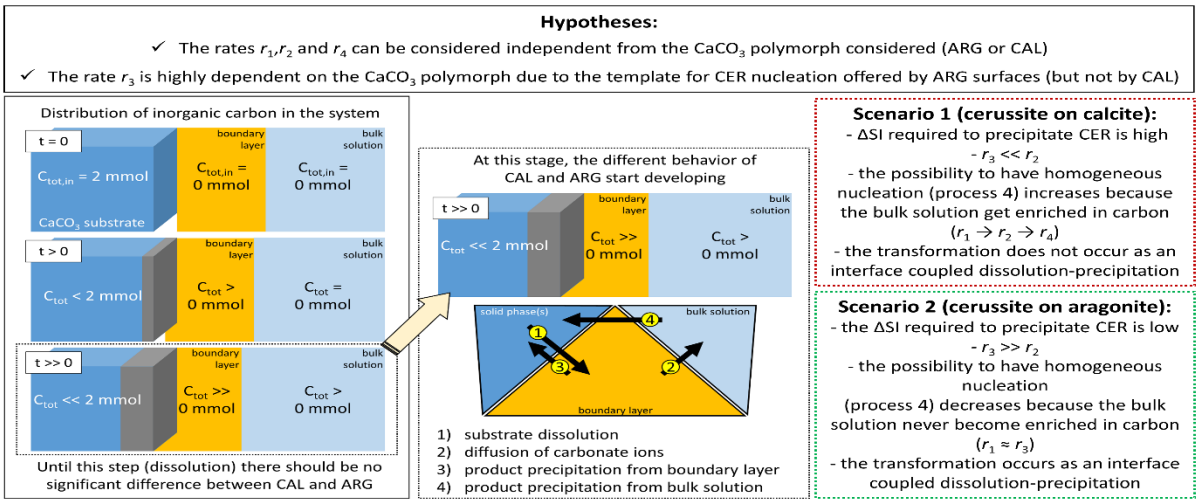

Fig. 7.3: Mechanistic interpretation of the different behaviours observed during Pb^{2+} uptake by calcite and aragonite. The template offered by ARG surfaces for CER nucleation causes surface passivation (Di Lorenzo et al. 2020).

7.2.2 The effect of Pb^{2+} on the initial steps of $CaCO_3$ crystallisation

Nucleation and growth of $CaCO_3$ are key factors for carbon sequestration technologies under development. Projects like Carbfix (Matter et al. 2011; Gislason & Oelkers 2014) where dissolved CO_2 is mineralized by injection into basaltic rocks, would take advantage from the possibility to use contaminated water instead of fresh groundwater. The main potential benefits are: i) The combination of wastewater treatment and carbon storage could reduce the overall costs while promoting more sustainable technologies (Lu et al. 2018). ii) The presence of heavy metals could delay carbonate precipitation favouring a longer persistence of permeability in the basaltic injection site.

The nucleation kinetic of Ca carbonates has been investigated within the Master project of Kay Steiner. The aim of this project is to obtain kinetics data on Pb^{2+} incorporation into $CaCO_3$ as function of ionic strength and pH. The preliminary results (Fig. 7.4) show that the presence of trace amounts of lead (Ca/Pb = 100, red line) delays the nucleation and reduces the growth rate of $CaCO_3$. When the Ca/Pb ratio decreases to 10, the effect on $CaCO_3$ nucleation and growth is similar, but a secondary Pb-rich phase is formed in addition. This Pb-rich phase has been identified as hydrocerussite ($Pb_3(CO_3)_2(OH)_2$) by Infrared spectroscopy. Scanning electron microscopy (SEM) shows that hydrocerussite incorporates Ca^{2+} ions when the precipitation occurs at pH 9, but not at pH 8. This evidence highlights the role

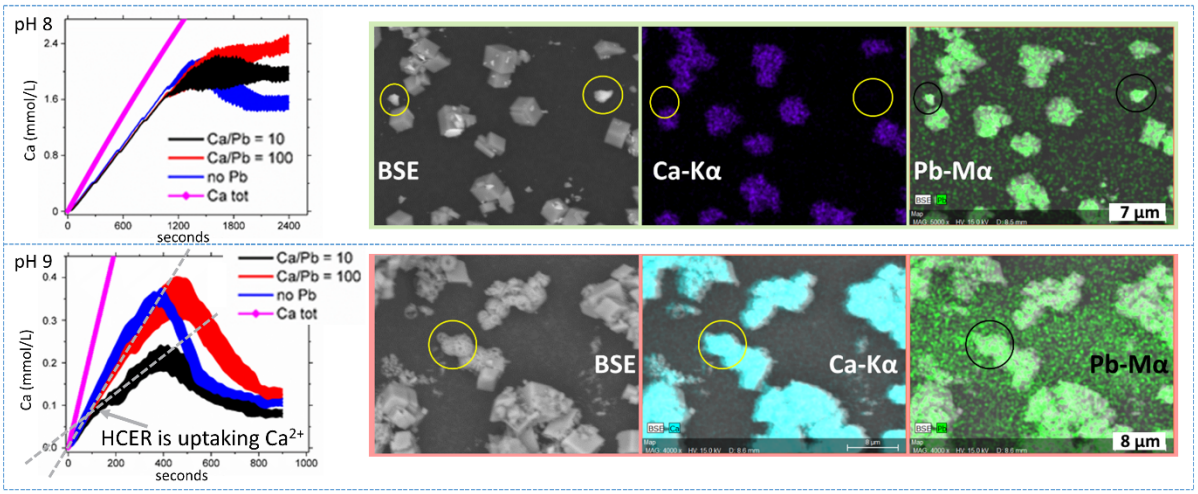

Fig. 7.4: Titration profiles obtained from calcium ion selective electrode according to the procedure developed by Gebauer et al. (2008). SEM micrographs and chemical maps are reported for the experiments with Ca/Pb = 10. The circles highlight some grains corresponding to the secondary Pb-rich phase (hydrocerussite). This phase precipitates without incorporating significant amounts of Ca^{2+} at pH 8. At higher pH, both Ca and Pb are incorporated in the secondary phase, as testified by the slope change in the titration curve.

of pH in controlling ion partitioning in far from equilibrium conditions. Further studies will investigate the role of pH and ionic strength in controlling the mixing properties of calcium and lead.

7.2.3 The suitability of magnesite towards Pb^{2+} uptake

The results obtained for Pb^{2+} uptake by CAL and ARG motivated the investigation of other abundant carbonate minerals with rhombohedral structure that could be used for an efficient uptake of lead ions from solution. Despite the high solubility of MGS (Fig. 7.1), many authors reported the existence of an elevated kinetic barrier that slows down the attainment of equilibrium (Saldi et al. 2009; Bénézeth et al. 2011; Xu et al. 2013). The change in the reactivity of magnesite at saturated solution (SI $\approx$ 2) in presence and in absence Pb^{2+} was investigated within the Bachelor Thesis of Tobias Arnold, defended in May 2020. The flow through AFM experiments demonstrated that the presence of Pb^{2+} has a dramatic influence on the reactivity of magnesite. In absence of Pb, it was not possible to measure any significant step propagation or to detect 2D-island nucleation. In presence of trace amounts of Pb^{2+} (Mg/Pb = 6600) two distinct behaviours have been observed depending on the ageing of the supersaturated solution. The 2D-island nucleation of a phase that quickly covers the {104} surfaces of MGS (Fig. 7.5 A) was observed when the supersaturated solution injected in the AFM experiments was prepared more than 1 week before the experiment. This phase was easily removable by flowing acidic water with pH 4 (Fig. 7.5 B) and the MGS surface underneath showed no signs of dissolution or modification. Contrary, a well measurable step dynamics was observed and measured on the MGS surface, when the supersaturated solution was prepared just before the experiment (Fig. 7.5 C).

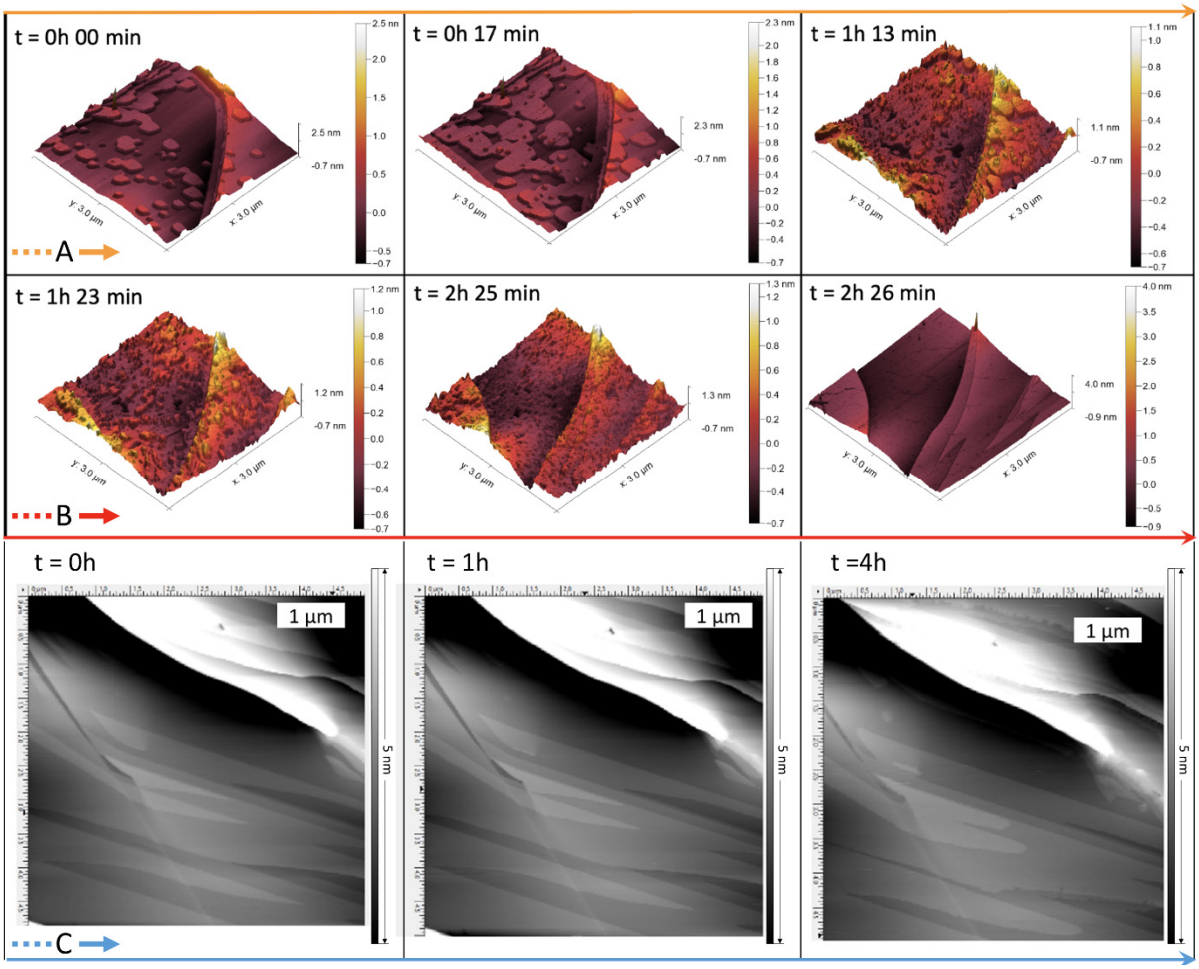

Fig. 7.5: A) Temporal evolution of a MGS surface after flowing a solution supersaturated with respect to magnesite. The solution was prepared 1 week before the AFM experiments. B) Dissolution of the phase nucleated on MGS with an acidic solution, pH 4. C) When the Pb-bearing supersaturated solution was prepared immediately before the experiments, MGS steps propagation could be observed at 25 °C.

7.3 Coordination chemistry and thermal stability of cation exchanged zeolites

Microporous zeolites have a well-defined framework structure and exchangeable extraframework (EF) cations. It is well-known that the sorption, catalytic and in general the physio-chemical properties of these materials can be modified via ion-exchange. In particular, the incorporation of transition and heavy metals (such as Cd, Zn, Ag, and Pb) was demonstrated to be particularly effective to improve their performance in various technological applications (Colella 1999; Ackley et al. 2003; Abreu et al. 2019). In the framework of SNSF Ambizione grant *"Insight into sorption mechanism of natural zeolites: Investigation of the bulk structural and surface-modifications after heavy-metal treatment in aqueous solutions" PZOOP2_173997,* principle investigator and grant holder Dr. G. Cametti (University of Bern), the structural stability of Ag^{+}, Cd^{2+}, and Pb^{2+} modified natural zeolites are investigated. The aim of this project is to determine: i) the coordination chemistry of the metal cations and their interaction with the framework; ii) the effect of the ion-exchange on the zeolites thermal-stability.

One of the project tasks focusses on small pore zeolites, namely levyne (framework type LEV) and erionite (framework type ERI). The Ag^{+} and Cd^{2+} forms of levyne and erionite were investigated by coupling single-crystal X-ray Diffraction (SCXRD), X-ray Absorption Fine Structure Spectroscopy (XAFS) and theoretical DFT-based Molecular Dynamics simulations. Data obtained by these complementary techniques consistently indicated that Cd^{2+} in LEV is arranged in a nearly ordered fashion. In contrast, strong disorder of the EF species (Cd^{2+} and H_2O) is observed in the ERI cavities. In the latter, Cd^{2+} forms aqueous complexes that are more mobile in comparison to Cd^{2+} in LEV, where Cd^{2+} bonds to both H_2O and framework-oxygen atoms. The formation of Cd-clusters is excluded based on Extended X-Ray Absorption Fine Structure (EXAFS) analysis.

Interestingly, the contrasting structural trends are found in the Ag-exchanged forms (Ag-LEV and Ag-ERI), *i.e.* Ag ions are more diffuse and disordered in levyne compared to erionite (Fig. 7.6). In this case, the thermal stability of Ag-LEV phase was tracked *in situ* by SCXRD and XAFS, and interpreted based on combination of experimental and modelling approaches. Differences in the dehydration behavior of Ag-LEV compared to Ca-LEV were found. In particular, no transformation to the levyne B' topology (as detected in Ca-LEV) occurred in Ag-LEV. Concerning Ag ions in the LEV framework type, the following conclusions can be drawn: i) as a function of temperature, Ag ions migrate within the cavities to maintain a coordination number similar to the RT conditions; ii) the Ag-O bonds (from 2.14 to 2.4 Å) are characteristic of short covalent-bonds, in agreement with the low coordination number of silver; iii) weak Ag^{1+}-Ag^{1+} interaction and clustering occur in Ag-LEV at room temperature only, whereas they persist in the inter-grown Ag-ERI phase up to 650°C.

Effect of Pb^{2+} on the thermal stability of STI and LEV framework type zeolites is co-investigated in master thesis of Diana P. Roos. The uptake of Pb^{2+} by zeolites is relevant in the context of environmental remediation

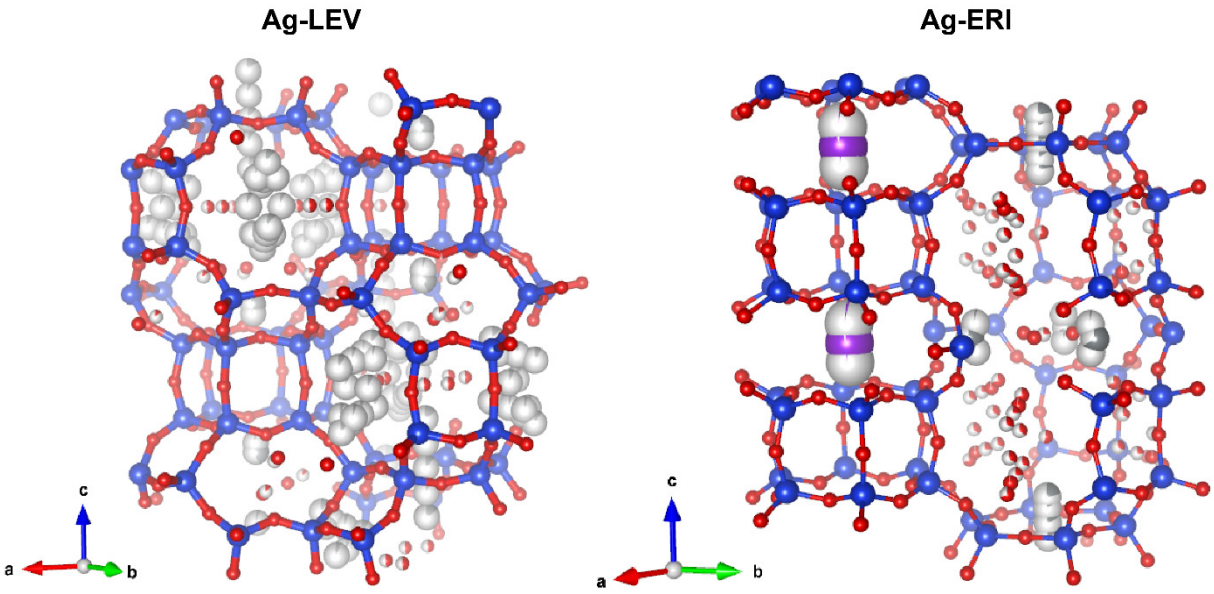

Fig. 7.6: Crystal structure of Ag-LEV and Ag-ERI at RT obtained by SC-XRD. Blue and red spheres represent Si/Al and O atoms, respectively. Ag atoms are shown in grey. Purple balls in Ag-ERI structure represent K atoms. Partially colour of crystallographic sites corresponds to partial occupancy.

and industrial processes. Because of the well-known toxicity of lead species, numerous studies were conducted on the ion exchange capacity and subsequent eventual removal of these compounds by natural and synthetic zeolites. Moreover, from a structural point of view, Pb-exchanged zeolites showed interesting phenomena such as Pb over-exchange and formation of different type of Pb-clusters inside the zeolitic cages (Nardin et al. 1995; Yeom et al. 1997). In this Master project, two Pb-zeolites with LEV and STI framework type were produced by ion-exchange. Chemical analyses by Electron Microprobe indicated a systematic surplus of Pb^{2+} compared to that required to balance the negative charge of the framework. The thermal stability of Pb^{2+} exchanged LEV and STI frameworks have been investigated by stepwise dehydration using single crystal X-ray diffraction. An anomalous behavior (switching from negative to positive thermal expansion) of the unit-cell volume as a function of temperature was observed in both samples. To interpret such behavior, Molecular Dynamics simulations have been applied for different structural models in broad temperature range. The rationalization of the computational and experimental results is ongoing.

7.4 Thermodynamic stability of solids from first principle

Thermodynamic properties of materials can be predicted from first principle quantum mechanical calculations knowing the derivatives of the free energy or equivalently of the partition function. Such calculations are very demanding computationally. Moreover, the thermal dependence of the partition function must include anharmonic effect, which depend on the full interaction potential. Therefore, the accurate prediction of the vibrational excitation spectra are of high interest. In contrast to harmonic and quasi-harmonic lattice dynamics (HLD), Decoupled anharmonic mode approximation (DAMA) takes into account the full potential energy surface (PES) along the eigenmodes in an independent particle approximation. Both, HLD and DAMA, describe the phonon interaction up to second order. This allows not only the examination of high temperature phases of crystals, which often show multiple energy minima at the PES, but also to take into account higher order corrections in the thermodynamic properties.

Recently, the real space DAMA approach (Adams & Passerone 2016) was extended to the reciprocal space (q-DAMA, Project Lead Dr. D. Adams), to allows more efficient estimation of vibrational anharmonic band structures and vibrational DOS, via q-point sampling. The new implementation of q-DAMA has been benchmarked against Self-Consistent ab-initio Lattice Dynamics (SCAILD; Souvatzis 2008), Molecular dynamics (MD), which both take into account contributions of the PES beyond the harmonic approximation (Adams et al. 2020).

The q-DAMA was applied to calculate the phonon dispersion and the phonon density-of-states, heat capacity, and the mean atomic displacement. In comparison with the HLD, the q-DAMA indicates a negligible anharmonic contribution to phonon frequencies (Fig. 7.7), a small, but significant influence on heat capacity. On the other hand, q-DAMA outperforms the other approximations in predicting the lattice parameter (Fig. 7.8) and the mean atomic displacement. The displacement amplitudes predicted by the q-DAMA are in good agreement with displacement amplitudes determined by the Debye-Waller factor in X-ray diffraction experiments. This

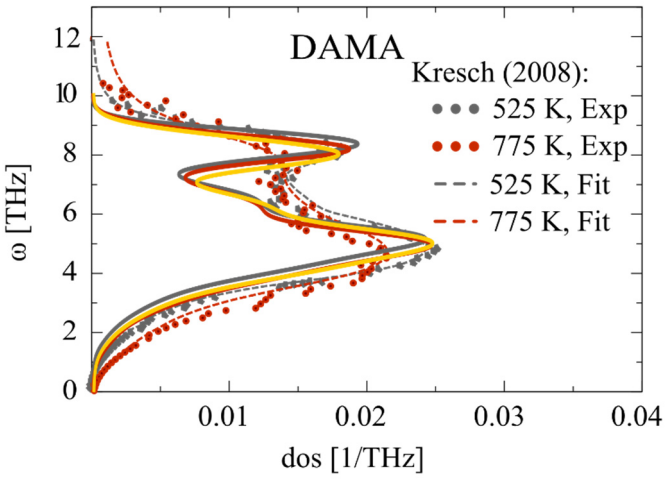

Fig. 7.7: Phonon density-of-states predicted by q-DAMA and compared to experimental data by Kresch et al. (2008) at 525 K and 775 K (dots).

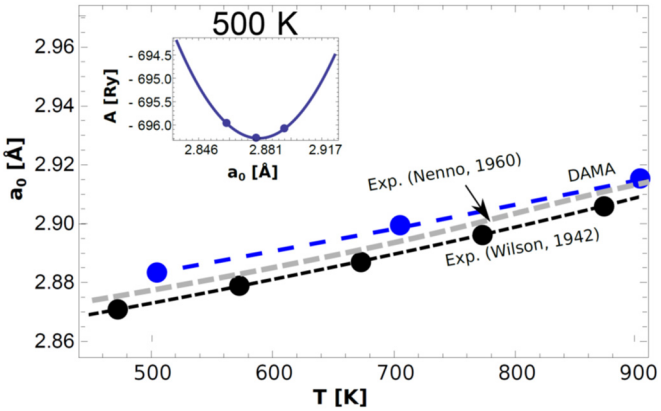

Fig. 7.8: Temperature dependence of lattice constant for fcc Al. Results from DAMA simulations (blue) at T = 500 K, T = 700 K and T = 900 K are compared to experimental data (grey and black). Inset: Lattice constant determination at T = 500 K by free energy minimization.

encourages the application of the q-DAMA applications to other materials, especially to those with strong anharmonicities including materials with soft modes.

7.5 Atomic scale mechanism of clay mineral reactivity

The surface complexation of metals on clay minerals is closely related to the reactivity and dissolution/precipitation processes at the edge sites of the clay platelets. The surface complexation can also act as a precursor for neo-formation of phyllosilicates. Both, neo-formation of phyllosilicates and concurrent dissolution/precipitation reactions are particularly important for the irreversible retention of hazardous cations. The structural incorporation requires recrystallization of the solid leading to dissolution of pristine material and precipitation of a new phase. The detailed mechanism of this process and the relation to the microscopic kinetics of clay mineral dissolution is strongly debated. Within the SNSF PhD project of René Schliemann, *ab initio* molecular dynamics simulations were applied to directly evaluate the dissolution mechanism and the activation energy of Al and Si leaching from idealized (110) and (010) edge surfaces of pyrophyllite in pure water at ambient conditions and also at elevated pressures. In contrast to the majority of the studies, this work explicitly takes into account for the atomistic mineral surface structure as well as finite temperature dynamics of solvent molecules in first and second coordination shell of reacting surface sites. The simulations provide mechanistic insight into atomic scale details on the step by leaching of tetrahedral and octahedral units at phyllosilicate surface (Schliemann & Churakov 2021; Churakov & Schliemann 2021).

The simulations reveal that the overall reaction mechanism can be rationalized as sequence of concurrent and reversible elementary reaction steps, which are (1) nucleophilic attack of ligands (H_2O/OH) on the dissolving surface site; (2) ligand exchange reactions in the first coordination shell of the reacting sites leading to changes of its conformation and denticity at the mineral surface; (3) collective proton transfer reactions between the acidic and basic oxygen sites mediated via a chain of the hydrogen bonded molecules in the first and second coordination shell of the reacting site (Fig. 7.8).

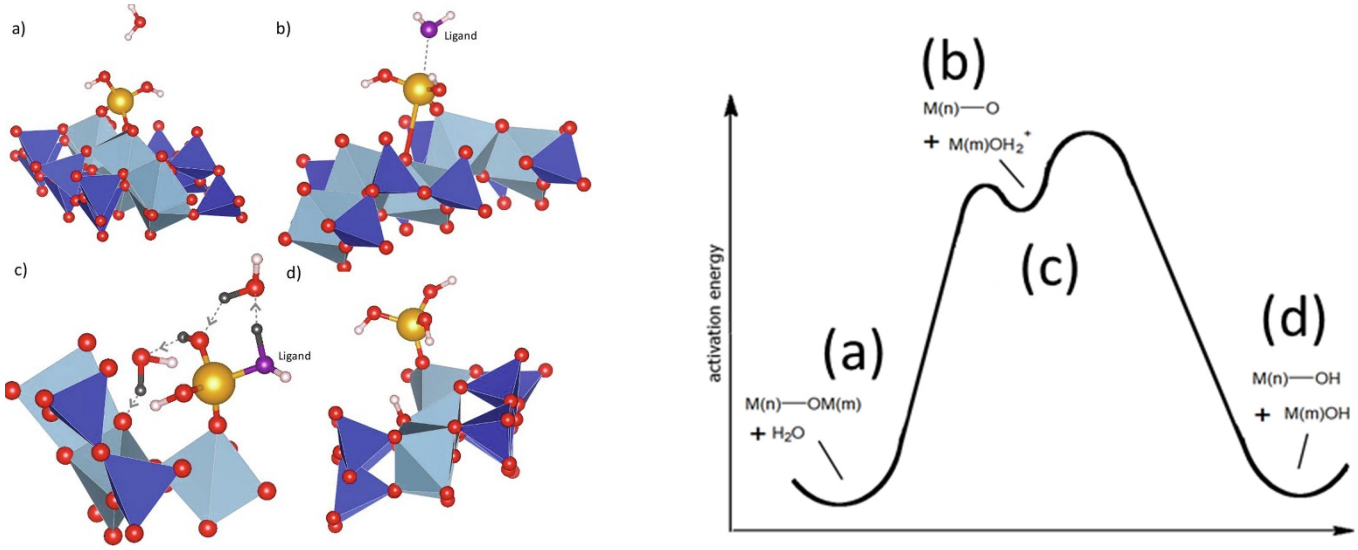

Fig. 7.8: Left: Schematic representation of a step-by-step Si-O bond hydrolysis for a bidentate surface >SiO_xH_y complex on the edge surface of clay minerals. Part of the edge surface is shown using polyhedral representation. Surface Si tetrahedra and Al octahedra are shown as blue and cyan polyhedral respectively. Oxygen atoms are represented by small red spheres. Water molecules not involved in the reaction process are omitted for the sake of clarity. The initial reaction step corresponds to the nucleophilic attack of a water molecule (magenta colour) on the bidentate surface complex, which destabilises the tetrahedral configuration and increases coordination number of Si ion from four to five. Thereafter, Si atom moves towards the ligand molecule and becomes a mono-dentate complex(c). This process is best described as a ligand-exchange. Stabilisation of the neo-formed complex require protonation of dangling oxygen site on the surface and the rearrangement of OH/H_2O molecules in the hydration shell of the surface complex (d). The direction of proton transfer along HB is shown by arrows. The net proton transfer is a result of several protons (dark grey) moving simultaneously along the chain of HB. The reaction product is a mono-dentate surface complex (d). Right: Schematic representation of the corresponding reaction barriers and energies of the intermediate complexes (Schliemann & Churakov 2021).

The pyrophyllite can be seen as the simplest structural prototype for the large variety of 2:1 phyllosilicates. The details of the dissolution mechanism obtained in this study for the pyrophyllite should be well applicable to a wide range 2:1 phyllosilicates. Analysis of the activation energies obtained in the simulations suggest that the major dissolution-reaction-controlling steps is the nucleophilic attack of a ligand molecule on the reacting site. Aqueous OH-ion is a stronger nucleophilic agent than water. Accordingly, the increasing dissolution rate of the phyllosilicate minerals at basic pH can be attributed to the higher concentration of OH, which is a stronger nucleophilic agent. Proton transfer reaction from an acidic to a more basic surface site plays a critical role in the stabilization of the reaction intermediates. The successful proton transfer reactions reduce the probability of the reversible intermediate reactions. The proton transfer reactions are essentially barrier free. The activation energy for this reaction step depends on the probability of the specific hydrogen bond arrangement of water molecules enabling the proton transfer reaction. The acidic pH conditions increase availability of protons for the saturation of under-coordinated oxygen sites and thus stimulate net dissolution process by reducing the probability of reverse precipitation reactions.

7.6 Comparative study of cation uptake and surface charge in C-S-H and ASR phases

Alkali-silica reaction (ASR) is one of the most important concrete durability issues worldwide. It was shown recently that ASR products have a structure similar to the natural mineral shlykovite. The sorption properties of ASR are barely known experimentally. A comparative study of C-S-H and ASR sorption properties and surface charge has been conducted within the BSc and the follow up MSc project of Nicolas Krattiger using reactive Grand Canonical Monte Carlo simulations. Both, C-S-H and ASR products have a negatively charged surface and thus adsorb preferentially cations at their surface; their surface charges become more negative at higher pH values due to the deprotonation of the ≡SiOH surface sites. The comparative study of C-S-H and ASR product shows that differences in the surface sites protonation state, evolution of surface charge and the ion adsorption as function of pH is largely determined by the distinct surface site densities in both phases. The density of the titratable ≡SiOH surface sites on C-S-H is nearly two times larger than that of ASR product. Accordingly, the highest expected surface charge of the C-S-H surface (e.g. 100% deprotonation of surface sites) is the two times the maximal surface charge density expected for ASR product. Since the ion adsorption is primary driven by electrostatic interaction of ions with the charged surface sites, the C-S-H has higher sorption capacity than ASR product. At equilibrium with the same electrolyte solution C-S-H adsorb more cations and anions per unit of surface area than ASR product. The model used in this study suggests that the ζ-potential of the ASR product remains weakly negative at the most relevant conditions (Krattiger et al. 2021).

7.7 References

Abreu N. J., Valdés H., Zaror A.C., Azzolina-Jury F., Meléndrez M.F. (2019)
Ethylene adsorption onto natural and transition metal modified Chilean zeolite: An *operando* DRIFTS approach. Microporous and Mesoporous Materials, 274, 134-148.

Ackley M., Rege S.U., Saxena H. (2003)
Application of natural zeolites in the purification and separation of gases. Microporous and Mesoporous Materials, 61, 25-42.

Adams D.J., Passerone D. (2016)
Insight into structural phase transitions from the decoupledanharmonic mode approximation, J. Phys. Cond. Matt. 28, 305401.

Bénézeth P., Saldi G.D., Dandurand J., Schott J. (2011)
Experimental determination of the solubility product of magnesite at 50 to 200 °C. *Chemical Geology*, 286(1–2), 21–31.

Churakov S.V., Schliemann R. (2021)
Ab initio simulations of clay minerals reactivity and thermodynamics, in C.I. Sainz-Díaz (Editor). Computational Modeling in Clay Mineralogy, AIPEA Educational Series, Pub. No. 3, Chapter 6, Digilabs, Bari, Italy.

Colella C. (1999)
Environmental applications of natural zeolitic materials based on their ion-exchange properties. In Application of natural microporous materials in environmental technology; Misaelides P., Macasek F., Pinnavaia T. J., Colella C. Eds.; NATO Science Series (Applied Sciences); Kluwer: Dordrecht, 1999; Vol. E362.

Di Lorenzo F., Prieto M. (2017)
Dissolution-Recrystallization of (Mg,Fe)CO_3 during Hydrothermal Cycles: Fe^{II}/Fe^{III} Conundrums in the Carbonation of Ferromagnesian Minerals. *Crystal Growth and Design*, 17(8), 4170–4182.

Di Lorenzo F., Ruiz-Agudo C., Churakov S.V. (2019)
The key effects of polymorphism during Pb^{II} uptake by calcite and aragonite. *CrystEngComm*, 21(41), 6145–6155.

Gislason S.R., Oelkers E.H. (2014)
Carbon Storage in Basalt. *Science*, 344, 373–375.

Krattiger N., Lothenbach B., Churakov S.V. (2021)
Sorption and electrochemical properties of ASR product and C-S-H: a comparative modelling study. Cement & Concrete Research. (Submitted)

Kresch M., Lucas M., Delaire O., Lin J.Y.Y., Fultz B. (2008)
Phonons in aluminum at high temperatures studied by inelastic neutron scattering, Phys. Rev. B 77, 024301.

Lu L., Guest J.S., Peters C.A., Zhu X., Rau G.H., Ren Z.J. (2018)
Wastewater treatment for carbon capture and utilization. *Nature Sustainability*, 1(12), 750–758.

Matter J.M., Broecker W.S., Gislason S.R., Gunnlaugsson E., Oelkers E.H., Stute M., Sigurdardóttir H., Stefansson A., Alfreðsson H.A., Aradóttir E.S., Axelsson G., Sigfússon B., Wolff-Boenisch D. (2011)
The CarbFix Pilot Project – Storing Carbon Dioxide in Basalt. *Energy Procedia*, 4, 5579–5585.

Nardin G., Randaccio L., Zangrando E. (1995)
Lead clustering in a zeolite X. Zeolites 15, 684-688.

Putnis A. (2009)
Mineral replacement reactions. *Reviews in Mineralogy and Geochemistry*, 70, 87–124.

Saldi G.D., Jordan G., Schott J., Oelkers E.H. (2009)
Magnesite growth rates as a function of temperature and saturation state. *Geochimica et Cosmochimica Acta*, 73(19), 5646–5657.

Schliemann R., Churakov S.V. (2021)
Atomic scale mechanism of clay minerals dissolution revealed by *ab initio* simulations. Geochimica et Cosmochimica Acta, 293, 438-460.

Souvatzis P., Eriksson O., Katsnelson M., Rudin S. (2008)
Entropy driven stabilization of energetically unstable crystal structures explained from first principles theory, Phys. Rev. Lett. 100, 095901.

Xu J., Yan C., Zhang F., Konishi H., Xu H., Teng H.H. (2013)
Testing the cation-hydration effect on the crystallization of Ca-Mg-CO_3 systems. *Proceedings of the National Academy of Sciences of the United States of America*, 110(44), 17750–17755.

Yeom Y. H., Kim Y., Seff K. (1997)
Crystal structure of zeolite X exchanged with Pb(II) at pH 6.0 and dehydrated: $(Pb^{4+})_{14}(Pb^{2+})_{18}(Pb_4O_4)_8Si_{100}Al_{92}O_{384}$. Journal of Physical Chemistry B, 101, 5314-5318.

8 GEOCHEMICAL ASPECTS OF CONVENTIONAL WASTE MATERIALS AND THEIR DISPOSAL

Eggenberger U., Churakov S.V., Weibel G., Glauser A. (PhD student), Wolffers M. (PhD student), Zappatini A., Zucha W., Ulrich M. (MSc student), Erb A. (MSc student)

8.1 Introduction

The Competence Centre for Secondary Raw Materials at the Institute of Geological Sciences conducts applied research in the field of environmental geochemistry and secondary raw materials. The core competences of the Centre cover the topics of circular economy and disposal quality of conventional non-radioactive waste materials. Sustainable implementation of recycling technology is waste type specific and requires a detailed knowledge of the material composition, long-term behaviour and process couplings controlling the material degradation. For the metal recycling from the residues of municipal solid waste incineration (MSWI) and wood incineration (WI), a detailed knowledge about formation and composition of the incineration residues (bottom ash, fly ash, wood ash) is essential to optimize metal recovery. Within the framework of the recent Swiss Waste Ordinance (Swiss Confederation, 2016), the requirements for residues have increased and metal recovery must be implemented by 2021 for municipal solid waste incineration fly ash and by 2023 for waste wood ash.

The FLUWA process represents the state-of-the-art technology for heavy metal recovery in Switzerland. During the FLUWA process, the fly ash is leached with acid scrub water (an acid similar to 5% HCl arising at the flue gas cleaning system) in a multistage cascade. After roughly 60 minutes of extraction at 50-60°C, the suspension is separated by vacuum belt filtration. The resulting heavy metal enriched filtrate can be precipitated to a hydroxide sludge for subsequent heavy metal recovery and the filter cake (depleted in heavy metals) is deposited on landfills. An oxidizing agent (e.g. H_2O_2) is often added for the mobilization of Cu and Pb, since the mobilisation of these elements is favoured under oxidizing extraction conditions. Further potential for the optimisation for FLUWA process is investigated in ongoing PhD projects.

8.2 Optimisation of metal recovery from MSWI Fly Ash (FA)

The FLUWA operation conditions and the efficiency of metal recovery depend on the composition of the input ashes. The binding form of the metals and their element-specific chemical and physical properties determines the type of treatment. Effective removal of Cd, Cu, Pb and Zn from the fly ash requires the optimization of the FLUWA operating parameters. Different parameters can be adjusted depending on the composition of input ash and acidic scrub water quality. The pH value is defined by the alkalinity of the ash and the amount of acid cumulated from quench water and acid addition. The pH value is also the decisive, whether Pb and Cu are lost due to re-precipitation out of the filtrate during the washing process. Using a higher amount of ash per liquid (liquid/Solid ratio, L/S), a higher throughput of ash can be achieved. However, this renders a stable operation of the process to be more difficult. To create ideal conditions for the extraction of redox-sensitive metals (e.g. Cd, Cu and Pb), hydrogen peroxide (30% wt.) is added during extraction. The amount of hydrogen peroxide required varies greatly between different ashes, mainly depending on the content of metallic Al. Therefore, H_2O_2 consumption is determined in advance using laboratory tests. Other factors influencing the fly ash extraction are temperature, reaction time and, related to this, the size and number of extraction vessels connected in series. The relatively high temperature results from the reaction and neutralization heat generated when ash and quench water are mixed. The residence time and the associated number of extraction vessels in existing FLUWA systems are determined by the design. Usually, three vessels connected in series with a volume adapted to the operation are used. In terms of reaction time, a total extraction time of one hour is usually implemented.

With this study the optimization of the acid fly ash leaching of a Swiss MSWI plant is analysed with the aim to determine parameters for an optimal extraction yield for zinc, lead, copper and cadmium and to compare the metal extraction yields with results from laboratory tests.

The laboratory experiments showed that above a threshold of 40 L/t FA, further hydrogen peroxide addition did not significantly improve yields of the four principal elements Cd, Cu, Pb and Zn (Fig. 8.1). It was also shown that a filtrate pH value of 4.0 and above at the end of the extraction resulted in diminished copper extraction yields through precipitation of hydroxides. The optimal extraction conditions are shown in Tab. 8.1. The transferability of the laboratory studies to the plant scale was also studied by running parallel tests on both laboratory and plant scale using the same extraction parameters.

Tab. 8.1: Optimal extraction conditions for the selected fly ash and acid scrubbing water.

Extracting agent	70% acidic scrub water 30% alkaline scrub water
L/S-ratio	3.0
Temperature (°C)	65
Extraction time (min)	60
Hydrogen peroxide 30% (L/t FA)	40
pH at the end of the extraction	3.8
Rising water (m3/h)	0.8

The yields achieved for Cd, Pb and Zn were comparable. However, the comparative study indicate large deviations in the extraction yields of copper, this can be explained by the fact that the pH value in the laboratory experiments can be controlled more easily and precisely than during continuous, large-scale operation.

In general, it can be concluded that operating parameters determined in the laboratory for optimal extraction yields are transferable to industrial operation plants.

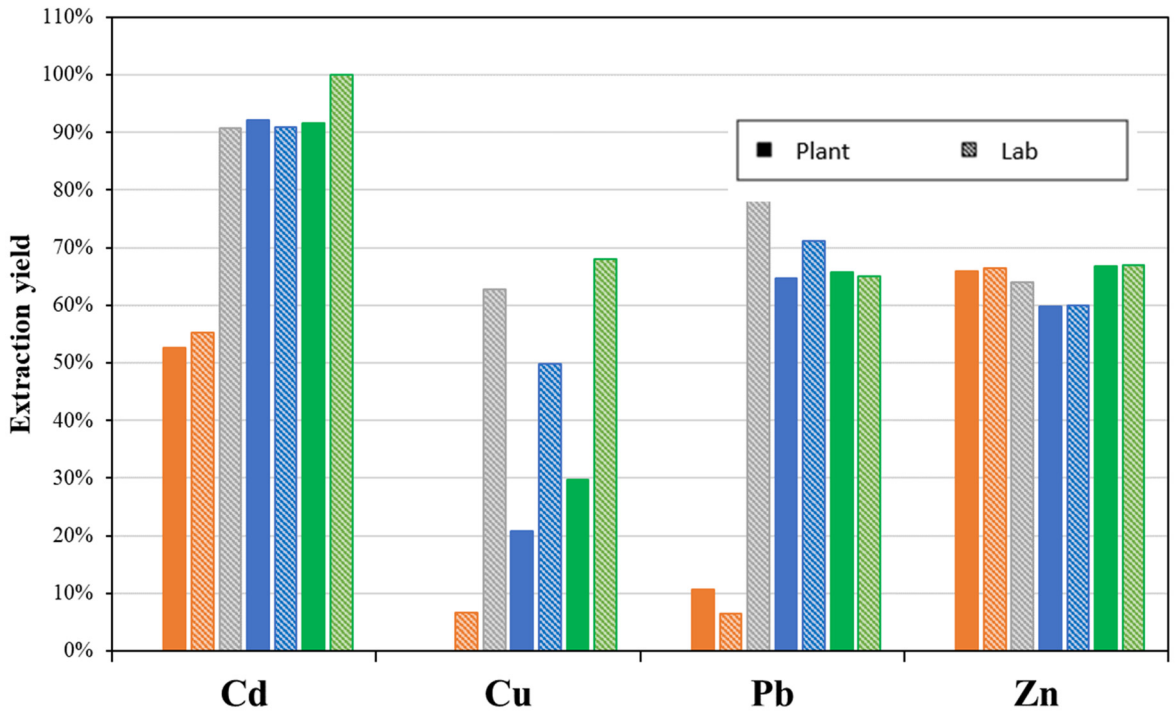

Experiment	Implementation	Date	L/S	End-pH	Oxidizers
Operating status 2017	Plant + Lab	07.12.2017	3	4.8	-
Optimum yield laboratory	Lab	15.02.2018	2	3.8	40 L H_2O_2/t FA
Optimisation experiment 1	Plant + Lab	15.02.2018	2.7	4.5	40 L H_2O_2/t FA
Optimisation experiment 1	Plant + Lab	14.06.2018	4	3.8	40 L H_2O_2/t FA

Fig. 8.1: Extraction yields of the three operating tests and the corresponding laboratory tests in comparison to the operating parameters determined in the laboratory for an optimal extraction yield.

8.3 Heavy metal recovery out of fly ash from municipal solid waste and wood incineration plants

In Switzerland, an annual load of 35'000t wood ash arises from automatic firings plants for natural forest and waste wood. One third thereof represents the fine grained wood fly ash (WA), often enriched in heavy metals (e.g. Ba, Cr, Cu, Pb, Ti, Zn) due to paintings, coatings or impregnation (Huron et al. 2017). During incineration, Cr(III) oxidizes to the very toxic and highly mobile Cr(VI) (Pohlandt-Schwandt 1999), leading to elevated Cr(VI) concentrations in wood fly ash. Thus, wood ash is considered as waste and is dumped on landfills. Due to the lack of treatment method, a temporarily regulatory permission is granted to dispose the contaminated waste wood fly ashes on landfill type D (TOC < 2 wt.%) or E (TOC < 5 wt.%), without a prior treatment up until 2023. The deposition of untreated wood fly ash may have very strong short- and long-term environmental impact due to high concentration of harmful heavy metals like Cd, Pb, Cu and Zn. Therefore, the development of a treatment technology for heavy metal depletion and a possible reduction of Cr(VI) is needed.

Acid fly ash leaching with the FLUWA process (Schlumberger et al. 2007; Bühler & Schlumberger 2010) represents a promising solution for treating wood fly ash prior to deposition, since it is performed under acid conditions. Because waste wood fly ash can yield heavy metal concentrations in the same range as the similarly generated MSWI fly ash, the co-treatment of both ashes was tested. The influence of the co-processing of wood ash in the FLUWA process was investigated in laboratory- and industrial scale experiments, the latter performed at a waste and wood power plants in Switzerland. Of a special interest was the efficiency of heavy metal recovery and the ability to outcome of Cr(VI) reduction under reducing and oxidizing processing conditions and consumption of neutralizing chemicals.

The recovery rates obtained in the laboratory experiments matched very well the corresponding recovery rates obtained in the on-site experiments. The co-treatment of wood fly ashes in the FLUWA process with 40l H_2O_2 per ton ash resulted in similar recovery rates for Zn and Cd, but in considerably lower Cu and Pb recovery rates compared to the experiments with MSWI fly ash, as seen in Fig. 8.2. A dosage of 60l H_2O_2 per ton ash resulted in similar Cu recovery rates, but still lower Pb recovery rates for the ash mix compared to the experiment with fly ash. In all the sampled filter cakes, the water-extractable Cr(VI) was below the threshold for landfill deposition.

In the laboratory-scale experiments it was observed, that wood fly ashes show a considerably lower redox potential during the FLUWA process than the MSWI fly ashes, which explains the higher oxidant dosage needed to reach a stable positive redox potential, as illustrated in Fig. 8.3. The figure shows, that the redox potential of the wood fly ashes drops shortly after the last H_2O_2 dosage during the experiment, whereas it stays constantly positive for the rest of the experiment in the MSWI fly ash. The low redox potential of the wood fly ash can be caused by the high content of organic matter (1-7 wt.%) or the presence of metals in their metallic form (mainly Al^0) – leading to rapid consumption or even catalytic destruction of the added H_2O_2. Further, the high Calcite and Ca-silicate concentration in the wood fly ash causes a high acid neutralization capacity, which led to a significantly

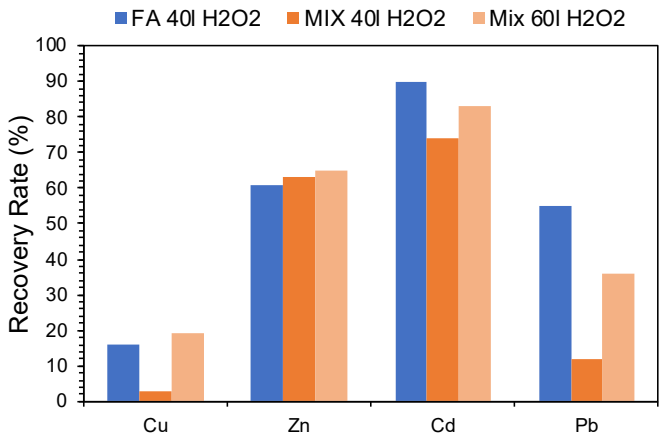

Fig. 8.2: Recovery rates achieved in on-site experiments with 40l H_2O_2 for fly ash and a mix of wood fly ash and fly ash (MIX, ratio fly ash to wood fly ash2:1). The experiment with the ash mix was repeated with 60l H_2O_2 per ton ash.

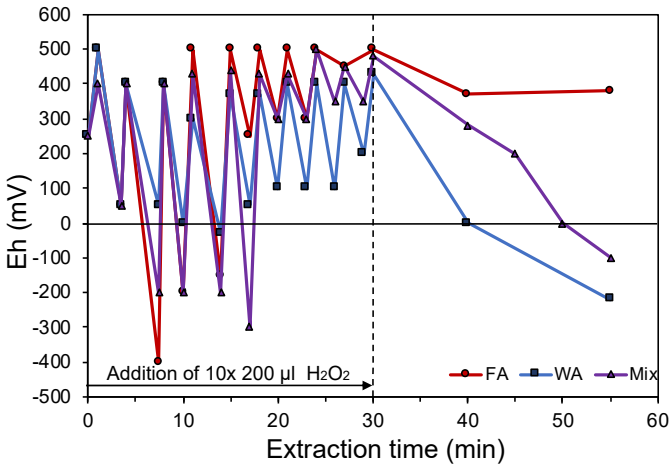

Fig. 8.3: Evolution of redox potential during H_2O_2 dosage (first 30 min of the experiment) and in the second half of the experiment, when no H_2O_2 was added.

higher acid consumption of wood ash in the FLUWA compared to MSWI fly ash (3×higher).

It can thus be concluded that the co-processing of wood ash in the FLUWA could be an efficient method for reducing the Cr(VI) concentration in the wood fly ash. However, the co-treatment of wood fly ashes results in a significantly higher acid and oxidant consumption and had a negative effect on the Pb recovery rates, probably due to the precipitation of $PbSO_4$. The high redox buffering capacity of the wood fly ashes can be of use in those incineration plants, where there is excess acidity and could be used as replacement for lime milk.

8.4 Bottom ash quality

Almost 800'000 tons of bottom ash is produced annually in Switzerland as results of the waste incineration. This solid residue may contain large quantities of heavy metals. As easily exportable natural ore resources are limited, circular economy becomes more and more important and thus waste incineration plants can contribute to sustainable use of resource serving as urban mines.

8.4.1 Influence of enhanced metal recovery on the residual bottom ash quality

MSWI bottom ash contains high amounts of ferrous (~9 wt.-%) and non-ferrous metals (~3.5 wt.-%) (Bunge 2014). The recovery of these valuable elements is regulated by the Swiss Waste Ordinance (Swiss Confederation 2016). However, there is no unified guidelines describing the metal specific technological process. Accordingly, different technics for the recovery of metals have been recently proposed and implemented in MSWI plants and on landfills. The influence of enhance recovery technics has a potential to improves the quality of the residual bottom ash sub-fractions. The process has not been studied in detail however. In general, two types of residual bottom ash fractions prevail in the enhanced metal recovery process: (1) finer fractions, which are removed at the beginning of the process by washing and/or sieving, where no metals are recovered (rBA) and (2) coarser fractions, undergoing enhanced treatment, in order to optimise the amount and quality of metals (eBA).

Two types of residual bottom ash fractions from two Swiss MSWI plants are studied in detail. A distinct fractionation has been shown for the fractions from both plants with similar enrichment and depletion tendencies for the main chemical and mineralogical composition. In order to depict these patterns all fractions of the process are normalized to the overall bottom ash composition. The resulting deviation-factor Δf is based on equation (8.1):

$$\Delta_f = \frac{c_{fraction}}{c_{overall}} \quad (8.1)$$

Δ_f : deviation-factor (-)

$c_{fraction}$: concentration of an element in a fraction out of an enhanced bottom ash treatment process (mg/kg)

$c_{overall}$: concentration of an element in the overall bottom ash of an enhanced bottom ash treatment process (mg/kg)

Thus, $\Delta_f > 1$ indicates enrichment and $\Delta_f < 1$ depletion of an element in a bottom ash fraction (Fig. 8.4a & b). By analysing the deviation factor, a strong dependency on grainsize, shaping the composition of bottom ash fractions becomes apparent:

- rBA show a strong enrichment in CaO, SO_3 and loss of ignition (LOI), which is due to the ash like mineral compounds with high content of carbonates and sulphates. In terms of trace elements, TOC, Cl and volatile heavy metals with low melting points of 300-600°C like Pb, Zn are enriched in rBA.

- eBA are dominated by SiO_2, Fe_2O_3, Al_2O_3 and Na_2O. Such coarse-grained fractions contain minerals like quartz, feldspar and pyroxene. Further, lithophilic heavy metals like Cr with melting temperatures >1400°C tend to remain in the bottom ash and are therefore enriched.

As has been revealed not only the grainsize but also the melting temperatures, especially of the heavy metals influence the observed patterns of enrichment and depletion. Additionally, process water involved in bottom ash treatment has a strong influence on release of readily soluble elements like Cl. For example, the fine fraction C-rBA2, which has been washed as part of the treatment shows 50% lower Cl-concentrations (8'000 mg/kg) than the fraction C-rBA1 (17'000 mg/kg) which has undergone dry treatment.

This study thus reveals the factors controlling the composition of residual bottom ash fractions, and highlights quality improvements made in the coarser, enhanced treated fractions. Despite these improvements, the heavy metal content in these fractions still exceeds several threshold concentration limits imposed for the secondary construction materials (Swiss Confederation 2016). Thus at present there is no alternative to status quo deposition on special landfills, and further studies and methodological developments are necessary.

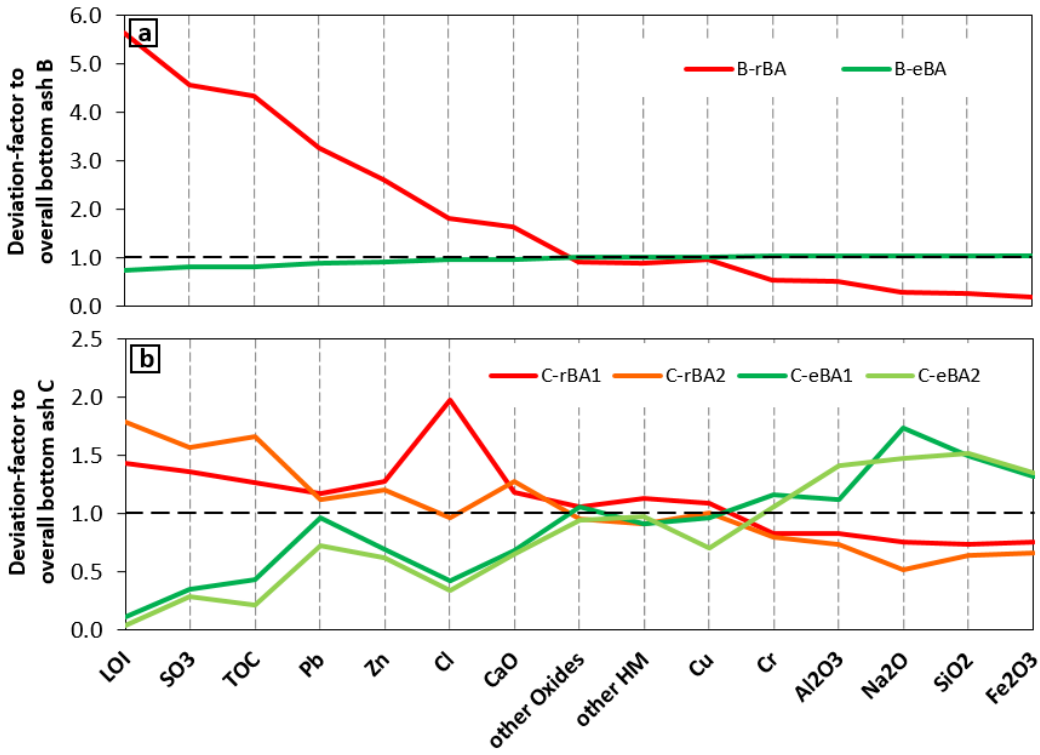

Fig. 8.4: Chemical composition of residual bottom ash fractions from enhanced metal recovery Process B and C normalized to the overall bottom ash composition of the respective process. The resulting deviation-factor (Δ_f) indicates enrichment (>1) or depletion (<1) with respect to overall bottom ash composition (--- =1). Results are in sequence of rising Δ_f for enhanced treated fractions (eBA, green lines) and declining Δ_f for removed fine fractions (rBA, red lines) respectively.

Currently analyses fractions can serve as a starting point for further treatment in order to improve their quality to suit for the utilization as secondary raw materials.

8.4.2 Dioxin destruction in residues from waste incineration plants in Switzerland

According to the Swiss Waste Ordinance the metals must be recovered from fly ash by FLUWA process from 2021 on (Swiss Confederation 2016). The washed fly ash, also called filter cake, remains and has to be deposited together with the bottom ash in landfills. After the FLUWA process, the filter cake still contains highly toxic substances, particularly dioxins and furans, which exceed in some cases the legally permitted threshold value of 1µg/kg for landfills. Within the project "ReFire" the decomposition of dioxins and furans by re-incineration of the leached filter cake was investigated on an industrial scale at two Swiss waste incineration plants. During several weeks, leached filter cake was transferred back into one of the furnace lines. ReFire bottom ash was sampled seamlessly parallel to a reference bottom ash as well as fly ashes and filter cake.

The influence of ReFire process on the chemical and mineralogical composition of the bottom ash, as well as its leaching-behaviour as the main risk assessment factor for deposition was studied in detail. Gas chromatography-mass spectrometry measurements of a reference bottom ash, ReFire bottom ash, leached filter cake and fly ashes shows that dioxins and furans were destroyed efficiently, and that they were not transferred into the ReFire bottom ash. XRF and total digestion-ICP-OES analyses reveal that the main chemical composition of the bottom ash was not changed significantly by the ReFire process. This observation is supported by PXRD determination of mineralogical composition and complementary by light microscope and scanning electron microscope analysis. It was notted however, that ReFire bottom ash show a slight increase in Pb, Sb and Sn. The increase in Pb is explained by reduction in the efficiency of the FLUWA process due to the higher sulfur input through the feedback of the filter cake as it contains high amount of sulfate phases (Fig. 8.5). This leads to precipitation of anglesite ($Pb[SO_4]$) remaining in the filter cake. Thus, it has implications on the Pb recovery from the fly ash, but determination of particulate ferrous and non-ferrous residual metal content shows that ReFire does not have negative effects on the metal recovery.

ReFire has been shown to be a an efficient practical option to reduce PCDD/F contents in landfill deposits

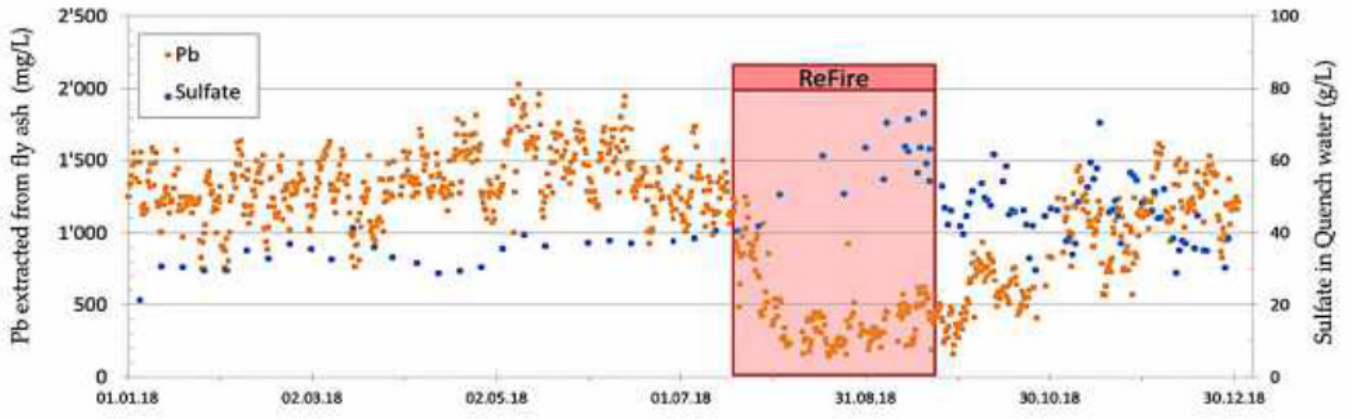

Fig. 8.5: Decrease of Pb-extraction from the fly ash in the FLUWA process, due to the increase of sulfate in the quench water. These effects are associated with the feedback of the filter cake during a ReFire test cycle (Fromm et al. 2019).

and to simplify the material flow as only bottom ash has to be deposited.

In the second step, the behaviour of the two bottom ash types under acid conditions prevailing in landfills has been investigated. Of special interest is the mobilization of heavy metals and the change of soluble phases within the bottom ash. To study this, 24h-batch-leaching tests, dynamic column tests and titration experiments to determine the acidic neutralizing capacity have been performed. The results demonstrate that the reference and ReFire bottom ashes behave very similar and that the release of heavy metals by leaching is generally limited (Fig. 8.6). This is due to the high pH-conditions, where the most relevant heavy metals like Cu, Pb, Sb show concentrations between 0.01 to 1 mg/l. The heavy metals Cr, Cd, Mn and Fe as well as Sb concentrations in the bottom ash eluates lie even <0.01 mg/l of the column eluate.

8.5 Influence of TOC concentrations in MSWI bottom ash on landfill aftercare

In Switzerland MSWI bottom ash has to comply with the legal threshold value for TOC of <2 wt.-% in order to be landfilled (Swiss Confederation 2016). However, TOC contents of this magnitude typically lead to elevated emission of dissolved organic carbon (DOC), ammonium and Cu (aq) (Chandler et al. 1997; Comans et al. 1993; Dijkstra et al. 2006; Johnson et al. 1996; van Zomeren & Comans 2004). Since 2008 the Canton of Zürich therefore pursues a strategy to lower TOC contents in bottom ash by 2020 to 0.5 wt.-%. To estimate correlations between the TOC and the other components, composition of the bottom ash has been monitored in the MSWI Plants A-F from 2008–2018. The results of the study (Fig. 8.7) indicate that TOC contents <0.5 wt.-% in bottom ash lead to DOC eluate concentrations <20 mg/l (Glauser et al. 2020).

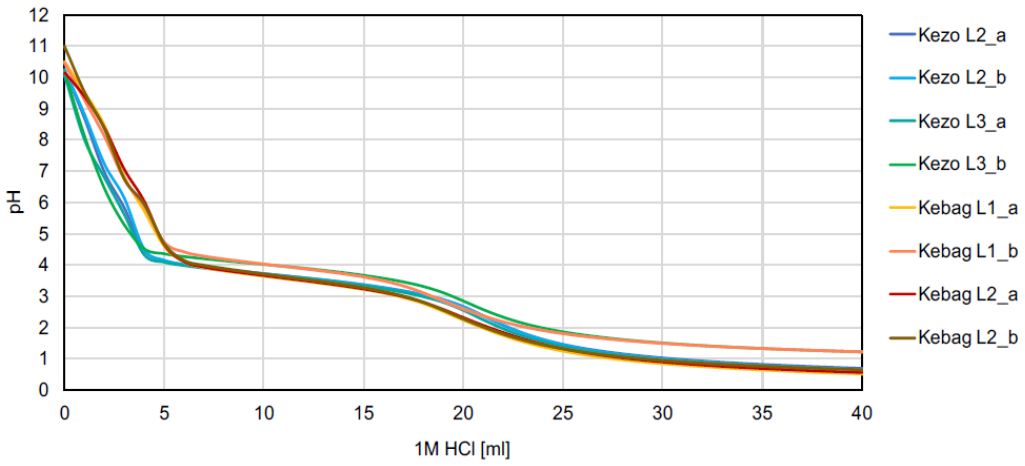

Fig. 8.6: Buffering capacity of all bottom ash samples from the studied Swiss MSWI plants KEZO and. KEBAG. The buffer capacity is independent of whether ReFire was performed or not.

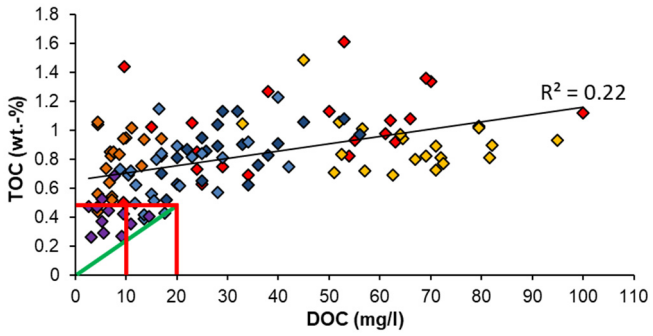

Fig. 8.7: Correlations of concentrations in bottom ash from Plant A –F between TOC and DOC. Overall no correlation exists, however TOC contents <0.5 wt.-% lead to DOC emissions <20 mg/l.

$$c_a(t) = c_0 \times e^{-\left(\frac{c_0}{m_v} \times \Delta\frac{L}{S} \times h\right) \times t} + c_{org} \times e^{-\left(\frac{c_{org}}{m_{org}} \times \Delta\frac{L}{S} \times h\right) \times t} \quad (8.2)$$

c_0 : initial concentration of readily soluble material (mg/l)
c_{org} : initial concentration of persistent organic material (mg/l)
m_v : total mobilisable fraction (mg/kg)
m_{org} : emission potential of persistent organic material (mg/kg)
$\Delta L/S$: annual change of L/S (l/kg*a)
h : heterogeneity factor of water flow in the landfill (-)
t : time after end of deposition (a)

DOC concentrations <20 µg/l are close to Swiss legal criteria for discharge of landfill leachate into surface waters (10 mg/l) according to the Swiss Water Protection Act (Swiss Confederation 1998). The emission results have been obtained by batch eluate tests according to Swiss Waste Legislation (FEON 2017). Such laboratory tests only partially simulate real conditions occurring on landfills. To approximate landfill conditions, column tests according to CEN/TS 14405 (2017) with recent bottom ashes combined with tests on simple emission forecasting complete the study (Lauer et al. 2011). The forecast is based on model calculating the concentration of a constituent at time t ($c_a(t)$; mg/l) along equation (8.2):

The comparison of results from batch and column tests shows similar cumulative concentrations, indicating that batch tests are suitable to evaluate bottom ash quality. The tested modelling approach, based on constant conditions and exponential decrease in concentration, proved adequate to simulate column progressions (Figure 8.8a). The modelled emission forecasts for DOC lie within 33% of column test results. Further, the model demonstrates the differences in flow regime between eluate tests and landfills by considering a flow factor h. Column tests are performed under homogenous flow through the material, represented by h=1 in the model. Such conditions represents a "worst case" simulation for

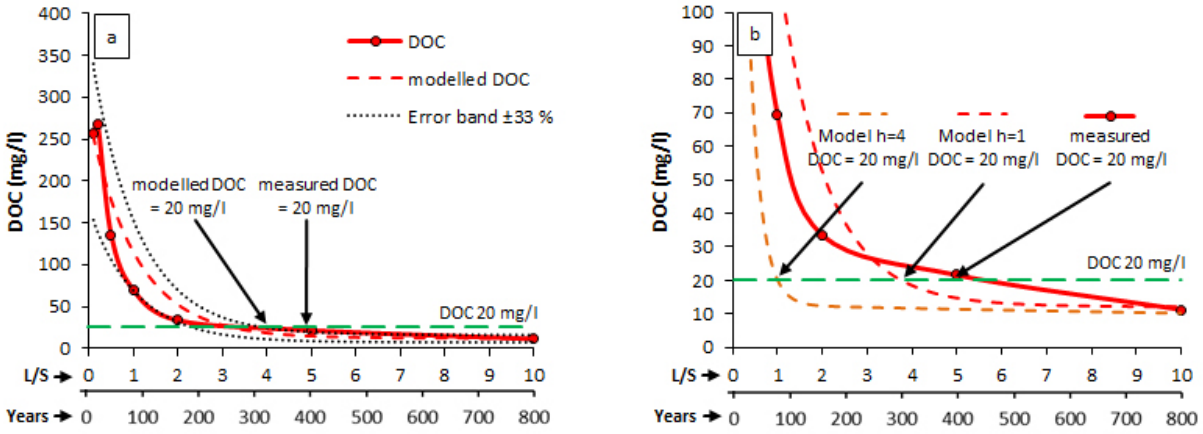

Fig. 8.8: (a) Modelled concentrations of DOC under homogenous flow in comparison with DOC measurements from column tests performed with average Swiss bottom ash. (b) Measured concentration for DOC in column tests and modelled concentrations with heterogeneity factor h=1 and h=4, respectively.

maximal leaching resulting in high DOC concentration and long aftercare phases on landfills. However, homogeneous leaching on landfills hardly ever occurs due to preferential flow paths. Changing the model parameter towards higher heterogeneity (h=4) results in only partial leaching of material. This leads to the lower mobilisation of pollutants in landfills and thus to faster decreasing DOC concentrations in the leachates (Figure 8.8b). With a scenario like this, DOC concentrations <20 mg/l on landfills are reached in approximately ¼ of the aftercare time compared to homogenous flow conditions prevailing in eluate tests. Thus, heterogeneous flow regimes contribute to a shorter landfill aftercare. However, partial leaching results in a higher remaining DOC reservoir bearing the potential of future DOC emissions due to changing preferential flow paths through new areas.

8.6 References

Bühler A., Schlumberger S. (2010)
Schwermetalle aus der Flugasche zurückgewinnen "Saure Flugaschenwäsche - FLUWA-Verfahren" ein zukunftsweisendes Verfahren in der Abfallverbrennung.

Bunge R. (2014)
Wieviel Metall steckt im Abfall. In: Thomé-Kozmiensky, K.J. (Ed.), Mineralische Nebenprodukte und Abfälle. TK Verlag Karl Thomé-Kozmiensky, Neuruppin, 91-130.

CEN/TS 14405 (2017)
Characterization of waste - Leaching behaviour tests - Up-flow percolation test (under specified conditions). European Committee for Standardization.

Chandler A.J. et al. (1997)
Municipal solid waste incinerator residues. Studies in Environmental Science, 67. Elsevier, Amsterdam.

Comans R., Van der Sloot H., Bonouvrie P. (1993)
Geochemical reactions controlling the solubility of major and trace elements during leaching of municipal solid waste incinerator residues, Proceedings of 1993 International Conference on Municipal Waste Combustion, 667-679.

Dijkstra J.J., Van Der Sloot H.A., Comans R.N. (2006)
The leaching of major and trace elements from MSWI bottom ash as a function of pH and time. Applied geochemistry, 21(2): 335-351.

FEON (2017)
Messmethoden im Abfall- und Altlastenbereich: Umwelt-Vollzug Nr. 1715. In: Federal Office for the Environment (Editor), 1-82.

Fromm S., Eggenberger U., Schlumberger S., Ulrich M. (2019)
UTF Projekt 583.12.18: 'Thermische Zerstörung von Dioxinen und Furanen in sauer gewaschenen KVA Flugaschen (ReFire)', Abschlussbericht.

Glauser A., Morf L.S., Weibel G., Eggenberger U. (2020)
Ten-years monitoring of MSWI bottom ashes with focus on TOC development and leaching behaviour. Waste Management, 117: 104-113.

Holleman A.F., E. Wiberg (2007)
Lehrbuch der Anorganischen Chemie. 102 ed.

Huron M., Oukala S., Lardière J., Giraud N., Dupont C. (2017)
An extensive characterization of various treated waste wood for assessment of suitability with combustion process. Fuel 202.

Johnson, C., Kersten, M., Ziegler, F., Moor, H. (1996)
Leaching behaviour and solubility—Controlling solid phases of heavy metals in municipal solid waste incinerator ash. Waste Management, 16(1-3): 129-134.

Lauer D., Fellner J., Brunner P.H. (2011)
Standortbezogene Kriterien zur Beurteilung der Umweltverträglichkeit von Deponieemissionen unter dem Aspekt der Nachsorgedauer (SKUDENA). Vienna University of Technology.

Pohlandt-Schwandt K. (1999)
Treatment of wood ash containing soluble chromate. Biomass and Bioenergy 16, 447–462.

Schlumberger S., Schuster M., Ringmann S., Koralewska R. (2007)
Recovery of high purity zinc from filter ash produced during the thermal treatment of waste and interting of residual materials. Waste Manag. Res. 25, 547–555.

Swiss Confederation (1998)
Waters Protection Ordinance (WPO), 1-72. Swiss Confederation, 2016. Ordinance on the Avoidance and the Disposal of Waste, 1-46.

Van Zomeren A., Comans R.N. (2004)
Contribution of natural organic matter to copper leaching from municipal solid waste incinerator bottom ash. Environmental science & technology, 38(14): 3927-3932.

Weibel G., Eggenberger U., Schlumberger S., Mäder U. (2017)
Chemical associations and mobilization of heavy metals in fly ash from mu-nicipal solid waste incineration. Waste Management 62, 147-159.

9 PUBLICATIONS

9.1 Peer reviewed research articles

Altmaier M.[1], Lothenbach B.[2], Metz V. [1], Wieland E. (2020)
Preface / Special Issue "Geochemistry research for cement-based materials in nuclear waste disposal applications". Applied Geochemistry 123, 104701.
[1]KIT/INE, Karlsruhe, Germany
[2]Empa, Dübendorf, Switzerland

Cametti G.[1], Churakov S.V. (2020)
Crystal structure of Ag-exchanged levyne intergrown with erionite: Single Crystal X-ray diffraction and Molecular Dynamics Simulations.
American Mineralogist, Special Issue on Microporous Mineral Phases, 105, 1631-1638.
[1]Institut für Geologie, Universität Bern, Switzerland

Cametti G.[1], Scheinost A.[2], Churakov S.V. (2020)
Structural Evolution of Ag-LEV Zeolite upon Heating: An In Situ Single-Crystal X-ray Diffraction (SC-XRD) and X-ray Absorption Spectroscopy (XAS) Study, ACS Omega, 5, 31774-31783.
[1]Institut für Geologie, Universität Bern, Switzerland
[2]Institute of Resource Ecology, Dresden, Germany

Churakov S.V., Hummel W., Marques Fernandes M. (2020)
Fundamental Research on Radiochemistry of Geological Nuclear Waste Disposal, Chimia 74, 1000-1009.

Curti E., Kulik D.A. (2020)
Oxygen potential calculations for conventional and Cr-doped UO_2 fuels based on solid solution thermodynamics. Journal of Nuclear Materials 534, 152140.

Di Lorenzo F.[1], Cametti G.[1], Vanhecke D.[2], Churakov S.V. (2020)
The role of interfaces in controlling Pb^{2+} removal by calcium carbonate minerals. Crystal Growth and Design, 20(9), 6157–6169.
[1]Institut für Geologie, Universität Bern, Switzerland
[2]Universität Fribourg, Switzerland

Eichinger F.[1,2], Gimmi T., Möri A.[1,3], Rüedi J.[4,5] (2020)
Profiles of chloride in matrix porewater as natural tracer for matrix diffusion in crystalline rocks. Applied Geochemistry 118 (2020) 104635.
[1]RWI, Institute of Geological Sciences, University of Bern, 3012, Bern, Switzerland
[2]Now at Hydroisotop GmbH, Schweitenkirchen, Germany
[3]Now at Federal Office of Topography Swisstopo, Wabern, Switzerland
[4]National Cooperative for the Disposal of Radioactive Waste, Wettingen, Switzerland
[5]Now at Poyry Switzerland, Zürich, Switzerland

Fazeli H.[1], Masoudi M.[1], Patel R.A., Aagaard P.[1], Hellevang H.[1] (2020)
Pore-scale modeling of nucleation and growth in porous media, ACS Earth and Space Chemistry. 2020; 4(2): 249-260.
[1]University of Oslo, Norway

Geng G., Shi Z.[1], Leemann A.[1], Borca C.[2], Huthwelker T.[2], Glazyrin K.[3], Pekov I.V.[4], Churakov S.V., Lothenbach B.[1], Dähn R., Wieland E. (2020)
Atomistic structure of alkali-silica reaction products refined from X-ray diffraction and micro X-ray absorption data. Cement and Concrete Research 129, 105958.
[1]Empa, Dübendorf, Switzerland
[2]Swiss Light Source, Villigen PSI, Switzerland
[3]DESY, Hamburg, Germany
[4]Moscow State University, Moscow, Russia

Geng G., Shi Z.[1], Leemann A.[1], Glazyrin K.[2], Kleppe A.[3], Daisenberger D.[3], Churakov S.V., Lothenbach B.[1], Wieland E., Dähn R. (2020)
Mechanical behavior and phase change of alkali-silica reaction products under hydrostatic compression. Acta Crystallographica Section B 76, 674-682.
[1]Empa, Dübendorf, Switzerland
[2]DESY, Hamburg, Germany
[3]Diamond Light Source, Didcot, United Kingdom

Glauser A.[1], Morf L.S.[2], Weibel G.[1, 3], Eggenberger U.[1] (2020)
Dataset on ten-years monitoring of MSWI bottom ashes in six MSWI plants in the Canton of Zürich, Switzerland. Data in Brief: 106261.
[1]Institut für Geologie, Universität Bern, Switzerland
[2]Baudirektion Kanton Zürich, Amt für Abfall, Wasser, Energie und Luft, Zürich, Switzerland
[3]Zentrum für nachhaltige Abfall- und Ressourcennutzung ZAR, Hinwil, Switzerland

Glauser A.[1], Morf L.S.[2], Weibel G.[1, 3], Eggenberger U.[1] (2020)
Ten-years monitoring of MSWI bottom ashes with focus on TOC development and leaching behaviour. Waste Management, 117: 104-113.
[1]Institut für Geologie, Universität Bern, Switzerland
[2]Baudirektion Kanton Zürich, Amt für Abfall, Wasser, Energie und Luft, Zürich, Switzerland
[3]Zentrum für nachhaltige Abfall- und Ressourcennutzung ZAR, Hinwil, Switzerland

Glaus M.A., Frick S., Van Loon L.R. (2020)
A coherent approach for cation surface diffusion in clay minerals and cation sorption models: Diffusion of Cs^+ and Eu^{3+} in compacted illite as case examples. Geochimica et Cosmochimica Acta 274, 79–96.

Guillemot T., Cvetković B.Z., Kunz D., Wieland E. (2020)
Processes leading to reduced and oxidised carbon compounds during corrosion of zero-valent iron in alkaline anoxic conditions. Chemosphere 250, 126230.

Guillemot T., Salazar G.[1], Cvetković B.Z., Kunz D., Szidat S.[1], Wieland E. (2020)
Determination of ultra-low concentrations of gaseous ^{14}C-bearing hydrocarbons produced during corrosion of irradiated steel using accelerator mass spectrometry. Analyst 145, 7870-7883.
[1]University of Bern, Bern, Switzerland

Hax Damiani L., Kosakowski G., Glaus M.A., Churakov S.V. (2020)
A framework for reactive transport modeling using FEniCS–Reaktoro: governing equations and benchmarking results. Computational Geosciences 24, 1071–1085.

Idiart A.[1], Laviña M.[1], Kosakowski G., Cochepin B.[2], Meeussen J.C.L.[3], Samper J.[4], Mon A.[4], Montoya V.[5,6], Munier I.[2], Poonoosamy J.[7], Montenegro L.[4], Deissmann G.[7], Rohmen S.[7], Damiani L.H., Coene E.[1], Naves A.[4] (2020)
Reactive transport modelling of a low-pH concrete / clay interface. Applied Geochemistry, 115, 104562.
[1]Amphos 21 Consulting, Barcelona, Spain
[2]Andra, Châtenay-Malabry, France
[3]Nuclear Research and Consultancy Group, Petten, the Netherlands
[4]Universidade de A Coruña, A Coruña, Spain
[5]Helmholtz-Centre for Environmental Research, (UFZ), Leipzig, Germany
[6]Institute for Nuclear Waste Disposal, (INE), Karlsruhe Institute of Technology, (KIT), Karlsruhe, Germany
[7]Forschungszentrum Jülich, Jülich, Germany

Jaquenoud M.[1], Elam W.T.[2], Grundl T.[3], Gimmi T., Jakob A., Schefer S.[4], Cloet V.[5], de Cannière P.[6], Van Loon L.R., Leupin O.X.[1] (2020)
X-ray fluorescence monitoring of iodide diffusion through Opalinus Clay: Demonstration of a novel experimental approach, Chemosphere (in press 2020), 128674.
[1]National Cooperative for the Disposal of Radioactive Waste, Wettingen, Switzerland
[2]Applied Physics Lab, University of Washington, Seattle, WA, 98105, USA
[3]ASchool of Freshwater Sciences, University of Wisconsin-Milwaukee, WI, 53201, USA
[4]Swisstopo, Route de la Gare 63, 2882, St-Ursanne, Switzerland
[5]Arcadis, Ifangstrasse 11, 8952, Schlieren, Switzerland
[6]FANC-AFCN, 1000, Brussels, Belgium

Keri A., Dähn R., Marques Fernandes M., Scheinost A., Krack M., Churakov S.V. (2020)
Iron Adsorption on Clays Inferred from Atomistic Simulations and X-ray Absorption Spectroscopy Environmental Science and Technology 54(9), 11886-11893.

Leal A.M.M.[1], Kyas S.[1], Kulik D.A., Saar M.O.[1] (2020)
Accelerating reactive transport modeling: On-Demand Machine Learning algorithm for chemical equilibrium calculations. Transport in Porous Media, 133, 161-204.
[1]Department of Earth Sciences, Geothermal Energy and Geofluids Group, Institute of Geophysics, ETH Zürich, Zurich, Switzerland

Luraschi P., Gimmi T., Van Loon L.R., Shafizadeh A. Churakov S.V. (2020)
Evolution of HTO and $^{36}Cl^-$ diffusion through a reacting cement-clay interface (OPC paste-Na montmorillonite) over a time of six years. Applied Geochemistry 119, 104581.

Ma B.[1], Fernandez-Martinez A.[2], Mancini A., Lothenbach B.[1] (2020)
Spectroscopic investigations on structural incorporation pathways of FeIII into zeolite frameworks in cement-relevant environments. Cement and Concrete Research 140, 106304.
[1]Empa, Dübendorf, Switzerland
[2]Université Grenoble Alpes, Grenoble, France

Mancini A., Lothenbach B.[1], Geng G., Grolimund D.[2], Sanchez D.F.[2], Fakra S.C.[3], Dähn R., Wehrli B.[4], Wieland E. (2020)
Iron speciation in blast furnace slag cements. Cement and Concrete Research 140, 106287.
[1]Empa, Dübendorf, Switzerland
[2]Swiss Light Source, Villigen PSI, Switzerland
[3]Advanced Light Source, Berkeley, United States
[4]ETH Zürich, Zürich, Switzerland

Mancini A., Wieland E., Geng G., Dähn R., Skibstedt J.[1], Wehrli B.[2], Lothenbach B.[3] (2020)
Fe(III) uptake by calcium silicate hydrates. Applied Geochemistry 113, 104460.
[1]Aarhus University, Aarhus, Denmark
[2]ETH Zürich, Zürich, Switzerland
[3]Empa, Dübendorf, Switzerland

Miron G.D.[1], Kulik D.A.[1], Thoenen T.[1] (2020)
Generating isocoulombic reactions as a tool for systematic evaluation of temperature trends of thermodynamic properties: Application to aquocomplexes of lanthanides and actinides. Geochim. Cosmochim. Acta 286, 119–142.

Molins S.[1], Soulaine C.[2,3,4], Prasianakis N.I., Abbasi A., Poncet P.[5], Ladd A.J.[6], Starchenko V.[7], Roman S.[2,4], Trebotich D.[1], Tchelepi H.A[2]., Steefel C.I.[1] (2020)
Simulation of mineral dissolution at the pore scale with evolving fluid-solid interfaces: review of approaches and benchmark problem set. Computational Geosciences, 1-34.
[1]Lawrence Berkeley National Laboratory, Berkeley, CA, USA
[2]Stanford University, Stanford, CA, USA
[3]French Geological Survey (BRGM), Orleans, France
[4]Universite Orleans-CNRS-BRGM, - Institut des Sciences de la Terre d'Orleans, Orleans, France
[5]E2S UPPA, CNRS, LMAP UMR 5142, Universite de Pau, Pays Adour, Pau, France
[6]University of Florida, Gainesville, FL, USA
[7]Oak Ridge National Laboratory, Oak Ridge, TN, USA

Nedyalkova L., Lothenbach B.[1], Geng G., Mäder U.[2], Tits J. (2020)
Uptake of iodide by calcium aluminate phases (AFm phases). Applied Geochemistry 116, 104559.
[1]Empa, Dübendorf, Switzerland
[2]University of Bern, Bern, Switzerland

Poonoosamy J.[1], Klinkenberg M.[1], Deissmann G.[1], Brandt F.[1], Bosbach D.[1], Mäder U.[2], Kosakowski G. (2020)
Effects of solution supersaturation on barite precipitation in porous media and consequences on permeability: Experiments and modelling. Geochimica et Cosmochimica Acta, 270, 4360.
[1]Forschungszentrum Jülich, Jülich, Germany
[2]Institute of Geological Sciences, University of Bern, Bern, Switzerland

Prasianakis N.I., Haller R., Mahrous M., Poonoosamy J.[1], Pfingsten W., Churakov S.V. (2020)
Neural network based process coupling and parameter upscaling in reactive transport simulations. Geochimica et Cosmochimica Acta, 291, 126-143.
[1]Forschungszentrum Julich, 52425 Julich, Germany

Rodriguez-Navarro C.[1], Burgos-Cara A.[1], Di Lorenzo F.[2], Ruiz-Agudo E. [1], Elert K.[1] (2020)
Nonclassical Crystallization of Calcium Hydroxide via Amorphous Precursors and the Role of Additives. Crystal Growth and Design, 20(7), 4418–4432.
[1]University of Granada, Granada, Spain
[2]University of Bern, Bern, Switzerland

Shafizadeh A., Gimmi T., Van Loon L.R., Kaestner A.P., Mäder U.K.[1], Churakov S.V. (2020)
Time-resolved porosity changes at cement-clay interfaces derived from neutron imaging
Cement Concrete Research 127 , 105924.
[1]University of Bern, Bern, Switzerland

Tournassat C.[1,2,3], Steefel C.I[1], Gimmi T. (2020)
Solving the Nernst-Planck equation in heterogeneous porous media with finite volume methods: Averaging approaches at interfaces. Water Resources Research, 56, e2019WR026832.
[1]Lawrence Berkeley National Laboratory, Berkeley, CA, USA
[2]BRGM, Orléans, France
[3]Université d'Orléans-CNRS/INSU-BRGM, Institut des Sciences de la Terre d'Orléans, Orléans, France

Vespa M.[1], Borca C.[2], Huthwelker T.[2], Lothenbach B.[3], Dähn R., Wieland E. (2020)
Structural characterisation of magnesium (sodium) aluminium silicate hydrate (M-(N)-A-S-H) phases by X-ray absorption near-edge spectroscopy. Applied Geochemistry 123, 104750.
[1]GeochEnv Consulting, Herrischried, Germany
[2]Swiss Light Source, Villigen PSI, Switzerland
[3]Empa, Dübendorf, Switzerland

Wick S.[1,2], Baeyens B.[3], Marques Fernandes M.[3], Göttlicher J.[4], Fischer M.[2], Pfenninger N.[1], Plötze M.[5], Voegelin A.[1] (2020)
Thallium sorption and speciation in soils: Role of micaceous clay minerals and manganese oxides. Geochimica et Cosmochimica Acta 288, 83-100.
[1]Eawag, Swiss Federal Institute of Aquatic Science and Technology, Dübendorf, Switzerland
[2]ETH Zürich, Zürich, Switzerland
[3]Paul Scherrer Institute, Villigen PSI, Switzerland
[4]Karlsruhe Institute of Technology, Eggenstein-Leopoldshafen, Germany
[5]ETH Zürich, Zürich, Switzerland

Wieland E., Kosakowski G., Lothenbach B.[1], Kulik D.A. (2020)
Geochemical modelling of the effect of waste degradation processes on the long-term performance of waste forms. Applied Geochemistry 115, 104539.
[1]Empa, Dübendorf, Switzerland

Yang G., Prasianakis N.I., Churakov S.V. (2020)
Comparative Modeling of Ions and Solvent Properties in Ca-Na Montmorillonite by Atomistic Simulations and Fluid Density Functional Theory Clays and clay minerals 68(2), 100-11 .

9.2 Technical reports

Glauser A., Weibel G., Eggenberger U. (2020)
Untersuchung der Schlackenqualität in der Schweiz: Charakterisierung – Ablagerung – Verwertung.

Kosakowski G., Huang Y., Wieland E. (2020)
Influence of material heterogeneities, process couplings and aggregate reactivity on the geochemical evolution of the L/ILW repository. Nagra Work Report NAB 20-11.

Weibel G. (2020)
Deponie Chrüzlen - Monitoring und Emissions-prognose des Trockenschlackenkompartiments.

Wieland E., Kosakowski G. (2020)
Review of the compositions of hydrated cements and cement-type pore water at different stages of the cement degradation. Nagra Work Report NAB 20-12.

Zappatini A., Eggenberger U. (2020)
Testverfahren von verfestigten problematischen Abfällen. On behalf of the Federal Office for the Environment.

9.3 Conferences/workshops/presentations

Gimmi T., Mazurek M. (2020)
CLAYWAT: Binding state and mobility of water in clay-rich media.
30th NEA/Clay Club meeting, 23.9.2020.

Gysi A., Hurtig N., Miron G.D. (2020)
An introduction to thermodynamic modeling of fluid-rock interaction and ore-forming processes using the GEMS code package, Geochemical Society online workshop, 8-9 December 2020.

Hummel W. (2020)
Solubility and speciation of mercury under anoxic conditions. 18th Swiss Geoscience Meeting, Symposium Nr. 4 Environmental Biogeochemistry of Trace Elements, Zürich, Switzerland, 7 November 2020.

Marques Fernandes M., Baeyens B., Daehn R., Scheinost A., Churakov S.V. (2020)
Fate of contaminants from repositories for radioactive waste based in clay-rock? 18th Swiss Geoscience Meeting, Symposium Nr. 4 Environmental Biogeochemistry of Trace Elements, Zürich, Switzerland, 7 November 2020.

Montoya V., Águila J.F., Samper J., Montenegro L., Kosakowski G., Krejci P., Pfingsten W. (2020)
Modelling Cs migration through Opalinus clay: A benchmark for single- and multi-species sorption-diffusion models. The international workshop on "How to integrate geochemistry at affordable costs into reactive transport for large-scale systems?", 5-7 February 2020, Dresden, Germany.

Patel R.A., Prasianakis N.I. (2020)
Pore-scale numerical modelling tools for improving efficiency of direct carbon capture in compacts
3rd RILEM Spring Convention 2020, March 10-14, 2020, Guimarães, Portugal.

Pfingsten W., Ayoub A., Podofillini L., Sansavini G. (2020)
Multiple complex reactive transport calculations to estimate the influence of uncertain Cs sorption parameters on Cs diffusion in clay and to construct a "new Cs Kd band". The international workshop on "How to integrate geochemistry at affordable costs into reactive transport for large-scale systems?", 5-7 February 2020, Dresden, Germany.

Poonoosamy J., Curti E. , Bosbach D., Churakov S.V., Wierwiller G.T., Deismann G., Prasianakis N.I. (2020)
(Ba,Sr)SO4 oscillatory zoning: a microfluidic experiment and advance pore scale modelling to unravel the process, American Geophysical Union Fall Meeting, AGU 2020. H094: Pore-scale physics: recent advances in experimental and computational methods (1-17 December 2020).

Prasianakis N.I., Haller R., Mahrous M., Poonoosamy J., Pfingsten W., Churakov S.V. (2020)
Machine Learning Enhanced Process Coupling and Parameter Upscaling in Reactive Transport Simulations. The international workshop on "How to integrate geochemistry at affordable costs into reactive transport for large-scale systems?", 5-7 February 2020, Dresden, Germany.

Wieland E. (2020)
Carbon-14 bearing compounds formed during corrosion of irradiated steel in cementitious environment, TRU-Waste 8 Workshop, Paris, France, 3-5 February 2020.

Yang Y., Prasianakis N.I., Churakov S.V., Patel R.A., Deissmann G. (2020)
Pore-scale numerical modePore scale modeling of ion diffusion in variably saturated clays. AGU Fall Meeting, Virtual, USA, 1 Dec 2020 - 17 Dec 2020.

9.4 Invited Talks

Prasianakis N.I. (2020)
Keynote talk: Towards Digital Twins: Machine Learning Based Process Coupling and Multiscale Modelling of Reactive Transport Phenomena, Goldschmidt Conference, Hawaii, USA, (June 2020, in virtual format).

9.5 Teaching

Churakov S.V.
Bachelor course: Kristallographie I+II, Institut für Geologie, Universität Bern, Spring and Fall Semester.

Churakov S.V.
Bachelor course: Kristalloptik. Institut für Geologie, Universität Bern, Fall Semester.

Eggenberger U., Zucha W., Wolffers M., Glauser A.
Master Course: Geochemical Analysis of Rocks, Institut für Geologie, Universität Bern, Fall semester 2020.
Master Course: X-Ray Powder Diffraction, Institut für Geologie, Universität Bern, Fall semester 2020.
CAS Course: Contaminated Sites, Institut für Geologie, Universität Bern, June 2020.

Gimmi T. (with Diamond L., van den Heuvel D., Mazurek M., Pettke T.)
Master course: Fluids in the crust. Institut für Geologie, Universität Bern, Fall Semester.

Plötze L.M., Hummel W.
Master Course: Landfilling, Contaminated Sites and Radioactive Waste Repositories, ETH Zurich, Fall semester.

Prasser H.-M., Günther-Leopold I., Hummel W.
Master Course: Nuclear Energy Systems, ETH Zurich, Spring semester.

9.6 PhD thesis defences

Mancini A. (2020)
Thermodynamic and spectroscopic investigations of ferric and ferrous iron in cementitious systems. ETH Zürich, Zürich, Switzerland, 18 March 2020.

Wick S. (2020)
Sorption of thallium to illite and birnessite and its impact on the solubility of thallium in soil. ETH Zürich, Zürich, Switzerland, 28 January 2020.

9.7 Other

Churakov S.V., Di Lorenzo F.
Guest Editor Minerals MDPI Special Issue "Mineral Surface Reactivity with Application to Contaminant Retention and Element Partitioning".

Gimmi T.
Associate Editor of Applied Geochemistry

Pfingsten W.
Secretary General of SITEX. Network Association.

Pfingsten W.
Examination of PhD thesis of Shuo Meng "Solute transport in fractured rocks: Analysis of analytical solutions and determinations of transport parameters", KTH Stockholm, Sweden, 28 February 2020.

Paul Scherrer Institut :: Forschungsstrasse 111 :: 5232 Villigen PSI :: Switzerland :: Tel. +41 56 310 21 11 :: www.psi.ch